



The University of  
**Nottingham**

UNITED KINGDOM · CHINA · MALAYSIA

# Modelling The Effects of Rotation and Tides on Dense Ocean Currents

Elmaghrbi M.S.

Thesis submitted to the University of Nottingham  
for the degree of Doctor of Philosophy (PhD)

2018

# Abstract

Dense ocean currents play a role in controlling the global climate through the ocean conveyor belt. These currents are found to be heavily impacted by the tidal motion, as the sources of these currents are often located at geographical areas of high tidal activities around the Earth. A streamtube model is used to describe these currents by studying the properties of these flows in both space and time domains, as the currents propagate downstream. The study found that in the presence of a background stratification the steady state streamtube experiences oscillatory behaviour which is modulated by the Coriolis parameter, the buoyancy frequency of the ambient, as well as the drag and entrainment coefficients of the current.

The results also show that the behaviour of unsteady dense currents can not be predicted using the same approaches used to model steady state dense currents and that a new unsteady system is required. The new model shows the presence of unsteady waves in time dependent dense currents. The unsteady waves are found to depend on the frequency and the amplitude of the temporal changes at the source of the current, with higher frequencies and amplitudes giving stronger waves. The waves are found to be modulated by the state variables and parameters, as well as the strength of the background ambient stratification.

*“All praises are to Him”*

# Acknowledgements

I would like to thank the University of Nottingham as a whole for the continuous support, both in my academic and personal life, especially the Faculty of Engineering and the Dean of Engineering Scholarship Scheme.

To the lights that showed me the way when it was darkest, my mum and dad, I could not have got here without your unbounded support. And to the joys of my life, my brothers and sisters, you are my world.

Last but not least, I would like to thank my friends in Nottingham and beyond, who supported me throughout the Ph.D, the thesis and my life in general.

# Contents

<b>1</b>	<b>Introduction</b>	<b>1</b>
1.1	Overview . . . . .	1
1.2	The formation of dense currents . . . . .	7
1.3	Using a top-hat streamtube model as a coherent structure to describe dense currents . . . . .	11
1.4	Gravity and inertial waves . . . . .	12
1.5	Laboratory experiments for rotating gravity currents . . . . .	15
1.6	Aims and objectives . . . . .	17
1.7	Outline of thesis . . . . .	18
<b>2</b>	<b>Theory</b>	<b>20</b>
2.1	Derivation outline . . . . .	20
2.2	Introduction . . . . .	20
2.3	Background studies . . . . .	21
2.4	The unsteady model . . . . .	26
2.4.1	Formulation . . . . .	26
2.4.2	Rotating into the continental slope coordinate system . . . . .	28
2.4.3	Reynolds averaging . . . . .	32
2.4.4	Transformation into path-relative coordinates . . . . .	36

2.4.5	Non-dimensionalisation of the equations . . . . .	49
2.4.6	Cross-sectional averaging to find bulk quantity equations . . . . .	57
<b>3</b>	<b>Methodology, and steady state current's flow in a homogeneous ambient</b>	<b>62</b>
3.1	Methodology . . . . .	63
3.2	Comparison with Smith (1975) . . . . .	68
3.3	The effects of different initial state variables . . . . .	70
3.4	The effects of different state parameters . . . . .	78
<b>4</b>	<b>Steady state currents and their oscillatory behaviour</b>	<b>84</b>
4.1	The effect of the background ambient stratification . . . . .	84
4.2	The effects of changing the state parameters . . . . .	94
4.2.1	Coriolis . . . . .	94
4.2.2	Drag coefficient . . . . .	99
4.2.3	Entrainment coefficient . . . . .	101
4.3	The limiting cases of the oscillations in the steady state currents . . . . .	104
<b>5</b>	<b>The unsteady model</b>	<b>109</b>
5.1	Stability of the unsteady model . . . . .	110
5.1.1	Velocity . . . . .	110
5.1.2	Cross sectional area . . . . .	113
5.1.3	Density . . . . .	115
5.2	The effect of a pulsing source . . . . .	116
5.2.1	Varying the initial velocity . . . . .	118
5.2.2	Varying initial cross-sectional area . . . . .	119
5.2.3	Varying the initial density . . . . .	120
5.3	The effect of changing the initial current path . . . . .	122

5.4	The effects of the amplitude and frequency of the oscillations . . . . .	123
5.4.1	Change of the oscillation amplitude . . . . .	123
5.4.2	Change of the oscillation frequency . . . . .	124
5.5	The effect of changing the stratification . . . . .	126
5.6	The effect of changing the state parameters . . . . .	129
5.6.1	Coriolis . . . . .	131
5.6.2	Drag coefficient . . . . .	133
5.6.3	Entrainment coefficient . . . . .	135
5.7	Analysis of the overshooting . . . . .	137
<b>6</b>	<b>Conclusion</b>	<b>144</b>
6.1	Summary of thesis . . . . .	144
6.2	General conclusions . . . . .	144
6.3	Future work . . . . .	147

# Chapter 1

## Introduction

### 1.1 Overview

The global ocean waters are in continuous circulation around the Earth in a combination of individual currents, operating in a similar fashion to a conveyor belt. These currents have a direct effect on the Earth's climate, making them an important factor to consider when analysing climate change [Broecker et al., 1991]. At high latitudes, waters are cooled down due to the low atmospheric temperatures and/or sea ice formation. This process increases the waters' density. Furthermore, in the case of ice formation, the rejection of brine from the ice adds to the increase of the cold water density, as salinity is the dominant driver of the density increase (Cenedese and Adduce [2008]; Holland [2011]). This density increase causes the newly formed cold waters to travel in currents sinking down due to gravity; these currents are called dense currents. The cold water is replaced with less dense warmer waters arriving from warmer climates in the form of shallower currents [Foster and Carmack, 1976].

Figure 1.1 shows a schematic of the ocean conveyor belt. This was first introduced by

Broecker et al. [1991], whose work essentially cemented the role of the conveyor belt as an agent of climate change. This circulation is also known as the ocean’s Thermohaline circulation, due to the fact that it is driven primarily by density differences arising from different salt and heat content of the currents in comparison to the ambient surroundings that these currents travel through [Lozier, 2010]. The four yellow circles shown in Figure 1.1, in the North Atlantic, the Ross Sea and the Weddell Sea off Antarctica, are examples of areas in the ocean that act as cooling regions for the conveyor belt. The warm surface currents, shown in red, transport waters poleward towards these regions, before the waters recirculate at depth and head back equatorward [Shepard et al., 1939]. The purple currents represent waters that travel across an ocean/sea bottom and are known as “bottom currents”, whereas blue currents represent waters that do not descend to the ocean bottom, but interleave at their level of neutral buoyancy and are known as “intermediate currents” [Ollitrault et al., 2006].

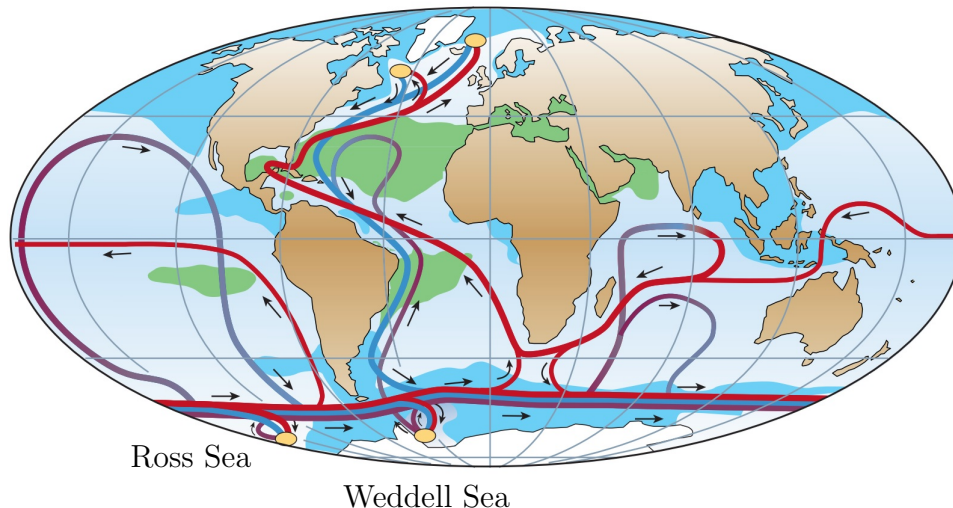


Figure 1.1: Schematic of the ocean conveyor belt as shown in Rahmstorf [2002]. The orange represents warm shallow currents, whereas the the cold, deep currents are represented in blue, with the arrows indicating the direction of flow.

Focusing on the Southern Hemisphere, Figure 1.2 shows a three-dimensional inter-basin flow schematic for the ocean water circulation, displaying the main active currents in the

three oceans in the Southern Hemisphere.

The figure contains a qualitative summary of the currents present in the indicated oceans and the key horizontal connections between these oceans, while illustrating the driving force behind these currents being the presence of the cold dense currents off Antarctica [Schmitz, 1996]. It can be seen that the currents descending down the oceans are concentrated at two main points, the first of which is off Antarctica, where we find the Circumpolar Deep Water current (CDW), which feeds into the Antarctic Intermediate Water (AAIW) and the Antarctic Bottom Water (AABW). The second region is found north of the equator, indicated here with the North Atlantic Deep Water (NADW) in green, and the Labrador Sea Water (LSW) in red.

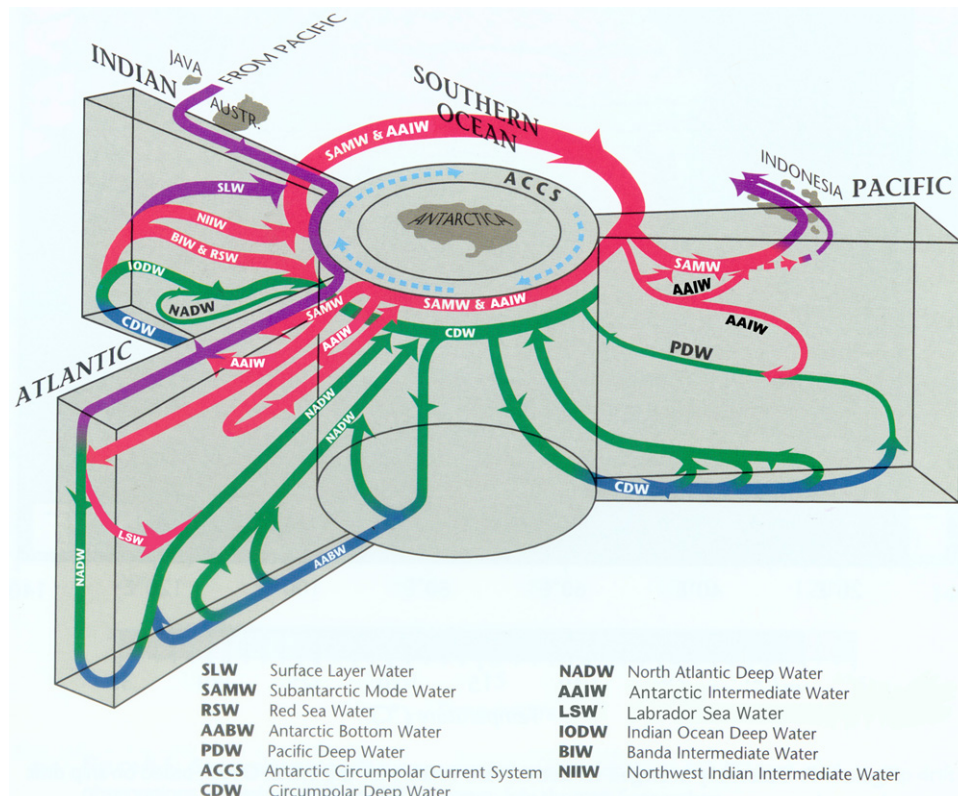


Figure 1.2: A three-dimensional schematic showing the major currents present in the southern hemisphere ocean circulations [Schmitz, 1996].

The fundamental dynamics of dense gravity currents have been studied for decades, with

researchers providing both experimental and mathematical models in order to help understand the complexity of such systems [Holland, 2011]. Recent observations have shown that tides play an important role in the behaviour and physics of these ocean currents (Whitworth and Orsi [2006]; Muench et al. [2009]; Padman et al. [2009]; Wang et al. [2010]).

Holland [2011] showed that the tidal impact on these currents that drive the polar water flows can be divided into three categories:

1. Redirecting the flow of the dense water as the tide affects the current's path;
2. Affecting the dynamics of the flow as the tidal excursion produces a 'pulsed source' of dense water;
3. Adding variable mixing to the plume, due to the oscillating tidal shear at the interface between the dense plume water and the ambient water surrounding it and/or at the seabed.

Holland [2011] investigated a current with a fixed path, and studied the other two categories. He concluded that the pulsed source case which affects the supply of dense water to the current is responsible for the hydrographic variability of the downstream behaviour, rather than variation in the current mixing. This study will look into currents that experience path oscillations as well as pulsed sources.

All four yellow circles in Figure 1.1, which represent the main sources of the dense currents in the ocean conveyor belt, are located in very active tidal regions, as can be seen in Figure 1.3. Looking at the two regions in the Southern Hemisphere in Figure 1.1, which are the Ross Sea and the Weddell Sea off the coast of Antarctica, we find out that the dense currents there are created due to ice formation. The tides affect the currents' sources and make them act in a pulsing manner [Holland, 2011].

As the positioning of the Moon and Sun changes with respect to the Earth, the gravitational attraction on the sea water of the rotating Earth changes. Hence, the tidal behaviour of the sea differs at different phases of the Moon. During the full and new Moons, where the Sun acts in conjunction with the Moon, the tides are at their maximum oscillation amplitude and are known as ‘spring’ tides. On the other hand, when the Moon goes through the first and third quarters, acting in opposition to the Sun, the tides in action are known as ‘neap’ tides [Visser, 1980].

In the neap tides phases, the dense currents behave in a relatively steady manner, as the tidal velocity is very small in comparison with the dense current velocity (Gordon et al. [2004]; Whitworth and Orsi [2006]; Gordon et al. [2009]; Muench et al. [2009]; Padman et al. [2009]; Wang et al. [2010]). They can be modelled mathematically using models such as that of Smith [1975], which the unsteady system in this study will be based on and will be explained in detail in section 2.3. More importantly, during the spring tides, the tides cause the currents’ paths to be considerably changed, making the steady-state models insufficient in predicting the behaviour of the downstream path (Smith [1975], Erofeeva et al. [2005]; Padman et al. [2009]; Holland [2011]). Taking the Ross Sea as an example, spring tides can reach velocities of up to  $1 \text{ m s}^{-1}$ , displacing the current source back and forth by about 20 km (Whitworth and Orsi [2006]; Padman et al. [2009]; Wang et al. [2010]). This process causes the the source of the current to behave in a pulsing manner, making the downstream current behaviour both time- and space-dependent [Holland, 2011].

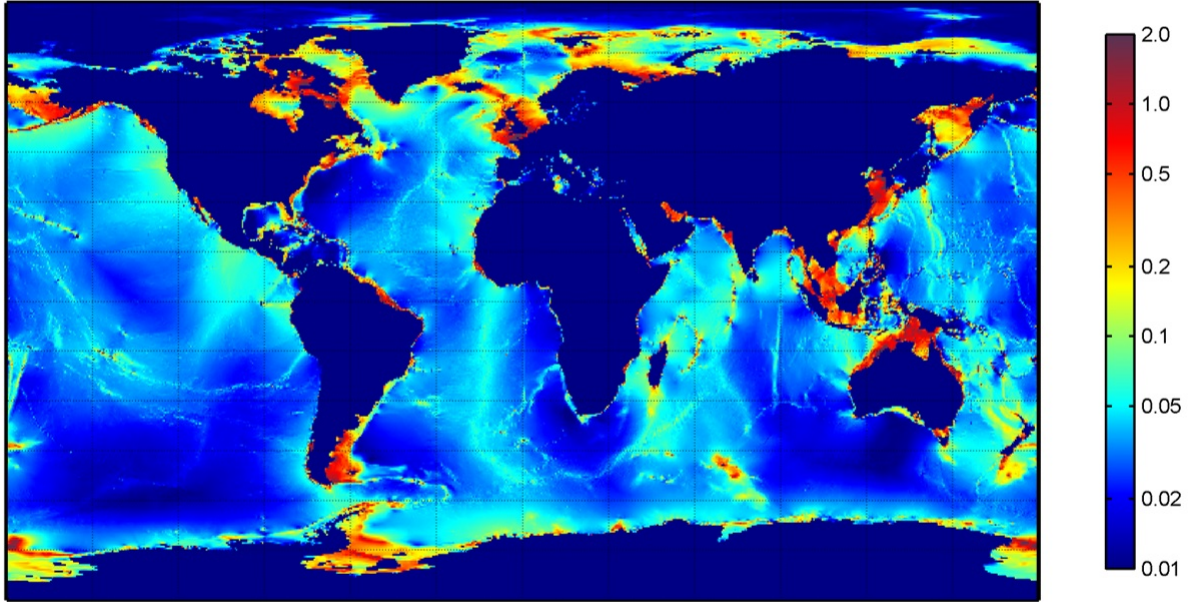


Figure 1.3: Schematic of global maximum tidal speed. The units on the right are in  $\text{m s}^{-1}$ , (Holland [2010]; COAS)

Figure 1.3 shows a large distribution in tidal activity across the global ocean water bodies. In regions of high tidal activities, tide speeds can reach up to  $2 \text{ m s}^{-1}$ , whereas in other regions, tides can be nearly non-existent, with tide speeds of  $0.01 \text{ m s}^{-1}$ . This further illustrates the importance of including the effects of these tidal activities on the dense ocean currents under investigation. As new discoveries are made regarding the dynamics of these currents, such as the effects of tidal motion on them, existing models are adapted accordingly. However, a full model for all global ocean currents is yet to be established.

Figure 1.4 gives a more detailed account of the maximum tidal current speed at the Ross Sea outflow off Antarctica, focusing on the area where the bottom left yellow circle is in Figure 1.1. Here the tide speeds can be as high as  $1 \text{ m s}^{-1}$ . With such complexity present, this study will focus on the dense currents driving these ocean currents, hence, the ocean conveyor belt, and what effects source time-dependency have on them. It is important to examine what generates these dense currents, and how they initially interact with the

ambient fluids in the oceans surrounding them.

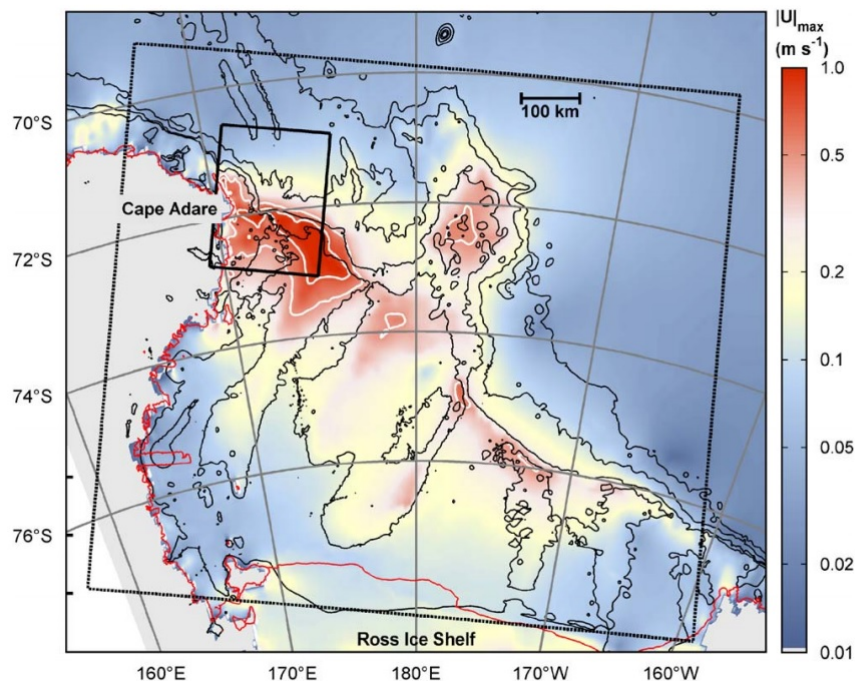


Figure 1.4: Maximum tidal current speed at the Ross Sea outflow [Padman et al., 2009].

## 1.2 The formation of dense currents

All global water bodies, including oceans, estuaries, and nearly all lakes and reservoirs that receive water from a river, have dense deep or bottom currents [Bo Pedersen, 1980]. As well as rivers, global oceans are filled with dense deep and bottom currents formed at the poles [Holland et al., 2014].

For oceans specifically, there are at least 61 known examples of dense currents around the world, with most of them resulting from the formation of dense water on a shelf (Ivanov et al. [2004]; Vilibić and Supić [2005]). The formation process and the descent of these dense water currents can happen for a number of reasons. Baines and Condie [1998] explained the stages of the formation of cold saline dense waters in the presence

of sea ice. The formation of these waters starts with the creation of dense water through convective processes due to surface cooling and rejection of brine from ice formation. The second stage involves the newly formed water mass spreading across the continental shelf (Figure 1.5) producing a boundary front at or near the shelf-break [Kuo, 1998]. The second stage is followed by a final third stage involving the geostrophic flow being steered down the slope by topographic features, or by gravity and friction, while experiencing the effect of Coriolis directing it across the slope. Figures 1.5 and 1.6 give a simple overview of the process that cold saline dense waters go through.

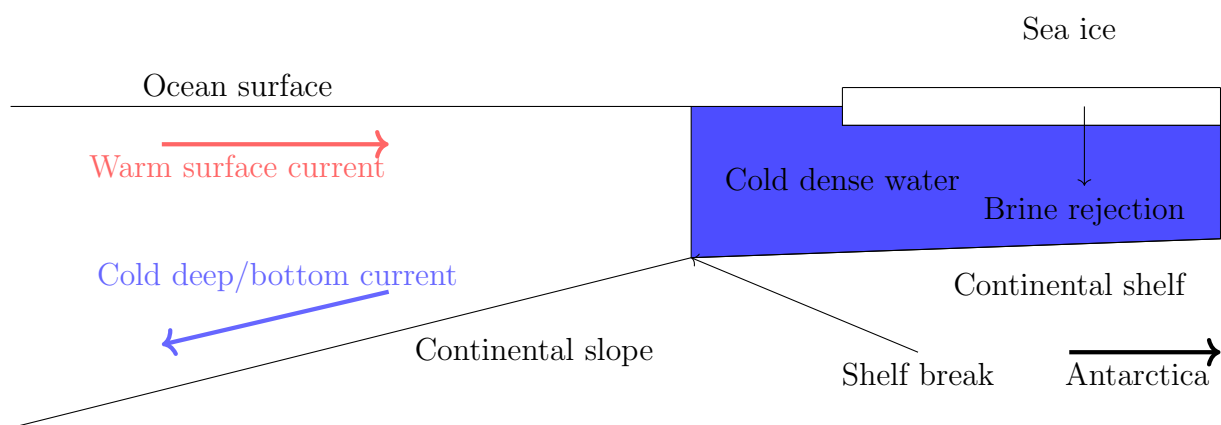


Figure 1.5: Schematic of ocean outflow near the Ross sea, showing the formation of the cold water, travelling down the continental slope, and being replaced with warmer less dense surface water.

In warm climates, conversely, Baringer and Price [1997] investigated the momentum and energy balance of the Mediterranean outflow, where the formation of dense waters was found to be caused by the intense evaporation of sea water.

The latter of the two formation mechanisms of dense currents occurs under warm conditions, whereas the first mechanism takes place under cold conditions. However, both mechanisms lead to a dense current travelling down towards the ocean bottom through a less dense ambient surrounding.

This study will focus on the behaviour of dense currents, without paying specific attention

to how the dense mass of water was generated. The model developed herein can be applied to any flow of a time-dependent bottom dense current in a rotating system.

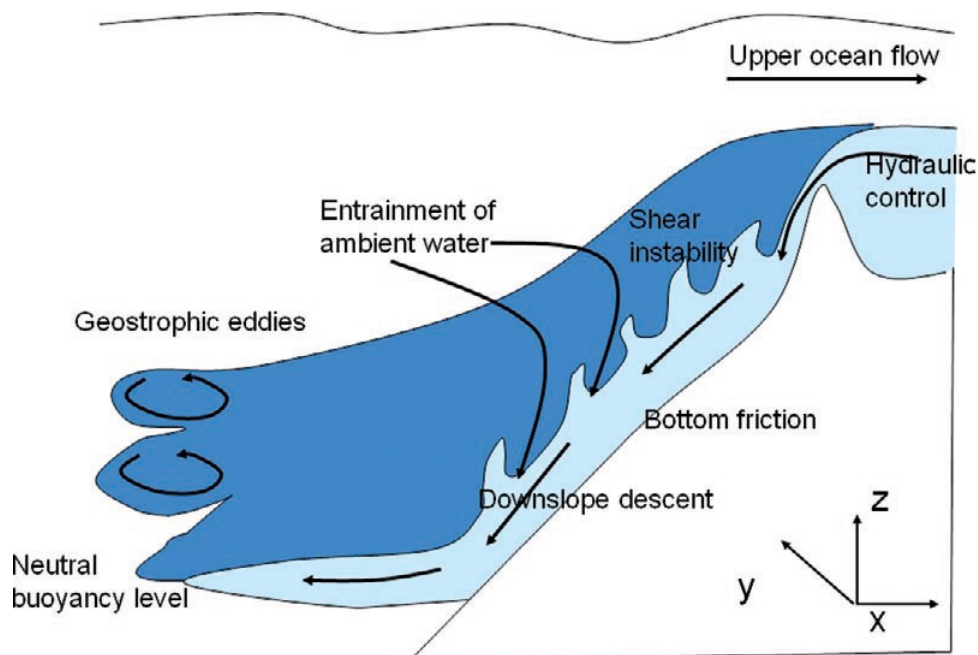


Figure 1.6: Physical processes that act upon dense currents as they travel down the continental slope through the ambient surroundings [Legg et al., 2009].

Once the dense waters are formed, they fill the sea above the continental shelf, generating a density front at the shelf break that forms the source of the dense down-slope flow (Shapiro and Hill [1997, 2003]; Jacobs [1991]; Borenäs et al. [2002]; Heggelund et al. [2004]; Wåhlin [2002, 2004]; Vilibić and Supić [2005]; Holland [2011]). The currents flow down the continental slope through the ambient surrounding and go through geostrophic adjustment as the buoyancy force driven by the density difference between the current and the ambient, is balanced by Coriolis due to the Earth’s rotation, and the current is diverted to flow along the continental slope.

While the current is travelling through the ambient, it experiences a number of physical processes. The model developed herein will be ideal for a flat continental slope with no geographical narrow channels directing the current and affecting its transport and mixing

with the ambient. In the presence of a narrow channel, the transport and mixing of the dense fluid is affected by the physical boundary of the channel, and mathematical models need to be adjusted to account for this [Girton et al., 2006]. As the dense water current descends down the continental slope, it experiences an adjustment in the velocity profile that is dependent on the density anomaly between the current and the ambient, and is also affected by the current's initial velocity leaving the shelf break [Gordon et al., 2004]. In addition to the friction processes at the ocean bed, the differences in velocities between the dense current and the ambient leads to shear instability (Figure 1.6), resulting in mixing between the two fluid bodies and entrainment from the ambient into the dense current [Ellison and Turner, 1959].

The amount of entrained fluid from the ambient into the current is a function of the current's mean velocity and density anomalies between the current and the ambient [Morton et al., 1956]. The current will continue to entrain fluid from the ambient, decreasing its mean density, and in the absence of a background density stratification the current will flow all the way to the sea bed where it will form a bottom current. In the case where a background stratification is present, and the current entrains enough ambient fluid to decrease its density to match that of the ambient, the current will level off at its neutral buoyancy level and spread into the ocean interior [Legg et al., 2006]. During these processes, the current will experience the effect of the Coriolis force and will be directed across the continental slope [Smith, 1975]. The final location of the current path will be highly influenced by the density of the ambient fluid surrounding the current. Hence, the final position of the current will depend on the strength of the ambient stratification, as well as on the strength of the Coriolis parameter acting upon the current. This study will look at these two forces and how they affect the current with both steady and unsteady source conditions.

These bottom currents play a crucial role for ecological life by being a source of oxygen,

affecting the piscatorial life in the oceans [Bo Pedersen, 1980]. Deep currents do not only play a role in the composition of the bottom waters, but the global ocean circulation pattern is driven by these currents, which in turn is responsible for the global climate [Cooper, 1955]. In addition, the transportation of sediments and formation of the sea bed topography in the oceans is affected by the behaviour of the dense bottom ocean currents, further affecting ecological life [Biscaye, 1965]. This cements the importance of correctly modelling these currents, and finding the extent of the effects that tidal motion has on them. In order to achieve this, a mathematical model will be developed, building on previously established models and adapting them to account for tidal affects on the dense currents.

### **1.3 Using a top-hat streamtube model as a coherent structure to describe dense currents**

Streamtube concepts have been used extensively in modelling flow patterns in two-dimensional domains [Bear, 2013]. Using a streamtube model to describe a current flow enables us to determine the important scales of motion, and to demonstrate the gross interaction between turbulent entrainment, bottom friction, and stratification of the ambient density field [Smith, 1975]. The currents under investigation are of turbulent behaviour. However, by using ensemble averaging, turbulent structures form a coherent structure, where a streamtube approximation could be used in order to obtain a theoretical model [Holmes et al., 1998]. One of the main assumptions adopted by Smith [1975] is that the current has a top-hat profile, where the fluid is assumed to have the same characteristics in the cross-sectional (normal to the mean flow) direction. This is a widely used approach when modelling water currents and other fluid flows (Morton et al.

[1956], Davidson [1986], Scase and Hewitt [2012]). This means that as the current entrains fluid with a different density from the ambient surroundings, the full cross-sectional area is affected instantaneously. In addition, the top-hat approach assumes that the current is symmetric about a centre axis or plane.

## 1.4 Gravity and inertial waves

Due to planetary rotation and density stratification in global ocean bodies, highly anisotropic flow structures with quasi-horizontal velocity fields tend to be produced. The turbulence dynamics under these two effects is still not fully understood [Praud et al., 2006].

In the case of a stratified fluid, without rotation, a finite column will experience a force tangential to the stratification if it was to be moved from its position, in a direction that is not normal to the stratification. The cause of this forcing is buoyancy; hence, if the column of fluid is moved down into a denser ambient surrounding, the fluid will experience a negative buoyancy force with an upward directional component. Regardless of the initial displacement, the column will try to return to its original location, but due to inertia it will overshoot, causing the buoyancy force to change direction. The column will keep oscillating about its neutral density position (assuming there is no mixing) at the buoyancy frequency of the fluid, also known as the Brunt-Väisälä frequency [Lighthill, 2001]. In the presence of drag and friction, the column oscillation will be dampened down eventually [Pedlosky, 2013]. Waves that are generated due to this mechanism are known as gravity waves [Lighthill, 2001].

The buoyancy frequency  $N$  is dependent on gravitational acceleration  $g$ , the displaced fluid density  $\rho$ , local vertical displacement  $dz$ , and the density anomaly (the density

difference between the displaced fluid and the ambient)  $d\rho$ . It is defined as:

$$(N) = \sqrt{-\frac{g}{\rho} \frac{d\rho}{dz}} \quad (1.1)$$

noting that  $\frac{d\rho}{dz}$  is the stratification rate of the fluid.

In a rotating fluid body, a small disturbance to the uniformly rotating fluid can propagate through the fluid as wave motions, as the presence of the Coriolis force bends the fluid particles' trajectory. These waves are known as inertial waves (Bjerknes et al. [1934], Phillips [1963]). Inertial waves are ever present in global oceans, where they are responsible for a substantial part of the dynamics and mixing in the interior of the supporting medium (Ogilvie and Lin [2004]); Wunsch and Ferrari [2004]; and Rabitti and Maas [2013]).

In the case of a stratified fluid, where the stratification is built by means of vertical density changes, the waves are referred to as 'internal (gravity)' waves, and despite immense interest in internal waves, their nature in confined domains is still largely unknown due to a variety of difficulties that undermine the study of their oscillations [Rabitti and Maas, 2013].

Rotating flows are characterised by a number of parameters, the most important of which are the Rossby number  $Ro = u'/(2\Omega l)$  and the Reynolds number  $Re = u'l/\nu$ , where  $u'$  is a velocity scale associated with an integral length scale of turbulence  $l$ , and  $\nu$  is the kinematic viscosity of the fluid.

Depending on the values of both the Rossby and Reynolds numbers, different regimes would exist in the flow. Figure 1.7, originally (Fig.1) in Godefert and Moisy [2015], illustrates these regimes in terms of the two parameters. Inertial waves are found to dominate flows that have a low Reynolds number with a vanishing Rossby number.

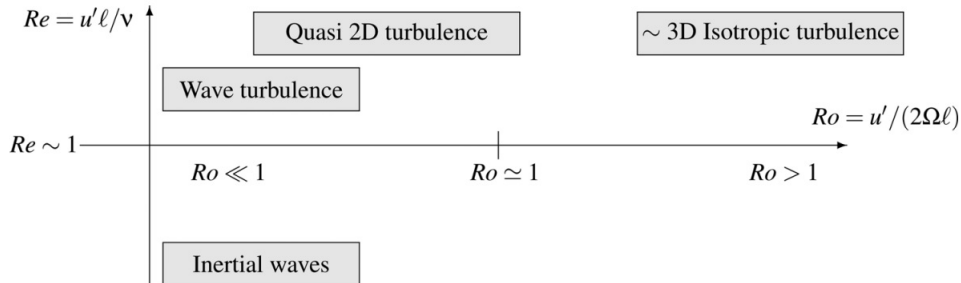


Figure 1.7: Schematic showing different regimes of rotating turbulence in Rossby-Reynolds parametric plane [Godeferd and Moisy, 2015].

Inertial ‘internal’ waves have also been observed in cases of internal tides, where the tidal motion causes the waves to propagate along the ocean’s internal stratification [Alford, 2003]. The breaking of such waves contributes significantly to ocean mixing, affecting marine productivity and global climate. The energy released during the breaking of these waves is thought to fuel the turbulence required to upwell the warm waters in the oceans’ Thermohaline circulation [Alford, 2003]. Holland et al. [2014] showed that the breaking of internal waves in a dense current that is generated from a pulsed source can happen at a geophysically relevant distance down-stream. It was shown that the distance at which the waves break is closer to the source for higher amplitude and shorter period perturbations. The nature of these waves in rotating flows remains unclear.

With the presence of a background ambient density stratification, the rotating dense current experiences internal waves that appear on the interface between the current and the ambient. The nature of these waves has been of immense research interest due to the effects the waves have on enhancing the mixing between the current and the ambient, hence, affecting the current’s propagation (Sutherland et al. [2004]; Ezer [2006]; Wählín and Cenedese [2006]; Wells [2007]; Cenedese and Adduce [2008]). The mixing dynamics of the dense currents have been studied both numerically using ocean models (Jiang and Garwood Jr [1996]; Jungclaus et al. [2001]; Käse et al. [2003]; Ezer [2005]; Özgökmen et al.

[2006]; Legg et al. [2006]; Xu et al. [2006]), and experimentally (Cenedese et al. [2004]; Cenedese and Adduce [2008]). Both the numerical and experimental approaches focused on the mixing features of the current, where the three dimensional structure of the current propagation were of interest. Jiang and Garwood Jr [1996], and Jungclaus et al. [2001], found that the dense current becomes unstable dynamically, and breaks into smaller sub-currents due to the baroclinic instability and bottom friction deforming the current. However, under the assumption of a ‘top-hat’ profile across the current cross-sectional area, density differences in the cross-sectional direction of the current are neglected, and the density is assumed constant. The ‘top-hat’ assumption only considers density differences between the current (as one structure) and the ambient. These assumptions do not allow for baroclinic instability to arise.

In the absence of tidal motion, and in the case of a steady state buoyancy driven current through a homogeneous ambient, the buoyancy and Coriolis forces reach a balance, and the current flow approaches a state of geostrophic equilibrium [Griffiths, 1986].

## **1.5 Laboratory experiments for rotating gravity currents**

This section presents some of the examples that used an experimental approach in an attempt to model rotating dense currents.

A newly formed current from a steady state source would settle after some time into a steady state current that is statistically independent of time. During the initial stages of the flow, the current can be divided into two sections, the nose and the main body of the current [Cenedese et al., 2004]. The characteristics of the nose are of interest only when studying the initial stages of the current. This study will be focusing on the

characteristics of the current's body, as it will deal with existing currents and the effects a change of source conditions has on them.

According to Cenedese et al. [2004], the rotating dense current can be one of three types: laminar regime, wave regime, and wave regime with the formation of eddies. In the laminar regime, the dense current has a constant thickness behind the head, whereas the wave regime has wave-like disturbances appearing at the interface between the dense current and the ambient fluid. In the eddy regime, periodic formation of cyclonic eddies appear in the overlying ambient fluid. From experimental analysis and comparison with oceanographic data, it was found that ocean gravity driven currents lie within the second type of flow, (wave regime). This flow was found to form for values of Froude number higher than 1, defined as  $Fr = U / \sqrt{g' H \cos \theta}$ , where  $U$  and  $H$  are the velocity and height of the dense current respectively,  $g' = g \frac{\Delta \rho}{\rho_0}$  is the reduced gravity,  $g$  is acceleration due to gravity,  $\Delta \rho$  is the density anomaly between the current and the ambient,  $\rho_0$  is the reference density, and  $\theta$  is the angle of the slope which the current is travelling down. This is consistent with the Froude number values for deep and bottom ocean currents (Simpson [1982]; Armi [1978]).

Experiments carried out in laboratories in order to study the behaviour of gravity currents moving down slopes in rotating systems have provided valuable information on the characteristics of these currents. The results obtained from the experimental analysis of gravity currents have been an impetus for the theoretical studies. Previous experiments have focused on the frontal waves of the current, covering the initial stages of the current descending the slope [Griffiths, 1986]. The purpose of this study is to develop a time-dependent model that will study the effect of variation of properties at the source for pre-existing currents, and how the steady state solutions compare with the new unsteady findings. Most experimental studies that have covered the behaviour of gravity currents in rotating systems have given a description of the current's body [Griffiths, 1986]. No

study to date describes a full mathematical model for an unsteady dense current in a rotating system.

Under the condition that the current source experiences a step change in the properties, the current would be split into three qualitatively different regions of behaviour [Scase et al., 2006]. The furthest region from the source remains unaffected by the change at the source. The region closest to the source is effectively a new steady current based on the final properties of the current source. The third region is the transitional region, in which the current adjusts between the state of the first two regions. If the change of source properties is continuous, there will only be one region, which is the transitional region as the current body is continuously adjusting to the change in the source conditions. This study will look at the latter case, where the source properties are continuously changing.

Since both time-dependent models developed by Scase et al. [2006] and Holland [2011] had no rotation, it will have to be determined if the rate of change of properties causes the introduction of a new current nose/head in the case of the rotating system. This is due to the impact it will have on the direction of the investigation to include some modified properties for a certain time scale. For the purposes of the current study, it is assumed that no nose is present. This study will focus on the response of an established current to temporal variations of the upstream source conditions.

## **1.6 Aims and objectives**

This study is a response to the current need to identify and develop a mathematical model that builds on previous work, in an attempt to understand the effects that time-dependent source conditions of dense gravity currents have on the properties of the down-stream propagation of those currents in rotating systems.

The aim of this thesis is to study and understand the effect that time varying source conditions have on deep ocean dense currents, and how the current down-stream behaviour is affected by the changes at the source, from both temporal and space domain perspectives.

In order to achieve the aims of this study, a good understanding of the mathematical models used in the past to describe steady state currents in rotating systems is necessary. Carrying on from this understanding will be a proposed technique and approach in order to solve the problem.

## 1.7 Outline of thesis

This thesis is divided into six chapters, including the Introduction. Chapter 2 gives an overview of the research carried out prior to the new model. Focusing on numerical modelling approaches, it mainly highlights the work done by Smith [1975], who produced the steady state streamtube model that this research project is based on. The extensive work done by Scase et al. [2006] in order to change the classical Morton et al. [1956] rising plume to the unsteady version is briefly summarised, as it will form the basis of extending the work of Smith [1975] to reach the full unsteady model. Chapter 2 also covers the derivation of the new model, starting from the Euler and incompressibility equations, leading to the derivation of the full integral dynamical system of equations.

In Chapter 3, firstly the numerical methods used to produce the results are explained before the newly-derived system is used to reproduce the results from the Mediterranean outflow covered in Smith [1975]. The effects of changing the current's initial cross-sectional area, velocity, density, and direction (pitch angle), on the current's propagation through a homogeneous ambient are then studied. The four variables of the current (cross-sectional area, velocity, density, and direction) are referred to in this thesis as the current's state

variables. In addition to the state variables, the effects of changing the rotational rate (Coriolis parameter), the drag and entrainment coefficients, and the slope angle, on a dense current in a homogeneous ambient, are also investigated in Chapter 3. The four parameters of the of the system, excluding the ambient stratification are referred to as ‘state parameters’.

Chapter 4 starts by looking at the effects that introducing a background density stratification to the ambient have on a steady state streamtube dense current, covering the new findings of the oscillations of the steady state currents, and looks into what controls these oscillations. Each of the rotational rate, and drag and entrainment coefficients effects are investigated. The frequencies of these waves are then related to the ambient stratification buoyancy frequencies, before a final study illustrates the limiting cases of when these oscillations appear.

The unsteady system is then used to present the new findings in Chapter 5. In line with recent research, the stability of the model is tested numerically to start with. After that the Mediterranean outflow from Smith [1975] is used as the base case, and the current source is oscillated by changing the initial state variables. The current down-stream response is measured, and full space-time envelopes of the current’s propagation as well as the envelopes of the current’s state variables are shown. The time-dependent results are then compared with the steady state results which are produced using the limits between which the source was oscillated.

Chapter 6 concludes the thesis by presenting the novel findings of the present study, and drawing the path for the future work suggested.

# Chapter 2

## Theory

### 2.1 Derivation outline

This chapter will cover the derivation of the time-dependent (unsteady) system of dense current evolution equations. The derivation follows on from the work carried out by Smith [1975], and by implementing a full mathematical derivation similar to that employed by Scase et al. [2006] the full unsteady streamtube model for bottom dense currents will be derived.

### 2.2 Introduction

Most work preceding that of Smith [1975], such as studies carried out by Cooper [1961], Lee and Ellett [1965], and Worthington [1969], followed an experimental approach. Smith [1975] provided the first full system for explaining the dynamics behind these currents. However, this system falls short when temporal fluctuations arise. With observations showing that these currents are affected on a temporal level by tidal motion (Middleton

et al. [1982]; Middleton et al. [1987]; Cutchin and Smith [1973]; Whitworth and Orsi [2006]; Muench et al. [2009]; Padman et al. [2009]; Wang et al. [2010]), this has made it even more critical to understand how these currents are affected by the temporal change of their source conditions.

Before presenting the derivation of the model, we overview the models of Smith [1975] and Scase et al. [2006] to give a better background of the current knowledge of modelling deep bottom currents, and how to take this into the time-dependent domain.

## 2.3 Background studies

Morton et al. [1956] gave one of the first descriptions for the properties and characteristics of a turbulent plume. The dynamics of dense bottom currents have since been modelled using both theoretical and experimental methods. Attempts started with Ellison and Turner [1959], where the motion of a layer of fluid lighter than its surroundings flowing up a sloping roof (or a heavier fluid than the ambient flowing down a sloping floor) was modelled both experimentally and theoretically. A number of studies followed, all based on the entrainment law of Morton et al. [1956], that the motion of fluid through an ambient of a different density is governed by the rate at which that current entrains fluid from that ambient, and the entrainment is taken to be proportional to the mean velocity of the current. The Ellison and Turner [1959] theory states that the entrainment rate into a current is a function of the current's mean velocity multiplied by an empirical function of the Richardson number of the current. All of these studies only included modelling of the spatial domain of the flow, while temporal changes of the source were never considered. However, the model by Morton et al. [1956] was later developed by Scase et al. [2006] in order to allow for time dependency, enabling the modelling of unsteady flow cases. In addition, Holland [2011] provided a time-dependent model based on the steady model of

Ellison and Turner [1959]. The approach taken by Scase et al. [2006] was used here in order to adapt the streamtube model by Smith [1975] to produce an unsteady system for deep dense ocean currents.

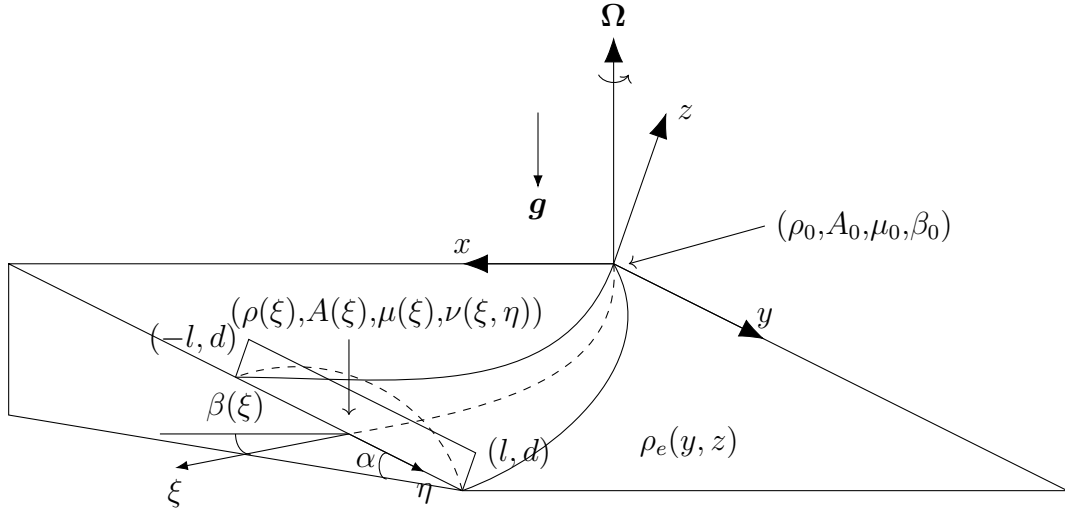


Figure 2.1: A schematic showing the streamtube model geometry

The study by Smith [1975] was one of the first studies to account for the effect of rotation on dense currents. Smith [1975] used a streamtube model to study the characteristics and properties of a steady, well-mixed deep boundary current in a rotating, stratified ocean.

The schematic shown in Figure 2.1 shows the geometrical aspects of the model used in Smith [1975]. The continental slope is represented here by the  $(x,y)$  plane, and is inclined to the horizontal at an angle  $\alpha$ , with  $z$  normal to the inclined  $(x,y)$  plane. The current is modelled using a second coordinate system which is a set of streamwise coordinates  $(\xi,\eta)$ . The rotational and gravity vectors,  $\mathbf{\Omega}$  and  $\mathbf{g}$  respectively, are aligned vertically to the horizontal plane.

Smith [1975] used empirical relations for parameterising the entrainment and frictional effects. The dynamical streamtube model was used to describe the integral flow properties of steady dense currents, to determine the important scales of motion, and to demonstrate

the gross interaction among turbulent entrainment  $E_0$ , bottom friction  $K$  and stratification of the ambient density field  $T$ . This approach led to the associated proportionality constants  $(E_0, K)$  being evaluated and determined for the Norwegian outflow through the Denmark Strait and for the Mediterranean outflow. This evaluation was achieved by comparing the model solution to hydrographic and current metre data collected from the flows under study, and varying the parameters in order to fit the model to the collected data. The entrainment law used in the model by Smith was based on Ellison and Turner [1959], and the bottom friction effects were represented by a quadratic drag law. Smith [1975] found that both the Norwegian and Mediterranean Outflows are characterised by the effects of turbulent friction and entrainment. The properties and local dynamics of the current near the source are dominated by strong turbulent friction and entrainment.

The current is modelled under the assumption that it has a rectangular cross-sectional area, and that the ratio of the height to the width of the current does not vary with the current's downstream distance. In addition to this assumption, a "top hat" approach was used. The top-hat approach assumes that the characteristics of the current in the cross-sectional direction are the same. Hence, as the current entrains fluid from the ambient, the entrained fluid will mix with the current fluid, changing the characteristics of the whole cross-section instantaneously.

It is useful here to cover the assumptions made by Smith [1975], upon which the stream-tube model was based:

- The bottom slope is assumed to be small ( $s = \tan \alpha \ll 1$ ).
- The fields of excess density and turbulence are concentrated near the bottom in a thin layer.
- Within the stress and pressure fields, variations normal to the bottom exceed those in the tangential directions:  $(\frac{\partial}{\partial z} \gg \frac{\partial}{\partial x}, \frac{\partial}{\partial y})$ .

- Vertical velocities and stresses are small. Hence, the reduced pressure field is nearly hydrostatic.
- A strong axial velocity dominates the component in the cross-stream direction, and the Reynolds stresses are related to the intensity of the mean current in the axial direction.
- The velocity and excess density fields are confined to the current region adjacent to the slope bottom. Within this region, variations in the density and velocity are negligible. From this assumption, the structure of the turbulence and specifically the frictional stresses and rate of entrainment may be related solely to the mean velocity and density contrast. For convenience, these properties were assumed to be uniform over a cross-section (top-hat).
- The aspect ratio of the cross-section is small, meaning that the pressure gradient terms are negligible with respect to the gravitational acceleration.
- The current is narrow (the cross-stream scale is much less than the local radius of the curvature of the stream axis).

The dynamical equations for the Smith [1975] model, are given in terms of the current downstream distance ( $\xi$ ), the mean velocity of the current  $V(\xi)$ , the density contrast between the current and the ambient fluid  $\Delta\rho(\xi)$ , the current's cross-sectional area  $A(\xi)$ , and the mean direction of the current given by the angle  $\beta$  which it makes with the positive  $x$  direction. The parameters appearing in the equations are the entrainment and frictional coefficients  $(E_0, K)$ , the bottom slope  $s$  ( $s = \tan \alpha$ ) where  $\alpha$  is the angle of the slope, the normal components of the Coriolis parameter  $\hat{f} = 2|\Omega| \cos \alpha$ , and gravity  $\hat{g}$  ( $\hat{g} = |g| \cos \alpha$ ).  $\hat{T}$  is the stratification rate normal to the plane in the ambient region, and  $\rho_e$  is the ambient density. The entrainment and frictional coefficients  $(E_0, K)$  have dimensions of length because of the integration performed in the cross-stream direction.

The streamtube model in the integral form is:

$$\frac{d}{d\xi}(AV) = E_0V, \quad (2.1)$$

$$\frac{d}{d\xi}(\rho AV) = \rho_e E_0V, \quad (2.2)$$

$$\rho V(\hat{f} + V\frac{d\beta}{d\xi}) = s\hat{g}\Delta\rho \cos\beta, \quad (2.3)$$

$$\frac{d}{d\xi}(\rho AV^2) = s\hat{g}\Delta\rho A \sin\beta - \rho KV^2. \quad (2.4)$$

Where:

$$\Delta\rho = \rho(\xi) - \rho_e(\xi), \quad (2.5)$$

$$\rho_e(\xi) = \rho_0[1 + s\hat{T}Y(\xi)]. \quad (2.6)$$

The steady results obtained by Smith [1975] for the Mediterranean outflow were reproduced using the new unsteady streamtube code. A numerical finite difference method was used to solve the equations with the given source conditions.

There is no existing simple model that allows for time-dependency for dense currents in rotating systems. This study will use the same approach used by Scase et al. [2006] and apply it to Smith's steady streamtube model in order to establish an unsteady streamtube model. Before this is carried out, it is useful to predict what the finished model will be like, or what the solutions from the limiting steady conditions are. This can be achieved using Smith's steady streamtube, and by solving a number of steady state currents using numerical methods while varying the steady source conditions. This enables the understanding of the physics of the currents, and gives an indication of how the current path and downstream properties would react to changing certain properties at the source.

Smith [1975] evaluated the entrainment and friction coefficients by matching the steady

streamtube model to hydro-graphic data from the Norwegian Overflow through the Denmark Strait and the Mediterranean Outflow. The latter was chosen here to study the effects of varying the characteristics of the current at the source on the downstream properties. This was achieved by changing the initial state variables at the current source. For consistency, the rest of the conditions and parameters of the dense currents of results presented in this thesis will use the Mediterranean outflow initial conditions presented by Smith [1975].

## 2.4 The unsteady model

### 2.4.1 Formulation

First of all, the incompressibility equation  $\nabla \cdot \mathbf{u} = 0$  is considered, and the assumptions made by Scase et al. [2006] are followed: that this stands for both the current and ambient fluids when described together. However, if the current fluid is to be expressed on its own, then it is observed that it expands with the rate of entrainment, whilst the ambient fluid is decreasing at the same rate. Therefore, for the current fluid at a certain time and distance,  $\nabla \cdot \mathbf{u} =$  the amount of fluid entrained per unit length. By integrating over the cross-sectional area of the current, the amount of fluid entrained is found to be equal to the constant of entrainment multiplied by the mean velocity of the current, where the constant of entrainment here has units of length due to the integration performed in the cross-stream direction [Smith, 1975]. For a current with a rectangular cross-sectional area  $\mathcal{D} = [-l, l] \times [0, d]$ , where  $(\eta, z) \in [-l, l] \times [0, d]$ , a velocity  $\mu$  in the streamwise direction, an entrainment coefficient  $E_0$ , and a density  $\rho$ , travelling through an ambient with a density

$\rho_e$ , the divergence of the velocity field vector  $\mathbf{u}$  is given by:

$$\int_{\mathcal{D}} \nabla \cdot \mathbf{u} \, dA = E_0 \mu, \quad (2.7)$$

and the mass conservation equation is given by:

$$\int_{\mathcal{D}} \left( \frac{D\rho}{Dt} \right) \, dA = E_0 \mu (\rho_e - \rho). \quad (2.8)$$

Equation 2.8 states that as we follow the density of the current downstream while it entrains ambient fluid, the current density will change as a function of the amount of fluid entrained as well as the density anomaly between the current and the ambient (if  $\rho_e = \rho$  the density does not change).

These two assumptions will be revisited in subsection 2.4.6.

The derivation is started by defining the coordinate system  $(x_s, y_s, z_s)$ , with a rotational rate  $\mathbf{\Omega}$  acting about the  $z_s$  axis, and gravitational acceleration  $\mathbf{g}$  acting in the negative  $z_s$  direction. The coordinate system is then rotated about the  $x_s$  axis with an angle  $\alpha$ , to the ‘slope coordinate’ system  $(x, y, z)$  (SC hereafter), noting that  $x_s$  is the same as  $x$ , and the continental slope is in the  $(x, y)$  plane. A second transformation of coordinates is then applied, where the motion is described in terms of the ‘path-relative’ axes system  $(\xi, \eta, z)$  (PC hereafter), where  $\xi$  is the streamwise direction, and  $\eta$  is in the spanwise direction, and is locally perpendicular to  $\xi$  in the  $(x, y)$  plane, and  $\mu$ ,  $\nu$ , and  $w$  are defined as the velocities in the streamwise ( $\xi$ -direction), spanwise ( $\eta$ -direction), and perpendicular to the slope ( $z$ -direction) respectively.  $z$  remains the same, perpendicular to the  $(x, y)$  plane, as well as the path relative axes  $(\xi, \eta)$ . Making use of Reynolds [1895], Reynolds averaging is then applied, in order to account for small-scale fluctuations that can be

ensemble averaged over time to describe the average (mean) state of motion in the current (Germano [1992];Randall [2015]). The equations are then non-dimensionalised in order to quantify the order of magnitude of the individual terms, allowing the conclusion of which terms dominate the flow of the current.

## 2.4.2 Rotating into the continental slope coordinate system

Taking the incompressibility and Euler equations in the coordinates  $(x_s, y_s, z_s, t)$  with gravity aligned in the negative  $z_s$ -direction, and rotational vector  $\mathbf{f} = 2\mathbf{\Omega}$ :

$$\nabla \cdot \mathbf{u}_s = 0, \quad (2.9)$$

$$\frac{D\mathbf{u}_s}{Dt} = -\frac{1}{\rho}\nabla p + \mathbf{g} - \mathbf{\Omega} \times (\mathbf{\Omega} \times \mathbf{x}_s) - 2\mathbf{\Omega} \times \mathbf{u}_s, \quad (2.10)$$

where the velocity field  $\mathbf{u}_s = (u_s, v_s, w_s)$ ,  $\rho$  is the density,  $\mathbf{g} = (0, 0, -g) = -g\mathbf{e}_{z_s}$  is the acceleration due to gravity, and  $\mathbf{e}_{z_s}$  is the unit vector in the  $z_s$  direction.

The density can be decomposed such that the current outflow density  $\rho(\mathbf{x}_s, t) = \rho_e(\mathbf{x}_s) + \Delta\rho(\mathbf{x}_s, t)$ , where  $\rho_e(\mathbf{x}_s)$  is the background ambient density. Smith [1975] makes a Boussinesq approximation [Boussinesq, 1903], such that for some constant background ambient density  $\rho_0$ ,  $\rho_0 = \rho_e = \rho$  unless the term is multiplied by gravity. Hence, Equation 2.10 can be written as:

$$\frac{D\mathbf{u}_s}{Dt} \approx -\frac{1}{\rho_0}\nabla p + \frac{[\rho_e(\mathbf{x}_s) + \Delta\rho(\mathbf{x}_s, t)]}{\rho_0}\mathbf{g} - \mathbf{\Omega} \times (\mathbf{\Omega} \times \mathbf{x}_s) - 2\mathbf{\Omega} \times \mathbf{u}_s. \quad (2.11)$$

Taking the background ambient density,  $\rho_e$ , to be vertically stratified such that,  $\rho_e(\mathbf{x}_s) =$

$\rho_e(z_s)$ , and using a dummy variable  $\zeta$ , then the ‘modified pressure’,  $p'(\mathbf{x}_s, t)$ , may be defined as:

$$p'(\mathbf{x}_s, t) = p(\mathbf{x}_s, t) + \int^z \rho_e(\zeta)g \, d\zeta. \quad (2.12)$$

Substituting into the Euler equation in a rotating frame (Equation 2.11), under the Boussinesq approximation applied by Smith [1975], and dropping the approximation sign:

$$\frac{D\mathbf{u}_s}{Dt} = -\frac{1}{\rho_0}\nabla p' + \frac{\Delta\rho(\mathbf{x}_s, t)}{\rho_0}\mathbf{g} - \boldsymbol{\Omega} \times (\boldsymbol{\Omega} \times \mathbf{x}_s) - 2\boldsymbol{\Omega} \times \mathbf{u}_s. \quad (2.13)$$

Noting that for general rotation pseudo-vector  $\boldsymbol{\Omega}$ , that

$$\nabla\left\{\frac{1}{2}\left[(\boldsymbol{\Omega} \cdot \mathbf{x}_s)^2 - |\boldsymbol{\Omega}|^2|\mathbf{x}_s|^2\right]\right\} = (\boldsymbol{\Omega} \cdot \mathbf{x}_s)\boldsymbol{\Omega} - |\boldsymbol{\Omega}|^2\mathbf{x}_s = \boldsymbol{\Omega} \times (\boldsymbol{\Omega} \times \mathbf{x}_s), \quad (2.14)$$

and writing a rotating modified pressure:

$$P = p + \int^z \rho_e(\zeta)g \, d\zeta + \frac{\rho_0}{2}\left[(\boldsymbol{\Omega} \cdot \mathbf{x}_s)^2 - |\boldsymbol{\Omega}|^2|\mathbf{x}_s|^2\right], \quad (2.15)$$

rearranging Equation 2.15 gives:

$$\frac{1}{2}\left[(\boldsymbol{\Omega} \cdot \mathbf{x}_s)^2 - |\boldsymbol{\Omega}|^2|\mathbf{x}_s|^2\right] = \frac{P}{\rho_0} - \frac{p}{\rho_0} + \frac{1}{\rho_0} \int^z \rho_e(\zeta)g \, d\zeta. \quad (2.16)$$

Substituting Equation 2.15 into the rhs of Equation 2.14, gives:

$$\boldsymbol{\Omega} \times (\boldsymbol{\Omega} \times \mathbf{x}_s) = \nabla\left[\frac{P}{\rho_0} - \frac{p}{\rho_0} + \frac{1}{\rho_0} \int^z \rho_e(\zeta)g \, d\zeta\right]. \quad (2.17)$$

Using Equation 2.12, and Equation 2.17 to substitute the first and third terms on the lhs of Equation 2.13 respectively, then the Euler equation can be written as:

$$\frac{D\mathbf{u}_s}{Dt} = -\frac{1}{\rho_0}\nabla P + \frac{\Delta\rho}{\rho_0}\mathbf{g} - 2\boldsymbol{\Omega} \times \mathbf{u}_s. \quad (2.18)$$

We now rotationally transform the equations into the SC system  $(x, y, z)$ , by rotating about the  $x_s$ -axis through an angle of  $\alpha$ , where the rotational matrix  $\mathbf{R}_s$  is given by:

$$\mathbf{R}_s = -g \begin{pmatrix} 1 & 0 & 0 \\ 0 & \cos \alpha & -\sin \alpha \\ 0 & \sin \alpha & \cos \alpha \end{pmatrix}. \quad (2.19)$$

This transformation only causes the direction of gravity to be changed, as  $\boldsymbol{\Omega}$  was kept general as shown in Equation 2.14. Thus:

$$\mathbf{g} = -g\mathbf{e}_{z_s} \mapsto -g \begin{pmatrix} 1 & 0 & 0 \\ 0 & \cos \alpha & -\sin \alpha \\ 0 & \sin \alpha & \cos \alpha \end{pmatrix} \begin{pmatrix} 0 \\ 0 \\ 1 \end{pmatrix} = -g \begin{pmatrix} 0 \\ -\sin \alpha \\ \cos \alpha \end{pmatrix} := \mathbf{g}_\alpha. \quad (2.20)$$

Defining the rotation pseudo-vector in the original non-rotated coordinates by  $\boldsymbol{\Omega} =$

$\Omega(\sin \theta \cos \phi, \sin \theta \sin \phi, \cos \theta)$ , where  $\phi$  is the azimuth and  $\theta$  is the inclination, then

$$\begin{aligned} \boldsymbol{\Omega} &\mapsto \Omega \begin{pmatrix} 1 & 0 & 0 \\ 0 & \cos \alpha & -\sin \alpha \\ 0 & \sin \alpha & \cos \alpha \end{pmatrix} \begin{pmatrix} \sin \theta \cos \phi \\ \sin \theta \sin \phi \\ \cos \theta \end{pmatrix} \\ &= \Omega \begin{pmatrix} \sin \theta \cos \phi \\ \cos \alpha \sin \theta \sin \phi - \sin \alpha \cos \theta \\ \cos \alpha \cos \theta + \sin \alpha \sin \theta \sin \phi \end{pmatrix} := \boldsymbol{\Omega}_\alpha. \end{aligned} \quad (2.21)$$

Note:  $|\mathbf{g}_\alpha| = g$ , and  $|\boldsymbol{\Omega}_\alpha| = \Omega$ . This thesis will primarily focus on the case where:  $\boldsymbol{\Omega} \propto \mathbf{g}$ , i.e.,  $\theta = 0$ .

Hence, the governing equations in the SC system, for a velocity field  $\mathbf{u} = (u, v, w)$ , in the axes system  $(x, y, z)$ , are given by:

$$\nabla \cdot \mathbf{u} = 0, \quad (2.22)$$

$$\frac{D\mathbf{u}}{Dt} = -\frac{1}{\rho} \nabla P + \frac{\Delta \rho}{\rho_0} \mathbf{g}_\alpha - 2\boldsymbol{\Omega}_\alpha \times \mathbf{u}, \quad (2.23)$$

where  $P$ ,  $\mathbf{g}_\alpha$ , and  $\boldsymbol{\Omega}_\alpha$  are defined as above.  $x$  is along the slope, perpendicular to the right as we look directly down the slope.  $y$  is down the slope, perpendicular to  $x$ , and  $z$  is normal to the slope. Note that this is the same coordinate system used by Smith [1975] and shown in Figure 2.1.

The third term on the rhs of Equation 2.23 can be decomposed into a magnitude and

direction using :  $\boldsymbol{\Omega}_\alpha = \Omega \hat{\boldsymbol{\Omega}}_\alpha$ , such as:

$$\begin{aligned}
2\boldsymbol{\Omega}_\alpha \times \mathbf{u} &= 2\Omega \begin{vmatrix} \mathbf{e}_x & \mathbf{e}_y & \mathbf{e}_z \\ \hat{\Omega}_{\alpha 1} & \hat{\Omega}_{\alpha 2} & \hat{\Omega}_{\alpha 3} \\ u & v & w \end{vmatrix} \\
&= f \left( \hat{\Omega}_{\alpha 2} w - \hat{\Omega}_{\alpha 3} v, \hat{\Omega}_{\alpha 3} u - \hat{\Omega}_{\alpha 1} w, \hat{\Omega}_{\alpha 1} v - \hat{\Omega}_{\alpha 2} u \right).
\end{aligned} \tag{2.24}$$

where  $f = 2\Omega$ ,  $\hat{\Omega}_{\alpha 1} = \sin \theta \cos \phi$ ,  $\hat{\Omega}_{\alpha 2} = \cos \alpha \sin \theta \sin \phi + \sin \alpha \cos \theta$ , and  $\hat{\Omega}_{\alpha 3} = \cos \alpha \cos \theta - \sin \alpha \sin \theta \sin \phi$ .

### 2.4.3 Reynolds averaging

Denoting the ensemble average of a quantity with  $\langle \cdot \rangle$ , each quantity may be decomposed into a ‘mean part’ and a ‘fluctuating part’, e.g.,  $u = \langle u \rangle + u'$ , where  $u'$  is chosen such that  $\langle u' \rangle = 0$ . The incompressibility condition is therefore:

$$\begin{aligned}
\nabla \cdot \mathbf{u} = 0 &\Rightarrow \frac{\partial u}{\partial x} + \frac{\partial v}{\partial y} + \frac{\partial w}{\partial z} = 0 \\
&\Rightarrow \frac{\partial}{\partial x} (\langle u \rangle + u') + \frac{\partial}{\partial y} (\langle v \rangle + v') + \frac{\partial}{\partial z} (\langle w \rangle + w') = 0.
\end{aligned} \tag{2.25}$$

Therefore ensemble averaging over Equation 2.25, and making use of  $\langle \langle \cdot \rangle \rangle = \langle \cdot \rangle$ , gives:

$$\frac{\partial \langle u \rangle}{\partial x} + \frac{\partial \langle v \rangle}{\partial y} + \frac{\partial \langle w \rangle}{\partial z} = 0, \tag{2.26}$$

and therefore,

$$\frac{\partial u'}{\partial x} + \frac{\partial v'}{\partial y} + \frac{\partial w'}{\partial z} = 0. \quad (2.27)$$

Taking the first component (the  $x$  direction) of the momentum equation (Equation 2.23), and making use of Equation 2.24, gives:

$$\frac{\partial u}{\partial t} + u \frac{\partial u}{\partial x} + v \frac{\partial u}{\partial y} + w \frac{\partial u}{\partial z} + f(\hat{\Omega}_{\alpha 2} w - \hat{\Omega}_{\alpha 3} v) = -\frac{1}{\rho_0} \frac{\partial P}{\partial x}, \quad (2.28)$$

decomposing Equation 2.28 to ‘mean’ and ‘fluctuating’ parts:

$$\begin{aligned} & \frac{\partial u}{\partial t} (\langle u \rangle + u') + (\langle u \rangle + u') \frac{\partial}{\partial x} (\langle u \rangle + u') + (\langle v \rangle + v') \frac{\partial}{\partial y} (\langle u \rangle + u') \\ & + (\langle w \rangle + w') \frac{\partial}{\partial z} (\langle u \rangle + u') + f \left( \hat{\Omega}_{\alpha 2} (\langle w \rangle + w') - \hat{\Omega}_{\alpha 3} (\langle v \rangle + v') \right) \\ & = -\frac{1}{\rho_0} \frac{\partial}{\partial x} (\langle P \rangle + P'). \end{aligned} \quad (2.29)$$

Expanding, and rearranging Equation 2.29, gives:

$$\begin{aligned} & \frac{\partial \langle u \rangle}{\partial t} + \left[ \langle u \rangle \frac{\partial}{\partial x} + \langle v \rangle \frac{\partial}{\partial y} + \langle w \rangle \frac{\partial}{\partial z} \right] \langle u \rangle + \\ & \frac{\partial u'}{\partial t} + \left[ \langle u \rangle \frac{\partial}{\partial x} + \langle v \rangle \frac{\partial}{\partial y} + \langle w \rangle \frac{\partial}{\partial z} \right] u' \\ & + \left[ u' \frac{\partial}{\partial x} + v' \frac{\partial}{\partial y} + w' \frac{\partial}{\partial z} \right] \langle u \rangle + \left[ u' \frac{\partial}{\partial x} + v' \frac{\partial}{\partial y} + w' \frac{\partial}{\partial z} \right] u' \\ & + f \left( \hat{\Omega}_{\alpha 2} (\langle w \rangle + w') - \hat{\Omega}_{\alpha 3} (\langle v \rangle + v') \right) \\ & = -\frac{1}{\rho_0} \frac{\partial \langle P \rangle}{\partial x} - \frac{1}{\rho_0} \frac{\partial P'}{\partial x}. \end{aligned} \quad (2.30)$$

Taking the 6th term in Equation 2.30, from the product rule we note that:

$$\begin{aligned} \left[ u' \frac{\partial}{\partial x} + v' \frac{\partial}{\partial y} + w' \frac{\partial}{\partial z} \right] u' = \\ \frac{\partial u' u'}{\partial x} + \frac{\partial u' v'}{\partial y} + \frac{\partial u' w'}{\partial z} - u' \left[ \frac{\partial u'}{\partial x} + \frac{\partial v'}{\partial y} + \frac{\partial w'}{\partial z} \right], \end{aligned} \quad (2.31)$$

where the 2nd term on the rhs is equal to zero from Equation 2.27.

Substituting Equation 2.31 into Equation 2.30 gives:

$$\begin{aligned} \frac{\partial \langle u \rangle}{\partial t} + \left[ \langle u \rangle \frac{\partial}{\partial x} + \langle v \rangle \frac{\partial}{\partial y} + \langle w \rangle \frac{\partial}{\partial z} \right] \langle u \rangle + \frac{\partial u'}{\partial t} \\ + \left[ \langle u \rangle \frac{\partial}{\partial x} + \langle v \rangle \frac{\partial}{\partial y} + \langle w \rangle \frac{\partial}{\partial z} \right] u' \\ + \left[ u' \frac{\partial}{\partial x} + v' \frac{\partial}{\partial y} + w' \frac{\partial}{\partial z} \right] \langle u \rangle + \frac{\partial u' u'}{\partial x} + \frac{\partial u' v'}{\partial y} + \frac{\partial u' w'}{\partial z} \\ + f \left( \hat{\Omega}_{\alpha 2}(\langle w \rangle + w') - \hat{\Omega}_{\alpha 3}(\langle v \rangle + v') \right) = -\frac{1}{\rho_0} \frac{\partial \langle P \rangle}{\partial x} - 1 \frac{1}{\rho_0} \frac{\partial P'}{\partial x}. \end{aligned} \quad (2.32)$$

When Equation 2.32 is ensemble-averaged, and making use of  $\langle \langle \cdot \rangle \rangle = \langle \cdot \rangle$ , the 3rd, 4th and 5th terms are found to equal zero due to the fluctuating terms in them. Thus,

$$\begin{aligned} \frac{\partial \langle u \rangle}{\partial t} + \left[ \langle u \rangle \frac{\partial}{\partial x} + \langle v \rangle \frac{\partial}{\partial y} + \langle w \rangle \frac{\partial}{\partial z} \right] \langle u \rangle \\ + f \left( \hat{\Omega}_{\alpha 2} \langle w \rangle - \hat{\Omega}_{\alpha 3} \langle v \rangle \right) \\ = -\frac{1}{\rho_0} \frac{\partial \langle P \rangle}{\partial x} - \left\{ \frac{\partial \langle u' u' \rangle}{\partial x} + \frac{\partial \langle u' v' \rangle}{\partial y} + \frac{\partial \langle u' w' \rangle}{\partial z} \right\}. \end{aligned} \quad (2.33)$$

The Reynolds stress tensor is defined as,

$$\tau_{xx} = -\rho_0 \langle u'u' \rangle, \tau_{xy} = -\rho_0 \langle u'v' \rangle, \tau_{xz} = -\rho_0 \langle u'w' \rangle,$$

$$\tau_{yx} = -\rho_0 \langle v'u' \rangle, \tau_{yy} = -\rho_0 \langle v'v' \rangle, \tau_{yz} = -\rho_0 \langle v'w' \rangle, \text{ and}$$

$$\tau_{zx} = -\rho_0 \langle w'u' \rangle, \tau_{zy} = -\rho_0 \langle w'v' \rangle, \tau_{zz} = -\rho_0 \langle w'w' \rangle.$$

Using the  $x$  component stress tensors, substituting into Equation 2.33, and dropping the brace notation, gives the 1st component of the momentum equation in the  $x$  axis direction to be:

$$\frac{Du}{Dt} + f \left( \hat{\Omega}_{\alpha 2} w - \hat{\Omega}_{\alpha 3} v \right) = -\frac{1}{\rho_0} \frac{\partial P}{\partial x} + \frac{1}{\rho_0} \left( \frac{\partial \tau_{xx}}{\partial x} + \frac{\partial \tau_{xy}}{\partial y} + \frac{\partial \tau_{xz}}{\partial z} \right). \quad (2.34)$$

The 2nd and 3rd components of the momentum equation (Equation 2.24) in the  $y$  and  $z$  directions respectively are given by:

$$\frac{Dv}{Dt} + f \left( \hat{\Omega}_{\alpha 3} u - \hat{\Omega}_{\alpha 1} w \right) = -\frac{1}{\rho_0} \frac{\partial P}{\partial y} + \frac{\Delta \rho}{\rho_0} g_{\alpha 2} + \frac{1}{\rho_0} \left( \frac{\partial \tau_{yx}}{\partial x} + \frac{\partial \tau_{yy}}{\partial y} + \frac{\partial \tau_{yz}}{\partial z} \right), \quad (2.35)$$

and

$$\frac{Dw}{Dt} + f \left( \hat{\Omega}_{\alpha 1} v - \hat{\Omega}_{\alpha 2} u \right) = -\frac{1}{\rho_0} \frac{\partial P}{\partial z} + \frac{\Delta \rho}{\rho_0} g_{\alpha 3} + \frac{1}{\rho_0} \left( \frac{\partial \tau_{zx}}{\partial x} + \frac{\partial \tau_{zy}}{\partial y} + \frac{\partial \tau_{zz}}{\partial z} \right), \quad (2.36)$$

noting the additional terms associated with the gravitational acceleration in the  $y$  and  $z$  directions, due to Equation 2.20.

The expression for  $P$  in the SC system is given by:

$$P = p + \int^{y \sin \alpha + z \cos \alpha} \rho_e(\zeta) g \, d\zeta + \frac{\rho_0}{2} [(\boldsymbol{\Omega} \cdot \mathbf{x})^2 - |\boldsymbol{\Omega}|^2 |\mathbf{x}|^2], \quad (2.37)$$

where  $x = (x, y, z)$  are in the SC system.

#### 2.4.4 Transformation into path-relative coordinates

After being rotated about the  $x$ -axis by angle  $\alpha$  to find the equations in the SC system, the equations are then transformed into the PC system (taking  $X(\xi, t)$  and  $Y(\xi, t)$  as the  $(x, y)$  coordinates for the centre line of the current), where:

$$x = X(\xi, t) - \eta \sin(\beta(\xi, t)), \quad (2.38)$$

and

$$y = Y(\xi, t) + \eta \cos(\beta(\xi, t)), \quad (2.39)$$

using the rotational matrix,  $\mathbf{R}_p$ , such that:

$$\mathbf{R}_p = \begin{pmatrix} \cos \beta & \sin \beta & 0 \\ -\sin \beta & \cos \beta & 0 \\ 0 & 0 & 1 \end{pmatrix}, \quad (2.40)$$

where  $z$  and  $t$  remain unchanged compared to the SC system.

The velocity field  $\boldsymbol{\mu} = (\mu, \eta, w)$  is therefore given by:

$$\boldsymbol{\mu} = \begin{pmatrix} \mu \\ \eta \\ w \end{pmatrix} = \mathbf{R}_p \mathbf{u} = \begin{pmatrix} \cos \beta & \sin \beta & 0 \\ -\sin \beta & \cos \beta & 0 \\ 0 & 0 & 1 \end{pmatrix} \begin{pmatrix} u \\ v \\ w \end{pmatrix} = \begin{pmatrix} u \cos \beta + v \sin \beta \\ -u \sin \beta + v \cos \beta \\ w \end{pmatrix}, \quad (2.41)$$

and

$$u = \mu \cos(\beta) - \nu \sin(\beta), \quad (2.42)$$

$$v = \mu \sin(\beta) + \nu \cos(\beta), \quad (2.43)$$

where:  $\mathbf{R}_p = \mathbf{R}_p(\beta) = \mathbf{R}_p(\xi, t)$ .

The PC system has the following axes:  $\xi$  is the streamwise coordinate along the current, and  $\eta$  is the spanwise coordinate and is locally perpendicular to  $\xi$ . Noting that the local angle between the path and the  $x$ -axis in the SC system is chosen to be  $\beta(\xi, t)$ , such that:

$$\left. \frac{\partial X}{\partial \xi} \right|_t = \cos \beta, \quad \left. \frac{\partial Y}{\partial \xi} \right|_t = \sin \beta. \quad (2.44)$$

To find the partial derivatives  $\frac{\partial}{\partial x}, \frac{\partial}{\partial y}, \frac{\partial}{\partial z}, \frac{\partial}{\partial t}$  in terms of the PC system, the Jacobian matrix

$\mathbf{J}$  is introduced:

$$\mathbf{J} = \begin{pmatrix} x_\xi & y_\xi & z_\xi & t_\xi \\ x_\eta & y_\eta & z_\eta & t_\eta \\ x_z & y_z & z_z & t_z \\ x_t & y_t & z_t & t_t \end{pmatrix} = \begin{pmatrix} X_\xi - \eta\beta_\xi \cos \beta & Y_\xi - \eta\beta_\xi \sin \beta & 0 & 0 \\ -\sin \beta & \cos \beta & 0 & 0 \\ 0 & 0 & 1 & 0 \\ X_t - \eta\beta_t \cos \beta & Y_t - \eta\beta_t \sin \beta & 0 & 1 \end{pmatrix}. \quad (2.45)$$

Making the following substitutions:  $X_\xi = \cos \beta$ ,  $Y_\xi = \sin \beta$  and defining  $h = 1 - \eta\beta_\xi$ ,  $\mathbf{J}$  can be written as:

$$\mathbf{J} = \begin{pmatrix} h \cos \beta & h \sin \beta & 0 & 0 \\ -\sin \beta & \cos \beta & 0 & 0 \\ 0 & 0 & 1 & 0 \\ X_t - \eta\beta_t \cos \beta & Y_t - \eta\beta_t \sin \beta & 0 & 1 \end{pmatrix}. \quad (2.46)$$

Hence, the inverse matrix  $\mathbf{J}^{-1}$  is given as:

$$\begin{aligned}
\mathbf{J}^{-1} &= \begin{pmatrix} \xi_x & \eta_x & z_x & t_x \\ \xi_y & \eta_y & z_y & t_y \\ \xi_z & \eta_z & z_z & t_z \\ \xi_t & \eta_t & z_t & t_t \end{pmatrix} \\
&= \begin{pmatrix} \frac{1}{h} \cos \beta & -\sin \beta & 0 & 0 \\ \frac{1}{h} \sin \beta & \cos \beta & 0 & 0 \\ 0 & 0 & 1 & 0 \\ \frac{1}{h}[\eta\beta_t - (X_t \cos \beta + Y_t \sin \beta)] & (X_t \sin \beta - Y_t \cos \beta) & 0 & 1 \end{pmatrix} \quad (2.47) \\
&= \begin{pmatrix} \frac{1}{h} \cos \beta & -\sin \beta & 0 & 0 \\ \frac{1}{h} \sin \beta & \cos \beta & 0 & 0 \\ 0 & 0 & 1 & 0 \\ \frac{1}{h}[\eta\beta_t - \mu_0] & -\nu_0 & 0 & 1 \end{pmatrix},
\end{aligned}$$

where the following definitions were made:  $\mu_0(\xi, t) = X_t \cos \beta + Y_t \sin \beta$ , and  $\nu_0(\xi, t) = Y_t \sin \beta - X_t \cos \beta$ . Therefore, using the chain rule:

$$\left. \frac{\partial}{\partial x} \right|_{y,z,t} = \frac{1}{h} \cos \beta \left. \frac{\partial}{\partial \xi} \right|_{\eta,z,t} - \sin \beta \left. \frac{\partial}{\partial \eta} \right|_{\xi,z,t}, \quad (2.48)$$

$$\left. \frac{\partial}{\partial y} \right|_{x,z,t} = \frac{1}{h} \sin \beta \left. \frac{\partial}{\partial \xi} \right|_{\eta,z,t} + \cos \beta \left. \frac{\partial}{\partial \eta} \right|_{\xi,z,t}, \quad (2.49)$$

$$\left. \frac{\partial}{\partial z} \right|_{x,y,t} = \left. \frac{\partial}{\partial z} \right|_{\xi,\eta,t}, \quad (2.50)$$

$$\left. \frac{\partial}{\partial t} \right|_{x,y,z} = \left. \frac{\partial}{\partial t} \right|_{\xi,\eta,z} + \frac{1}{h}(\eta\beta_t - \mu_0) \left. \frac{\partial}{\partial \xi} \right|_{\eta,z,t} - \nu_0 \left. \frac{\partial}{\partial \eta} \right|_{\xi,z,t}. \quad (2.51)$$

Using Equation 2.48, Equation 2.49, and Equation 2.50, and writing partial derivatives

as subscripts (e.g.  $\frac{\partial \beta}{\partial \xi} = \beta_\xi$ ), the divergence of the velocity field  $\mathbf{u}$  in the PC system is:

$$\begin{aligned}\nabla \cdot \mathbf{u} &= \left. \frac{\partial u}{\partial x} \right|_{y,z,t} + \left. \frac{\partial v}{\partial y} \right|_{x,z,t} + \left. \frac{\partial w}{\partial z} \right|_{x,y,t} \\ &= \left\{ \frac{1}{h} \cos \beta \left. \frac{\partial u}{\partial \xi} \right|_{\eta,z,t} - \sin \beta \left. \frac{\partial u}{\partial \eta} \right|_{\xi,z,t} \right\} \\ &\quad + \left\{ \frac{1}{h} \sin \beta \left. \frac{\partial v}{\partial \xi} \right|_{\eta,z,t} + \cos \beta \left. \frac{\partial v}{\partial \eta} \right|_{\xi,z,t} \right\} + \left. \frac{\partial w}{\partial z} \right|_{\xi,\eta,t}.\end{aligned}\tag{2.52}$$

By making use of Equation 2.42 and Equation 2.43, while noting that  $\beta_\eta = 0$ , gives:

$$\begin{aligned}\nabla \cdot \mathbf{u} &= \frac{1}{h} \frac{\partial}{\partial \xi} [u \cos \beta + v \sin \beta] - \frac{\beta_\xi}{h} [-u \sin \beta + v \cos \beta] \\ &\quad + \frac{\partial}{\partial \eta} [-u \sin \beta + v \cos \beta] + \frac{\partial w}{\partial z} \\ &= \frac{1}{h} \frac{\partial \mu}{\partial \xi} - \frac{\beta_\xi \nu}{h} + \frac{\partial \nu}{\partial \eta} + \frac{\partial w}{\partial z}.\end{aligned}\tag{2.53}$$

Substituting in  $\mu$  and  $\nu$  from Equation 2.40, the divergence of the velocity field  $\mathbf{u}$  in the PC system can be written as:

$$\nabla \cdot \mathbf{u} = h^{-1}(\mu_\xi - \beta_\xi \nu) + \nu_\eta + w_z.\tag{2.54}$$

Interpreting the definitions of  $\mu_0$  and  $\nu_0$  given above, the position of the path in the SC system is given by  $(X(\xi, t), Y(\xi, t))$ . So, the velocity of the point of the path parametrised by  $\xi$  is given by:

$$u_0(\xi, t) = \left. \frac{\partial X}{\partial t} \right|_\xi, \quad v_0(\xi, t) = \left. \frac{\partial Y}{\partial t} \right|_\xi.\tag{2.55}$$

Hence, in the PC path itself has a local velocity in the streamwise and spanwise directions and given by:

$$\begin{pmatrix} \mu_0 \\ \nu_0 \end{pmatrix} = \begin{pmatrix} \cos \beta & \sin \beta \\ -\sin \beta & \cos \beta \end{pmatrix} \begin{pmatrix} u_0 \\ v_0 \end{pmatrix} = \begin{pmatrix} X_t \cos \beta + Y_t \sin \beta \\ -X_t \sin \beta + Y_t \cos \beta \end{pmatrix}. \quad (2.56)$$

Next, the momentum equation, whose components are given in Equations (2.34) to (2.36), is transformed into the PC system. This is done a term at a time.

Taking the convective derivative  $\frac{D\mathbf{u}}{Dt}$  first, where:

$$\frac{D\mathbf{u}}{Dt} = \frac{\partial \mathbf{u}}{\partial t} + u \frac{\partial \mathbf{u}}{\partial x} + v \frac{\partial \mathbf{u}}{\partial y} + w \frac{\partial \mathbf{u}}{\partial z}, \quad (2.57)$$

and transforming  $\frac{\partial \mathbf{u}}{\partial t}$  into the PC, by using  $\mathbf{R}_p$ , gives:

$$\begin{aligned} \mathbf{R}_p \frac{\partial \mathbf{u}}{\partial t} \Big|_{x,y,z} &= \mathbf{R}_p \frac{\partial}{\partial t} \Big|_{x,y,z} (\mathbf{R}_p^{-1} \boldsymbol{\mu}) = \mathbf{R}_p \mathbf{R}_p^{-1} \frac{\partial \boldsymbol{\mu}}{\partial t} \Big|_{x,y,z} + \mathbf{R}_p \frac{\partial \mathbf{R}_p^{-1}}{\partial t} \Big|_{x,y,z} \boldsymbol{\mu} \\ &= \frac{\partial \boldsymbol{\mu}}{\partial t} \Big|_{x,y,z} + \frac{\partial \beta}{\partial t} \Big|_{x,y,z} \begin{pmatrix} 0 & -1 & 0 \\ 1 & 0 & 0 \\ 0 & 0 & 0 \end{pmatrix} \boldsymbol{\mu} \\ &= \frac{\partial \boldsymbol{\mu}}{\partial t} \Big|_{\xi,\eta,z} + \frac{1}{h} (\eta \beta_t - \mu_0) \frac{\partial \boldsymbol{\mu}}{\partial t} \Big|_{\eta,z,t} - \nu_0 \frac{\partial \boldsymbol{\mu}}{\partial t} \Big|_{\xi,z,t} \\ &+ \left\{ \beta_t + \frac{\beta_\xi}{h} (\eta \beta_t - \mu_0) \right\} \begin{pmatrix} 0 & -1 & 0 \\ 1 & 0 & 0 \\ 0 & 0 & 0 \end{pmatrix} \boldsymbol{\mu}. \end{aligned} \quad (2.58)$$

The rest of the convective derivative in Equation 2.57 is now considered:

$$\begin{aligned}
\mathbf{u} \cdot \nabla &= u \frac{\partial}{\partial x} \Big|_{y,z,t} + v \frac{\partial}{\partial y} \Big|_{x,z,t} + w \frac{\partial}{\partial z} \Big|_{x,y,t} \\
&= u \left\{ \frac{1}{h} \cos \beta \frac{\partial}{\partial \xi} \Big|_{\eta,z,t} - \sin \beta \frac{\partial}{\partial \eta} \Big|_{\xi,z,t} \right\} \\
&+ v \left\{ \frac{1}{h} \sin \beta \frac{\partial}{\partial \xi} \Big|_{\eta,z,t} + \cos \beta \frac{\partial}{\partial \eta} \Big|_{\xi,z,t} \right\} + w \frac{\partial}{\partial z} \Big|_{\xi,\eta,t} \\
&= \frac{1}{h} [u \cos \beta + v \sin \beta] \frac{\partial}{\partial \xi} \Big|_{\eta,z,t} + [-u \sin \beta + v \cos \beta] \frac{\partial}{\partial \eta} \Big|_{\xi,z,t} \\
&+ w \frac{\partial}{\partial z} \Big|_{\xi,z,t} = \frac{\mu}{h} \frac{\partial}{\partial \xi} + \nu \frac{\partial}{\partial \eta} + w \frac{\partial}{\partial z},
\end{aligned} \tag{2.59}$$

leading to the definition:  $\hat{\nabla} = (h^{-1} \partial_\xi, \partial_\eta, \partial_z)$  in PC, such that  $\mathbf{u} \cdot \nabla = \boldsymbol{\mu} \cdot \hat{\nabla}$ . Then:

$$\begin{aligned}
\mathbf{R}_p(\mathbf{u} \cdot \nabla) \mathbf{u} &= \mathbf{R}_p \left[ (\boldsymbol{\mu} \cdot \hat{\nabla})(\mathbf{R}_p^{-1} \boldsymbol{\mu}) \right] \\
&= (\boldsymbol{\mu} \cdot \hat{\nabla})(\mathbf{R}_p \mathbf{R}_p^{-1} \boldsymbol{\mu}) - \left[ (\boldsymbol{\mu} \cdot \hat{\nabla}) \mathbf{R}_p \right] (\mathbf{R}_p^{-1} \boldsymbol{\mu}) \\
&= (\boldsymbol{\mu} \cdot \hat{\nabla}) \boldsymbol{\mu} - \left[ (\boldsymbol{\mu} \cdot \hat{\nabla}) \mathbf{R}_p \right] (\mathbf{R}_p^{-1} \boldsymbol{\mu}).
\end{aligned} \tag{2.60}$$

Noting that,  $\mathbf{R}_p = \mathbf{R}_p(\beta) = \mathbf{R}_p(\xi, t)$ , therefore  $\partial_\eta \mathbf{R}_p = \partial_z \mathbf{R}_p = 0$ , so  $(\boldsymbol{\mu} \cdot \hat{\nabla}) \mathbf{R}_p = \mu h^{-1} \partial_\xi \mathbf{R}_p$ , and using  $\mathbf{R}_p$  from Equation 2.40, giving  $\mathbf{R}_p^{-1}$  to be:

$$\mathbf{R}_p^{-1} = \begin{pmatrix} \cos \beta & -\sin \beta & 0 \\ \sin \beta & \cos \beta & 0 \\ 0 & 0 & 1 \end{pmatrix}. \tag{2.61}$$

Then,

$$\begin{aligned}
\left[ (\boldsymbol{\mu} \cdot \hat{\nabla}) \mathbf{R}_p \right] \mathbf{R}_p^{-1} &= \frac{\mu \beta_\xi}{h} \begin{pmatrix} -\sin \beta & \cos \beta & 0 \\ -\cos \beta & -\sin \beta & 0 \\ 0 & 0 & 1 \end{pmatrix} \begin{pmatrix} \cos \beta & -\sin \beta & 0 \\ \sin \beta & \cos \beta & 0 \\ 0 & 0 & 1 \end{pmatrix} \\
&= -\frac{\mu \beta_\xi}{h} \begin{pmatrix} 0 & -1 & 0 \\ 1 & 0 & 0 \\ 0 & 0 & 0 \end{pmatrix}.
\end{aligned} \tag{2.62}$$

Substituting into Equation 2.60 gives:

$$\mathbf{R}_p (\mathbf{u} \cdot \nabla) \mathbf{u} = (\boldsymbol{\mu} \cdot \hat{\nabla}) \boldsymbol{\mu} + \frac{\mu \beta_\xi}{h} \begin{pmatrix} 0 & -1 & 0 \\ 1 & 0 & 0 \\ 0 & 0 & 0 \end{pmatrix} \boldsymbol{\mu}. \tag{2.63}$$

Combining Equations (2.58) and (2.63) gives the rotated convective derivative in PC as:

$$\begin{aligned}
\mathbf{R}_p \frac{D\boldsymbol{\mu}}{Dt} &= \frac{\partial \boldsymbol{\mu}}{\partial t} + (\boldsymbol{\mu} \cdot \hat{\nabla}) \boldsymbol{\mu} + \frac{1}{h} (\eta \beta_t - \mu_0) \frac{\partial \boldsymbol{\mu}}{\partial \xi} - \nu_0 \frac{\partial \boldsymbol{\mu}}{\partial \eta} \\
&+ \left[ \beta_t + \frac{\beta_\xi}{h} (\eta \beta_t - \mu_0 + \mu) \right] \begin{pmatrix} 0 & -1 & 0 \\ 1 & 0 & 0 \\ 0 & 0 & 0 \end{pmatrix} \boldsymbol{\mu}.
\end{aligned} \tag{2.64}$$

Next, the Coriolis term of the momentum equation  $f\boldsymbol{\Omega}_\alpha$ , given in the component format

in Equations (2.34), (2.35) and (2.45) in the SC system, written here as:

$$f \begin{pmatrix} \hat{\Omega}_{\alpha 2} w - \hat{\Omega}_{\alpha 3} v \\ \hat{\Omega}_{\alpha 3} u - \hat{\Omega}_{\alpha 1} w \\ \hat{\Omega}_{\alpha 1} v - \hat{\Omega}_{\alpha 2} u \end{pmatrix} = f \begin{pmatrix} 0 & -\hat{\Omega}_{\alpha 3} & \hat{\Omega}_{\alpha 2} \\ \hat{\Omega}_{\alpha 3} & 0 & -\hat{\Omega}_{\alpha 1} \\ -\hat{\Omega}_{\alpha 2} & \hat{\Omega}_{\alpha 1} & 0 \end{pmatrix} \mathbf{u}, \quad (2.65)$$

is rotated into the PC system, such that:

$$\begin{aligned} \mathbf{R}_p f \begin{pmatrix} \hat{\Omega}_{\alpha 2} w - \hat{\Omega}_{\alpha 3} v \\ \hat{\Omega}_{\alpha 3} u - \hat{\Omega}_{\alpha 1} w \\ \hat{\Omega}_{\alpha 1} v - \hat{\Omega}_{\alpha 2} u \end{pmatrix} &= f \mathbf{R}_p \begin{pmatrix} 0 & -\hat{\Omega}_{\alpha 3} & \hat{\Omega}_{\alpha 2} \\ \hat{\Omega}_{\alpha 3} & 0 & -\hat{\Omega}_{\alpha 1} \\ -\hat{\Omega}_{\alpha 2} & \hat{\Omega}_{\alpha 1} & 0 \end{pmatrix} \mathbf{R}_p^{-1} \boldsymbol{\mu} \\ &= f \begin{pmatrix} 0 & -\hat{\Omega}_{\alpha 3} & \hat{\Omega}_{\alpha 2} \cos \beta - \hat{\Omega}_{\alpha 1} \sin \beta \\ \hat{\Omega}_{\alpha 3} & 0 & -\hat{\Omega}_{\alpha 1} \cos \beta - \hat{\Omega}_{\alpha 2} \sin \beta \\ -\hat{\Omega}_{\alpha 2} \cos \beta + \hat{\Omega}_{\alpha 1} \sin \beta & \hat{\Omega}_{\alpha 1} \cos \beta + \hat{\Omega}_{\alpha 2} \sin \beta & 0 \end{pmatrix} \boldsymbol{\mu} \quad (2.66) \\ &= f \begin{pmatrix} -\hat{\Omega}_{\alpha 3} \nu + [\hat{\Omega}_{\alpha 2} \cos \beta - \hat{\Omega}_{\alpha 1} \sin \beta] w \\ \hat{\Omega}_{\alpha 3} \mu - [\hat{\Omega}_{\alpha 1} \cos \beta + \hat{\Omega}_{\alpha 2} \sin \beta] w \\ [-\hat{\Omega}_{\alpha 2} \cos \beta + \hat{\Omega}_{\alpha 1} \sin \beta] \mu + \hat{\Omega}_{\alpha 1} \cos \beta + \hat{\Omega}_{\alpha 2} \sin \beta \nu \end{pmatrix}. \end{aligned}$$

Next, the pressure gradient term  $\frac{1}{\rho_0} \nabla P$ , is rotated from the SC system to the PC system.

Rotating the gradient operator first gives:

$$\begin{aligned}
\mathbf{R}_p \nabla_{CS} &= \begin{pmatrix} \cos \beta & \sin \beta & 0 \\ -\sin \beta & \cos \beta & 0 \\ 0 & 0 & 1 \end{pmatrix} \begin{pmatrix} \partial_x \\ \partial_y \\ \partial_z \end{pmatrix} \\
&= \begin{pmatrix} \cos \beta \partial_x + \sin \beta \partial_y \\ -\sin \beta \partial_x + \cos \beta \partial_y \\ \partial_z \end{pmatrix} \\
&= \begin{pmatrix} \cos \beta \left[ \frac{1}{h} \cos \beta \partial_\xi - \sin \beta \partial_\eta \right] + \sin \beta \left[ \frac{1}{h} \sin \beta \partial_\xi + \cos \beta \partial_\eta \right] \\ -\sin \beta \left[ \frac{1}{h} \cos \beta \partial_\xi - \sin \beta \partial_\eta \right] + \cos \beta \left[ \frac{1}{h} \sin \beta \partial_\xi + \cos \beta \partial_\eta \right] \\ \partial_z \end{pmatrix} = \hat{\nabla},
\end{aligned} \tag{2.67}$$

*PC*

where  $\hat{\nabla}$  is defined previously as  $\hat{\nabla} = (h^{-1}\partial_\xi, \partial_\eta, \partial_z)$ . So the pressure gradient term is given by  $\frac{1}{\rho_0} \hat{\nabla} P$  in the PC system.

The  $\rho_0^{-1}\Delta\rho\mathbf{g}_\alpha$  term is rotated into the PC system as:

$$\begin{aligned}
\mathbf{R}_p \frac{\Delta\rho}{\rho_0} \mathbf{g}_\alpha &= \frac{\Delta\rho}{\rho_0} \begin{pmatrix} \cos \beta & \sin \beta & 0 \\ -\sin \beta & \cos \beta & 0 \\ 0 & 0 & 1 \end{pmatrix} \begin{pmatrix} 0 \\ g_{\alpha 2} \\ g_{\alpha 3} \end{pmatrix} \\
&= \frac{\Delta\rho}{\rho_0} \begin{pmatrix} g_{\alpha 2} \sin \beta \\ g_{\alpha 2} \cos \beta \\ g_{\alpha 3} \end{pmatrix} \\
&= -\frac{g\Delta\rho}{\rho_0} \begin{pmatrix} \sin \alpha \sin \beta \\ \sin \alpha \cos \beta \\ \cos \alpha \end{pmatrix}.
\end{aligned} \tag{2.68}$$

The remaining terms to be dealt with are the Reynolds stresses, and dealing with them can be done using two approaches. The first will be to define a suitable stress tensor in the PC system by re-writing the existing Reynolds stresses in terms of the PC system. The second approach will be to substitute in an eddy viscosity model and examine the consequences by using a turbulence closure.

### Approach 1:

Having the stress tensor as:

$$\underline{\underline{\tau}}_1 = \begin{pmatrix} \tau_{xx} & \tau_{xy} & \tau_{xz} \\ \tau_{yx} & \tau_{yy} & \tau_{yz} \\ \tau_{zx} & \tau_{zy} & \tau_{zz} \end{pmatrix},$$

and defining,  $\underline{\underline{\sigma}} = \mathbf{R}_p \underline{\underline{\tau}}_1 \mathbf{R}_p^{-1}$ , the Reynolds stresses can be transformed from the SC

system to the PC system as:

$$\mathbf{R}_p \nabla \cdot \underline{\underline{\tau}} = \begin{pmatrix} \frac{1}{h} + \frac{\partial \sigma_{\xi\xi}}{\partial \xi} + \frac{\partial \sigma_{\xi\eta}}{\partial \eta} + \frac{\partial \sigma_{\xi z}}{\partial z} - \frac{\beta_\xi}{h} (\sigma_{\xi\eta} + \sigma_{\eta\xi}) \\ \frac{1}{h} + \frac{\partial \sigma_{\eta\xi}}{\partial \xi} + \frac{\partial \sigma_{\eta\eta}}{\partial \eta} + \frac{\partial \sigma_{\eta z}}{\partial z} - \frac{\beta_\xi}{h} (\sigma_{\xi\xi} - \sigma_{\eta\eta}) \\ \frac{1}{h} + \frac{\partial \sigma_{z\xi}}{\partial \xi} + \frac{\partial \sigma_{z\eta}}{\partial \eta} + \frac{\partial \sigma_{zz}}{\partial z} - \frac{\beta_\xi}{h} \sigma_{z\eta} \end{pmatrix}. \quad (2.69)$$

Thus, to summaries, the incompressibility condition in the PC system is given by:

$$\frac{1}{h} \left( \frac{\partial \mu}{\partial \xi} - \nu \frac{\partial \beta}{\partial \xi} \right) + \frac{\partial \nu}{\partial \eta} + \frac{\partial w}{\partial z} = 0, \quad (2.70)$$

and the momentum equation in components format in the PC system in the streamwise, spanwise and slope-normal directions respectively, is given by:

$$\begin{aligned} & \frac{\partial \mu}{\partial t} + \frac{\mu}{h} \frac{\partial \mu}{\partial \xi} + \nu \frac{\partial \mu}{\partial \eta} + w \frac{\partial \mu}{\partial z} + \frac{\eta \beta_t - \mu_0}{h} \frac{\partial \mu}{\partial \xi} - \nu_0 \frac{\partial \mu}{\partial \eta} \\ & - \left[ \beta_t + \frac{\beta_\xi}{h} (\eta \beta_t - \mu_0 + \mu) \right] \nu + f \left[ -\hat{\Omega}_{\alpha 3} \nu + (\hat{\Omega}_{\alpha 2} \cos \beta - \hat{\Omega}_{\alpha 1} \sin \beta) w \right] \\ & = -\frac{1}{\rho_0 h} \frac{\partial P}{\partial \xi} + \frac{g \sin \alpha \Delta \rho}{\rho_0} \sin \beta + \frac{1}{\rho_0} \left[ \frac{1}{h} \frac{\partial \sigma_{\xi\xi}}{\partial \xi} + \frac{\partial \sigma_{\xi\eta}}{\partial \eta} + \frac{\partial \sigma_{\xi z}}{\partial z} - \frac{\beta_\xi}{h} (\sigma_{\xi\eta} + \sigma_{\eta\xi}) \right], \end{aligned} \quad (2.71)$$

$$\begin{aligned} & \frac{\partial \nu}{\partial t} + \frac{\mu}{h} \frac{\partial \nu}{\partial \xi} + \nu \frac{\partial \nu}{\partial \eta} + w \frac{\partial \nu}{\partial z} + \frac{\eta \beta_t - \mu_0}{h} \frac{\partial \nu}{\partial \xi} - \nu_0 \frac{\partial \nu}{\partial \eta} \\ & + \left[ \beta_t + \frac{\beta_\xi}{h} (\eta \beta_t - \mu_0 + \mu) \right] \mu + f \left[ \hat{\Omega}_{\alpha 3} \mu - (\hat{\Omega}_{\alpha 1} \cos \beta + \hat{\Omega}_{\alpha 2} \sin \beta) w \right] \\ & = -\frac{1}{\rho_0} \frac{\partial P}{\partial \eta} + \frac{g \sin \alpha \Delta \rho}{\rho_0} \cos \beta + \frac{1}{\rho_0} \left[ \frac{1}{h} \frac{\partial \sigma_{\eta\xi}}{\partial \xi} + \frac{\partial \sigma_{\eta\eta}}{\partial \eta} + \frac{\partial \sigma_{\eta z}}{\partial z} - \frac{\beta_\xi}{h} (\sigma_{\xi\xi} - \sigma_{\eta\eta}) \right], \end{aligned} \quad (2.72)$$

and

$$\begin{aligned}
& \frac{\partial w}{\partial t} + \frac{\mu}{h} \frac{\partial w}{\partial \xi} + \nu \frac{\partial w}{\partial \eta} + w \frac{\partial w}{\partial z} + \frac{\eta \beta_t - \mu_0}{h} \frac{\partial w}{\partial \xi} - \nu_0 \frac{\partial w}{\partial \eta} \\
& + f \left[ (-\hat{\Omega}_{\alpha 2} \cos \beta + \hat{\Omega}_{\alpha 1} \sin \beta) \mu + (\hat{\Omega}_{\alpha 1} \cos \beta + \hat{\Omega}_{\alpha 2} \sin \beta) \nu \right] \\
& = -\frac{1}{\rho_0} \frac{\partial P}{\partial z} + \frac{g \cos \alpha \Delta \rho}{\rho_0} + \frac{1}{\rho_0} \left[ \frac{1}{h} \frac{\partial \sigma_{z\xi}}{\partial \xi} + \frac{\partial \sigma_{z\eta}}{\partial \eta} + \frac{\partial \sigma_{zz}}{\partial z} - \frac{\beta_\xi}{h} \sigma_{z\eta} \right].
\end{aligned} \tag{2.73}$$

### Approach 2:

An eddy viscosity model is defined, such that the Reynolds stresses are defined by:

$$\underline{\underline{\tau_2}} = \begin{pmatrix} 2A_H u_x & A_H(v_x + u_y) & A_V u_z + A_H w_x \\ A_H(v_x + u_y) & 2A_H v_x & A_V v_z + A_H w_y \\ A_V u_z + A_H w_x & A_V v_z + A_H w_y & 2A_V w_z \end{pmatrix}, \tag{2.74}$$

for a horizontal eddy viscosity,  $A_H$  and a vertical eddy viscosity  $A_V$ .

Then, the Reynolds stresses in the PC system are given by:

$$\underline{\underline{\sigma}} = \rho_0 \begin{bmatrix} \frac{2}{h} A_H(\mu_\xi - \nu \beta_\xi) & A_H(\mu_\eta + \frac{1}{h}[\nu_\xi + \mu \beta_\xi]) & A_V \mu_z + A_H \frac{1}{h} w_\xi \\ A_H(\mu_\eta + \frac{1}{h}[\nu_\xi + \mu \beta_\xi]) & 2A_H \nu_\eta & A_V v_z + A_H w_y \\ A_V \mu_z + A_H \frac{1}{h} w_\xi & A_V v_z + A_H w_y & 2A_V w_z \end{bmatrix}, \tag{2.75}$$

where the same  $A_H$  and  $A_V$  appear in each expression. This facilitates a more rigorous non-dimensionalisation in terms of the Reynolds stresses in the PC system.

### 2.4.5 Non-dimensionalisation of the equations

A length scale  $L$  and a velocity scale  $U$  are introduced in each of the streamwise, spanwise, and plane normal directions, such that:

$$\begin{aligned}\xi &= L_\xi \xi', \quad \eta = L_\eta \eta', \quad z = L_z z', \\ \mu &= U_\xi \mu', \quad \nu = U_\eta \nu', \quad w = U_z w' .\end{aligned}\tag{2.76}$$

A pressure scale  $\Gamma$  and a time-scale  $T$  are also introduced, such that:

$$P = \Gamma P', \quad t = T t',\tag{2.77}$$

where dashed quantities are non-dimensional, and assumed to be of order one.

Non-dimensionalisation of the continuity equation, (Equation 2.70):

$$\frac{1}{1 - \frac{L_n \eta' \beta'_\xi}{L_\xi}} \left( \frac{U_\xi}{L_\xi} \frac{\partial \mu'}{\partial \xi'} - \frac{U_\eta \nu'}{L_\xi} \frac{\partial \beta}{\partial \xi'} \right) + \frac{U_\eta}{L_\eta} \frac{\partial \nu'}{\partial \eta'} + \frac{U_z}{L_z} \frac{\partial w'}{\partial z'} = 0.\tag{2.78}$$

Smith [1975] observes that  $h \approx 1$  in these flows, which is true provided  $L_\eta \ll L_\xi$ , giving:

$$\frac{L_\eta}{L_\xi} = \delta,\tag{2.79}$$

where  $\delta \ll 1$ , which implies that the current is much narrower in the spanwise direction than it is long in the streamwise direction; an assumption that agrees with physical observations.

Hence,

$$(1 + O(\delta)) \left( \frac{U_\xi}{L_\xi} \frac{\partial \mu'}{\partial \xi'} - \frac{U_\eta}{L_\xi} \nu' \frac{\partial \beta}{\partial \xi'} \right) + \frac{U_\eta}{L_\eta} \frac{\partial \nu'}{\partial \eta'} + \frac{U_z}{L_z} \frac{\partial w'}{\partial z'} = 0 \Rightarrow \frac{U_\xi}{L_\xi} \sim \frac{U_\eta}{L_\eta} \sim \frac{U_z}{L_z}. \quad (2.80)$$

Smith [1975] makes the assumption that  $w \ll \mu$ , which gives:  $U_z = \epsilon U_\xi$ , (where  $\epsilon \ll 1$ ), and this forces  $L_z = \epsilon L_\xi$ . No assumption has yet been made about the relative magnitudes of  $\delta$  and  $\epsilon$ , .

Summarising the above:

$$L_\eta = \delta L_\xi, \quad L_z = \epsilon L_\xi, \quad U_\eta = \delta U_\xi, \quad U_z = \epsilon U_\xi. \quad (2.81)$$

The stress tensor,  $\underline{\underline{\sigma}}$  given in Equation 2.75, and taking advantage of the symmetry and defining  $A_H = U_\xi L_z A'_H$ ,  $A_V = U_\xi L_z A'_V$ , where  $A'_H$  and  $A'_V$  are of order 1:

$$\begin{aligned} \underline{\underline{\sigma}} &= \rho_0 \begin{bmatrix} \frac{2}{h} A_H (\mu_\xi - \nu \beta_\xi) & A_H (\mu_\eta + \frac{1}{h} [\nu_\xi + \mu \beta_\xi]) & A_V \mu_z + A_H \frac{1}{h} w_\xi \\ A_H (\mu_\eta + \frac{1}{h} [\nu_\xi + \mu \beta_\xi]) & 2A_H \nu_\eta & A_V \nu_z + A_H w_y \\ A_V \mu_z + A_H \frac{1}{h} w_\xi & A_V \nu_z + A_H w_y & 2A_V w_z \end{bmatrix} \\ &= \rho_0 U_\xi^2 \epsilon \begin{bmatrix} \frac{2A'_H}{h} \left( \frac{\partial \mu'}{\partial \xi'} - \delta \nu' \frac{\partial \beta}{\partial \xi'} \right) & \frac{A'_H}{\delta} \left( \frac{\partial \mu'}{\partial \eta'} + \frac{\delta}{h} \left[ \delta \frac{\partial \nu'}{\partial \xi'} + \mu' \frac{\partial \beta}{\partial \xi'} \right] \right) & A'_V \frac{1}{\epsilon} \frac{\partial \mu'}{\partial z'} + \frac{A'_H}{h} \epsilon \frac{\partial w'}{\partial \xi'} \\ \frac{A'_H}{\delta} \left( \frac{\partial \mu'}{\partial \eta'} + \frac{\delta}{h} \left[ \delta \frac{\partial \nu'}{\partial \xi'} + \mu' \frac{\partial \beta}{\partial \xi'} \right] \right) & 2A'_H \frac{\partial \nu'}{\partial \eta'} & A'_V \frac{\delta}{\epsilon} \frac{\partial \nu'}{\partial z'} + A'_H \frac{\epsilon}{\delta} \frac{\partial w'}{\partial \eta'} \\ A'_V \frac{1}{\epsilon} \frac{\partial \mu'}{\partial z'} + \frac{A'_H}{h} \epsilon \frac{\partial w'}{\partial \xi'} & A'_V \frac{\delta}{\epsilon} \frac{\partial \nu'}{\partial z'} + A'_H \frac{\epsilon}{\delta} \frac{\partial w'}{\partial \eta'} & 2A'_V \frac{\partial w'}{\partial z'} \end{bmatrix}, \end{aligned} \quad (2.82)$$

$\underline{\underline{\sigma}}$  is written as  $\underline{\underline{\sigma}} = \rho_0 U_\xi^2 \epsilon \underline{\underline{\sigma}}'$ .

The steady state momentum equations in the component format in the PC system dimensionally are given by:

$$\begin{aligned} & \frac{\mu}{h} \frac{\partial \mu}{\partial \xi} + \nu \frac{\partial \mu}{\partial \eta} + w \frac{\partial \mu}{\partial z} - \frac{\beta_\xi}{h} \mu \nu + f \left[ -\hat{\Omega}_{\alpha 3} \nu + (\hat{\Omega}_{\alpha 2} \cos \beta - \hat{\Omega}_{\alpha 1} \sin \beta) w \right] \\ & = -\frac{1}{\rho_0 h} \frac{\partial P}{\partial \xi} + \frac{g \sin \alpha \Delta \rho}{\rho_0} \sin \beta + \frac{1}{\rho_0} \left[ \frac{1}{h} \frac{\partial \sigma_{\xi \xi}}{\partial \xi} + \frac{\partial \sigma_{\xi \eta}}{\partial \eta} + \frac{\partial \sigma_{\xi z}}{\partial z} - \frac{\beta_\xi}{h} (\sigma_{\xi \eta} + \sigma_{\eta \xi}) \right], \end{aligned} \quad (2.83)$$

$$\begin{aligned} & \frac{\mu}{h} \frac{\partial \nu}{\partial \xi} + \nu \frac{\partial \nu}{\partial \eta} + w \frac{\partial \nu}{\partial z} \frac{\beta_\xi}{h} \mu^2 + f \left[ \hat{\Omega}_{\alpha 3} \mu - (\hat{\Omega}_{\alpha 1} \cos \beta + \hat{\Omega}_{\alpha 2} \sin \beta) w \right] \\ & = -\frac{1}{\rho_0} \frac{\partial P}{\partial \eta} + \frac{g \sin \alpha \Delta \rho}{\rho_0} \cos \beta + \frac{1}{\rho_0} \left[ \frac{1}{h} \frac{\partial \sigma_{\eta \xi}}{\partial \xi} + \frac{\partial \sigma_{\eta \eta}}{\partial \eta} + \frac{\partial \sigma_{\eta z}}{\partial z} - \frac{\beta_\xi}{h} (\sigma_{\xi \xi} + \sigma_{\eta \eta}) \right], \end{aligned} \quad (2.84)$$

and

$$\begin{aligned} & \frac{\mu}{h} \frac{\partial w}{\partial \xi} + \nu \frac{\partial w}{\partial \eta} + w \frac{\partial w}{\partial z} + f \left[ (-\hat{\Omega}_{\alpha 2} \cos \beta + \hat{\Omega}_{\alpha 1} \sin \beta) \mu + (\hat{\Omega}_{\alpha 1} \cos \beta + \hat{\Omega}_{\alpha 2} \sin \beta) \nu \right] \\ & = -\frac{1}{\rho_0} \frac{\partial P}{\partial z} + \frac{g \cos \alpha \Delta \rho}{\rho_0} + \frac{1}{\rho_0} \left[ \frac{1}{h} \frac{\partial \sigma_{z \xi}}{\partial \xi} + \frac{\partial \sigma_{z \eta}}{\partial \eta} + \frac{\partial \sigma_{z z}}{\partial z} - \frac{\beta_\xi}{h} \sigma_{z \eta} \right]. \end{aligned} \quad (2.85)$$

Non-dimensionalising the three momentum equations above, using the same method car-

ried out for the continuity equation (Equation 2.80), gives:

$$\begin{aligned}
& \frac{U_\xi^2}{L_\xi} \frac{\mu'}{h} \frac{\partial \mu'}{\partial \xi'} + \nu' \frac{U_\eta U_\xi}{L_\eta} \frac{\partial \mu'}{\partial \eta'} + w' \frac{U_z U_\xi}{L_z} \frac{\partial \mu'}{\partial z'} - \mu' \nu' \frac{U_\xi U_\eta}{L_\xi} \frac{\beta_\xi}{h} \\
& + f \left[ -\hat{\Omega}_{\alpha 3} U_\eta \nu' + (\hat{\Omega}_{\alpha 2} \cos \beta - \hat{\Omega}_{\alpha 1} \sin \beta) U_z w' \right] \\
& = -\frac{\Gamma}{L_\xi} \frac{1}{\rho_0 h} \frac{\partial P'}{\partial \xi'} + \frac{g \sin \alpha \Delta \rho}{\rho_0} \sin \beta \\
& + U_\xi^2 \epsilon \left[ \frac{1}{L_\xi h} \frac{\partial \sigma'_{\xi\xi}}{\partial \xi'} + \frac{1}{L_\eta} \frac{\partial \sigma'_{\xi\eta}}{\partial \eta'} + \frac{1}{L_z} \frac{\partial \sigma'_{\xi z}}{\partial z'} - \frac{1}{L_\xi} \frac{\beta'_\xi}{h} (\sigma'_{\xi\eta} + \sigma'_{\eta\xi}) \right],
\end{aligned} \tag{2.86}$$

$$\begin{aligned}
& \frac{U_\xi U_\eta}{L_\xi} \frac{\mu'}{h} \frac{\partial \nu'}{\partial \xi'} + \nu' \frac{U_\eta^2}{L_\eta} \frac{\partial \nu'}{\partial \eta'} + w' \frac{U_z U_\eta}{L_z} \frac{\partial \nu'}{\partial z'} + \mu'^2 \frac{U_\xi^2}{L_\xi} \frac{\beta_\xi}{h} \\
& + f \left[ \hat{\Omega}_{\alpha 3} U_\xi \mu' - (\hat{\Omega}_{\alpha 1} \cos \beta + \hat{\Omega}_{\alpha 2} \sin \beta) U_z w' \right] \\
& = -\frac{\Gamma}{L_\eta} \frac{1}{\rho_0} \frac{\partial P'}{\partial \eta'} + \frac{g \sin \alpha \Delta \rho}{\rho_0} \cos \beta \\
& + U_\xi^2 \epsilon \left[ \frac{1}{L_\xi h} \frac{\partial \sigma'_{\eta\xi}}{\partial \xi'} + \frac{1}{L_\eta} \frac{\partial \sigma'_{\eta\eta}}{\partial \eta'} + \frac{1}{L_z} \frac{\partial \sigma'_{\eta z}}{\partial z'} + \frac{1}{L_\xi} \frac{\beta'_\xi}{h} (\sigma_{\xi\xi} + \sigma_{\eta\eta}) \right],
\end{aligned} \tag{2.87}$$

and

$$\begin{aligned}
& \frac{U_\xi U_z}{L_\xi} \frac{\mu'}{h} \frac{\partial w'}{\partial \xi'} + \nu' \frac{U_\eta U_z}{L_\eta} \frac{\partial w'}{\partial \eta'} + w' \frac{U_z^2}{L_z} \frac{\partial w'}{\partial z'} \\
& + f \left[ (-\hat{\Omega}_{\alpha 2} \cos \beta + \hat{\Omega}_{\alpha 1} \sin \beta) U_\xi \mu' + (\hat{\Omega}_{\alpha 1} \cos \beta + \hat{\Omega}_{\alpha 2} \sin \beta) U_\eta \nu' \right] \\
& = -\frac{\Gamma}{L_z} \frac{1}{\rho_0} \frac{\partial P'}{\partial z'} + \frac{g \cos \alpha \Delta \rho}{\rho_0} \\
& + U_\xi^2 \epsilon \left[ \frac{1}{L_\xi h} \frac{\partial \sigma'_{z\xi}}{\partial \xi'} + \frac{1}{L_\eta} \frac{\partial \sigma'_{z\eta}}{\partial \eta'} + \frac{1}{L_z} \frac{\partial \sigma'_{zz}}{\partial z'} - \frac{1}{L_\xi} \frac{\beta'_\xi}{h} \sigma'_{z\eta} \right].
\end{aligned} \tag{2.88}$$

Rearranging Equation 2.88 gives the following:

$$\begin{aligned}
& \frac{\mu'}{h} \frac{\partial \mu'}{\partial \xi'} + \nu' \frac{L_\xi U_\eta}{L_\eta U_\xi} \frac{\partial \mu'}{\partial \eta'} + w' \frac{U_z L_\xi}{U_\xi L_z} \frac{\partial \mu'}{\partial z'} - \mu' \nu' \frac{U_\eta \beta_\xi}{U_\xi h} \\
& + \left[ - \left( \frac{f L_\xi}{U_\xi} \right) \frac{U_\eta}{U_\xi} \hat{\Omega}_{\alpha 3} \nu' + \left( \frac{f L_\xi}{U_\xi} \right) \frac{U_z}{U_\xi} (\hat{\Omega}_{\alpha 2} \cos \beta - \hat{\Omega}_{\alpha 1} \sin \beta) w' \right] \\
& = - \left( \frac{\Gamma}{\rho_0 U_\xi^2} \right) \frac{1}{\rho_0 h} \frac{\partial P'}{\partial \xi'} + \frac{g L_\xi \sin \alpha \Delta \rho}{U_\xi^2 \rho_0} \sin \beta \\
& + \epsilon \left[ \frac{1}{h} \frac{\partial \sigma'_{\xi\xi}}{\partial \xi'} + \frac{L_\xi}{L_\eta} \frac{\partial \sigma'_{\xi\eta}}{\partial \eta'} + \frac{L_\xi}{L_z} \frac{\partial \sigma'_{\xi z}}{\partial z'} - \frac{\beta'_\xi}{h} (\sigma'_{\xi\eta} + \sigma'_{\eta\xi}) \right], \tag{2.89}
\end{aligned}$$

$$\begin{aligned}
& \frac{\mu'}{h} \frac{\partial \nu'}{\partial \xi'} + \nu' \frac{L_\xi U_\eta}{L_\eta U_\xi} \frac{\partial \nu'}{\partial \eta'} + w' \frac{U_z L_\xi}{U_\xi L_z} \frac{\partial \nu'}{\partial z'} + \mu'^2 \frac{U_\xi \beta_\xi}{U_\eta h} \\
& + \left[ \left( \frac{f L_\xi}{U_\eta} \right) \hat{\Omega}_{\alpha 3} \mu' - \left( \frac{f L_\xi U_z}{U_\xi U_\eta} \right) (\hat{\Omega}_{\alpha 1} \cos \beta + \hat{\Omega}_{\alpha 2} \sin \beta) w' \right] \\
& = - \frac{\Gamma L_\xi}{L_\eta \rho_0 U_\eta U_\xi} \frac{\partial P'}{\partial \eta'} + \frac{g L_\xi \sin \alpha \Delta \rho}{U_\xi U_\eta \rho_0} \cos \beta \\
& + \frac{U_\xi}{U_\eta} \epsilon \left[ \frac{1}{h} \frac{\partial \sigma'_{\eta\xi}}{\partial \xi'} + \frac{L_\xi}{L_\eta} \frac{\partial \sigma'_{\eta\eta}}{\partial \eta'} + \frac{L_\xi}{L_z} \frac{\partial \sigma'_{\eta z}}{\partial z'} + \frac{\beta'_\xi}{h} (\sigma_{\xi\xi} + \sigma_{\eta\eta}) \right], \tag{2.90}
\end{aligned}$$

and

$$\begin{aligned}
& \frac{\mu'}{h} \frac{\partial w'}{\partial \xi'} + \nu' \frac{L_\xi U_\eta}{L_\eta U_\xi} \frac{\partial w'}{\partial \eta'} + w' \frac{U_z L_\xi}{U_\xi L_z} \frac{\partial w'}{\partial z'} \\
& + \left[ \left( \frac{f L_\xi}{U_\eta} \right) (-\hat{\Omega}_{\alpha 2} \cos \beta + \hat{\Omega}_{\alpha 1} \sin \beta) \mu' + \left( \frac{f L_\xi U_\eta}{U_\xi U_z} \right) (\hat{\Omega}_{\alpha 1} \cos \beta + \hat{\Omega}_{\alpha 2} \sin \beta) \nu' \right] \\
& = - \left( \frac{\Gamma L_\xi}{L_\eta \rho_0 U_\eta U_\xi} \right) \frac{\partial P'}{\partial z'} + \frac{g L_\xi \cos \alpha \Delta \rho}{U_z U_\xi \rho_0} \\
& + \frac{U_\xi}{U_z} \epsilon \left[ \frac{1}{h} \frac{\partial \sigma'_{z\xi}}{\partial \xi'} + \frac{L_\xi}{L_\eta} \frac{\partial \sigma'_{z\eta}}{\partial \eta'} + \frac{L_\xi}{L_z} \frac{\partial \sigma'_{zz}}{\partial z'} - \frac{\beta'_\xi}{h} \sigma_{z\eta} \right]. \tag{2.91}
\end{aligned}$$

Defining  $Ro_\xi = U_\xi/fL_\xi$ , and substituting in the definitions of  $\delta$  and  $\epsilon$  from Equation 2.81, where  $\delta = L_\eta/L_\xi = U_\eta/U_\xi$ , and  $\epsilon = L_z/L_\xi = U_z/U_\xi$ , gives:

$$\begin{aligned}
& \frac{\mu'}{h} \frac{\partial \mu'}{\partial \xi'} + \nu' \frac{\partial \mu'}{\partial \eta'} + w' \frac{\partial \mu'}{\partial z'} - \delta \mu' \nu' \frac{\beta_\xi}{h} \\
& + \frac{1}{Ro_\xi} \left[ -\delta \hat{\Omega}_{\alpha 3} \nu' + \epsilon (\hat{\Omega}_{\alpha 2} \cos \beta - \hat{\Omega}_{\alpha 1} \sin \beta) w' \right] \\
& = - \left( \frac{\Gamma}{\rho_0 U_\xi^2} \right) \frac{1}{h} \frac{\partial P'}{\partial \xi'} + \frac{gL_\xi \sin \alpha \Delta \rho}{U_\xi^2 \rho_0} \sin \beta \\
& + \left[ \epsilon \frac{1}{h} \frac{\partial \sigma'_{\xi\xi}}{\partial \xi'} + \frac{\epsilon}{\delta} \frac{\partial \sigma'_{\xi\eta}}{\partial \eta'} + \frac{\partial \sigma'_{\xi z}}{\partial z'} - \epsilon \frac{\beta'_\xi}{h} (\sigma'_{\xi\eta} + \sigma'_{\eta\xi}) \right],
\end{aligned} \tag{2.92}$$

$$\begin{aligned}
& \frac{\mu'}{h} \frac{\partial \nu'}{\partial \xi'} + \nu' \frac{\partial \nu'}{\partial \eta'} + w' \frac{\partial \nu'}{\partial z'} + \mu'^2 \frac{1}{\delta} \frac{\beta_\xi}{h} \\
& + \frac{1}{Ro_\xi} \left[ \frac{1}{\delta} \hat{\Omega}_{\alpha 3} \mu' - \frac{\epsilon}{\delta} (\hat{\Omega}_{\alpha 1} \cos \beta + \hat{\Omega}_{\alpha 2} \sin \beta) w' \right] \\
& = - \left( \frac{\Gamma}{\rho_0 U_\xi^2} \right) \frac{1}{\delta^2} \frac{\partial P'}{\partial \eta'} + \frac{gL_\xi \sin \alpha \Delta \rho}{U_\xi^2 \delta \rho_0} \cos \beta \\
& + \frac{1}{\delta} \left[ \frac{\epsilon}{h} \frac{\partial \sigma'_{\eta\xi}}{\partial \xi'} + \frac{\epsilon}{\delta} \frac{\partial \sigma'_{\eta\eta}}{\partial \eta'} + \frac{\partial \sigma'_{\eta z}}{\partial z'} + \epsilon \frac{\beta'_\xi}{h} (\sigma_{\xi\xi} + \sigma_{\eta\eta}) \right],
\end{aligned} \tag{2.93}$$

and

$$\begin{aligned}
& \frac{\mu'}{h} \frac{\partial w'}{\partial \xi'} + \nu' \frac{\partial w'}{\partial \eta'} + w' \frac{\partial w'}{\partial z'} \\
& + \frac{1}{Ro_\xi} \left[ \frac{1}{\epsilon} (-\hat{\Omega}_{\alpha 2} \cos \beta + \hat{\Omega}_{\alpha 1} \sin \beta) \mu' + \frac{\delta}{\epsilon} (\hat{\Omega}_{\alpha 1} \cos \beta + \hat{\Omega}_{\alpha 2} \sin \beta) \nu' \right] \\
& = - \left( \frac{\Gamma}{\rho_0 U_\xi^2} \right) \frac{1}{\epsilon^2} \frac{\partial P'}{\partial z'} + \frac{gL_\xi \cos \alpha \Delta \rho}{U_\xi^2 \epsilon \rho_0} \\
& + \left[ \frac{1}{h} \frac{\partial \sigma'_{z\xi}}{\partial \xi'} + \frac{1}{\delta} \frac{\partial \sigma'_{z\eta}}{\partial \eta'} + \frac{1}{\epsilon} \frac{\partial \sigma'_{zz}}{\partial z'} - \frac{\beta'_\xi}{h} \sigma_{z\eta} \right].
\end{aligned} \tag{2.94}$$

So the slope-normal equation (Equation 2.94) indicates that the largest pressure gradients are driven by the gravitational term, the Coriolis terms, and the  $\partial\sigma'_{zz}/\partial z'$  term, which is in line with Smith [1975]. In order to balance this, the pressure scale  $\Gamma = \rho_0 U_\xi^2 \epsilon$  is chosen, which has the same order of magnitude as the stress tensor. Therefore the slope-normal equation is an equation for the evolution of the rotating modified pressure,  $P$ , which does not appear at leading order in the streamwise and spanwise momentum equations.

Moving on to the unsteady terms, the natural time scale that keeps the time derivatives in the convective derivative is  $T = L_\xi/U_\xi$ .

The current's path is parametrised by  $\xi$ , such that:

$$X(\xi, t) = \int_0^\xi dX(\zeta) = \int_0^\xi \cos \beta(\zeta, t) d\zeta, \quad (2.95)$$

and

$$Y(\xi, t) = \int_0^\xi dY(\zeta) = \int_0^\xi \sin \beta(\zeta, t) d\zeta, \quad (2.96)$$

where  $\zeta$ , is a dummy parameter. Hence,

$$\left. \frac{\partial X}{\partial t} \right|_\xi = - \int_0^\xi \sin \beta(\zeta, t) \frac{\partial}{\partial t} \beta(\zeta, t) d\zeta, \quad (2.97)$$

and

$$\left. \frac{\partial Y}{\partial t} \right|_\xi = \int_0^\xi \cos \beta(\zeta, t) \frac{\partial}{\partial t} \beta(\zeta, t) d\zeta. \quad (2.98)$$

Thus:

$$\mu_0 = \left. \frac{\partial X}{\partial t} \right|_{\xi} \cos \beta + \left. \frac{\partial Y}{\partial t} \right|_{\xi} \sin \beta = \int_0^{\xi} \sin[\beta(\xi, t) - \beta(\zeta, t)] \frac{\partial}{\partial t} \beta(\zeta, t) d\zeta, \quad (2.99)$$

and

$$\nu_0 = -\left. \frac{\partial X}{\partial t} \right|_{\xi} \sin \beta + \left. \frac{\partial Y}{\partial t} \right|_{\xi} \cos \beta = \int_0^{\xi} \cos[\beta(\xi, t) - \beta(\zeta, t)] \frac{\partial}{\partial t} \beta(\zeta, t) d\zeta. \quad (2.100)$$

### Mass conservation

The mass conservation equation states that:

$$\frac{D\rho}{Dt} = 0 \Rightarrow \frac{\partial \rho}{\partial t} + (\mathbf{u} \cdot \nabla) \rho = 0. \quad (2.101)$$

This can be rotated into the SC system using  $\mathbf{R}_s$ , such that:

$$\frac{\partial \rho}{\partial t} + (\mathbf{u} \cdot \nabla) \rho = 0, \quad (2.102)$$

and by using rotation matrix  $\mathbf{R}_p$ , along with the results from Equation 2.47, gives:

$$\frac{\partial \rho}{\partial t} + \frac{1}{h} \frac{\partial}{\partial \xi} (\rho \mu) + \frac{\partial}{\partial \eta} (\rho \nu) + \frac{\partial}{\partial z} (\rho w) + \frac{\eta \beta_t - \mu_0}{h} \frac{\partial \rho}{\partial \xi} - \nu_0 \frac{\partial \rho}{\partial \eta} - \frac{\rho \nu}{h} \frac{\partial \beta}{\partial \xi} = 0. \quad (2.103)$$

The above equation (Equation 2.103) can be non-dimensionalised as:

$$\frac{\partial \rho'}{\partial t'} + \frac{1}{h} \frac{\partial}{\partial \xi'} (\rho' \mu') + \frac{\partial}{\partial \eta'} (\rho' \nu') + \frac{\partial}{\partial z'} (\rho' w') + \frac{\delta \eta' \beta'_t - \epsilon \mu'_0}{h} \frac{\partial \rho'}{\partial \xi'} - \epsilon \nu'_0 \frac{\partial \rho'}{\partial \eta'} - \frac{\delta \rho' \nu'}{h} \frac{\partial \beta}{\partial \xi'} = 0. \quad (2.104)$$

Equations (2.78), (2.92) to (2.94) and (2.104), give, the non-dimensionalised, volume, momentum, and mass conservation equations respectively.

## 2.4.6 Cross-sectional averaging to find bulk quantity equations

Assuming a top-hat profile for the current under the assumption of a rectangular cross-section  $(\eta, z) \in [-l, l] \times [0, d] = \mathcal{D}$ , where  $l = l(\xi, t)$ , and  $d = d(\xi, t)$ , as stated previously, while taking  $h = 1$  (Smith [1975]) gives:  $\epsilon \ll \delta \ll 1$ , and taking the following kinematic boundary conditions that require the boundary of the plume cross-section to move with the local plume velocity, such that velocities at the boundary are:

$$\nu = \frac{dl}{dt} = \frac{\partial l}{\partial t} + \mu \frac{\partial l}{\partial \xi}, \quad (2.105)$$

and,

$$w = \frac{dd}{dt} = \frac{\partial d}{\partial t} + \mu \frac{\partial d}{\partial \xi}, \quad (2.106)$$

integrating over the right half of  $\mathcal{D}$ , and using symmetry, Equation 2.7 gives:

$$\begin{aligned} \frac{E_0 \mu}{2} &= \int_{\mathcal{D}R} \left[ \frac{\partial \mu}{\partial \xi} + \frac{\partial \nu}{\partial \xi} + \frac{\partial w}{\partial \xi} \right] dA \\ &= \int_0^d \int_0^l \frac{\partial \mu}{\partial \xi} d\eta dz + \int_0^d \int_0^l \frac{\partial \nu}{\partial \xi} d\eta dz + \int_0^d \int_0^l \frac{\partial w}{\partial \xi} d\eta dz \\ &= \left\{ \int_0^d \frac{\partial}{\partial \xi} \left[ \int_0^l \mu d\eta \right] dz - \int_0^d \left[ \frac{\partial l}{\partial \xi} \mu \Big|_{\eta=l} \right] dz \right\} \int_0^d \nu \Big|_{\eta=l} dz + \int_0^l w \Big|_{z=d} d\eta, \end{aligned} \quad (2.107)$$

where use has been made of  $\nu(\eta = 0) = 0$  by symmetry and  $w(z = 0) = 0$ , a no

penetration condition at the base of the current.

Hence,

$$\begin{aligned}
\frac{E_0\mu}{2} &= \int_0^d \frac{\partial}{\partial \xi} \left[ \int_0^l \mu d\eta \right] dz + \int_0^d \left[ \nu \Big|_{\eta=l} - \frac{\partial l}{\partial \xi} \mu \Big|_{\eta=l} \right] dz + \int_0^l w \Big|_{z=d} d\eta \\
&= \left\{ \frac{\partial}{\partial \xi} \int_0^d \int_0^l \mu d\eta dz - \frac{\partial d}{\partial \xi} \left[ \int_0^l \mu d\eta \right]_{z=d} \right\} \\
&\quad + \int_0^d \left[ \nu \Big|_{\eta=l} - \frac{\partial l}{\partial \xi} \mu \Big|_{\eta=l} \right] dz + \int_0^l w \Big|_{z=d} d\eta.
\end{aligned} \tag{2.108}$$

As  $d$  is independent of  $\eta$ , it is given that:

$$\frac{E_0\mu}{2} = \frac{1}{2} \frac{\partial}{\partial \xi} (\mu A) + \int_0^d \left[ \nu \Big|_{\eta=l} - \frac{\partial l}{\partial \xi} \mu \Big|_{\eta=l} \right] dz + \int_0^l \left[ w \Big|_{z=d} - \frac{\partial d}{\partial \xi} \Big|_{z=d} \right] d\eta. \tag{2.109}$$

Since both  $l$  and  $d$  are independent of  $\eta$  and  $z$ , Equation 2.109 can be written as:

$$\frac{E_0\mu}{2} = \frac{1}{2} \frac{\partial}{\partial \xi} (\mu A) + d \frac{\partial l}{\partial t} + l \frac{\partial d}{\partial t}. \tag{2.110}$$

So, in terms of the current cross-sectional area  $A$  (making use of symmetry), the continuity equation implies that:

$$\frac{\partial A}{\partial t} + \frac{\partial}{\partial \xi} (\mu A) = E_0\mu. \tag{2.111}$$

For the mass conservation equation (Equation 2.8), taking  $h = 1$ , while assuming a top-hat profile for the current density  $\rho$ , and applying the kinematic boundary conditions

given in Equation 2.105 and Equation 2.106, having integrated the lhs over the current cross sectional area, gives:

$$\frac{\partial}{\partial t}(\rho A) + \frac{\partial}{\partial \xi}(\rho \mu A) = \rho_e E_0 \mu. \quad (2.112)$$

Taking the streamwise momentum equation (Equation 2.92), and removing terms of order  $\delta$  (this removes the Coriolis term), gives::

$$\frac{\partial \mu}{\partial t} + \mu \frac{\partial \mu}{\partial \xi} + \nu \frac{\partial \mu}{\partial \eta} + w \frac{\partial \mu}{\partial z} = \frac{g \sin \alpha \Delta \rho}{\rho_0} \sin \beta + \frac{1}{\rho_0} \frac{\partial \sigma_{\xi z}}{\partial z}. \quad (2.113)$$

This can be written in conservative form as:

$$\frac{\partial}{\partial t}(\rho \mu) + \frac{\partial}{\partial \xi}(\rho \mu^2) + \frac{\partial}{\partial \eta}(\rho \mu \nu) + \frac{\partial}{\partial z}(\rho \mu w) - \mu \left[ \frac{D\rho}{Dt} + \rho \nabla \cdot \mathbf{u} \right] = g A \sin \alpha \Delta \rho \sin \beta + \frac{\partial \sigma_{\xi z}}{\partial z}. \quad (2.114)$$

The term in the square brackets cancels with the drag due to entrainment when integrated over the area,  $A$ . Hence,

$$\frac{\partial}{\partial t}(\rho A \mu) + \frac{\partial}{\partial \xi}(\rho A \mu^2) = g A \sin \alpha \Delta \rho \sin \beta + \int_{\mathcal{A}} \frac{\partial \sigma_{\xi z}}{\partial z} dA. \quad (2.115)$$

The stress term, as it is in Smith [1975], is expressed as  $-\rho K \mu^2$ . Therefore, the momentum equation in the streamwise direction is given by:

$$\frac{\partial}{\partial t}(\rho A \mu) + \frac{\partial}{\partial \xi}(\rho A \mu^2) = g A \sin \alpha \Delta \rho \sin \beta - \rho K \mu^2. \quad (2.116)$$

The spanwise momentum equation (Equation 2.93) has leading order terms at  $\delta^{-1}$  which

yields:

$$\beta_\xi \mu^2 + \beta_t \mu + \hat{f} \mu = \frac{g \sin \alpha \Delta \rho}{\rho_0} \cos \beta + \frac{1}{\rho_0} \frac{\partial \sigma_{\eta z}}{\partial z}. \quad (2.117)$$

Removal of the stress tensor term by consideration of the stress tensor components in ‘Method 2’, noting that  $\sigma'_{\eta z} \sim O(\delta \sigma'_{\xi z})$ , and so is an order of magnitude smaller than the remaining terms of the equation. Physically, this implies that there is a greater stress on the current due to the downstream drag against the ‘slope’ as opposed to spanwise drag.

### Full cross-section integrated unsteady stream boundary system

$$A_t + (\mu A)_\xi = E_0 \mu. \quad (2.118)$$

$$(\rho A)_t + (\rho \mu A)_\xi = E_0 \mu \rho_e. \quad (2.119)$$

$$(\rho A \mu)_t + (\rho A \mu^2)_\xi = g A \sin \alpha \Delta \rho \sin \beta - \rho K \mu^2. \quad (2.120)$$

$$\beta_t + \mu \beta_\xi = \frac{g \sin \alpha \Delta \rho}{\rho \mu} \cos \beta - \hat{f}, \quad (2.121)$$

where:

$$\Delta \rho = \rho(\xi) - \rho_e(\xi), \quad (2.122)$$

$$\rho_e(\xi) = \rho_0 [1 + s \hat{T} Y(\xi)]. \quad (2.123)$$

Above are the unsteady version of (5)-(8) in Smith [1975]. This system is for the four

unknowns  $(\mu, A, \rho, \beta)$ . The current path can be calculated at any time  $t$  using:

$$X(\xi, t) = \int_0^\xi \cos \beta(\zeta, t) d\zeta, \quad (2.124)$$

and

$$Y(\xi, t) = \int_0^\xi \sin \beta(\zeta, t) d\zeta. \quad (2.125)$$

This is the full comprehensive, non-linear set of equations which can model time-dependent boundary currents in rotating systems.

## Chapter 3

# Methodology, and steady state current's flow in a homogeneous ambient

This chapter will look into results from a steady state perspective, specifically into an extension of the work carried out by Smith [1975]. Next, the study presents an investigation into the effects of varying the initial state variables of a steady state streamtube dense current on the propagation of the current. Finally the consequences of changing the rotational rate of the system, the drag and entrainment coefficients of the flow and the slope angle are presented and analysed. To start, before presenting any of the results, the numerical methods used in the computational analysis to reach both the steady and unsteady results in this study are covered.

### 3.1 Methodology

The numerical method used to produce the results throughout the thesis was a marching finite difference first order explicit method. The scheme was one dimensional, in space only, for the steady state currents, and two dimensional, in both space and time, for the unsteady currents. The main controlling factor for such schemes is the numerical discretisation applied when producing the results. Here a convergence, studied based on a total Euclidean distance, is presented to show how the results tend to a solution as the numerical accuracy is increased.

The Euclidean distance for two sets of data with  $N$  points each, where:  $\underline{a} = (a_1, a_2, a_3, \dots, a_n)$  and  $\underline{b} = (b_1, b_2, b_3, \dots, b_n)$ , is:  $D_{Ed} = \sqrt{\sum_{i=1}^N (b_i - a_i)^2}$ .

First, in the steady state case, working only on a spatial discretisation, a current of 100 km in length was used, the numerical step size was varied, and the total Euclidean distance between the current with the smallest step size and every other current was measured.

To start off with, a solution using a step size of 0.25 m was generated and saved as a comparison tool for the rest of the solutions with the different step sizes. In order to compare the results, the function “interp” was used in Matlab, this function returns interpolated values at specific query points using linear interpolation, which in turn allows for the comparison of two different currents to be carried out.

Each current was used to generate 400,000 data points along the current’s path (this number comes from using a step size of 0.25 m over a 100 km total length), and the corresponding points across each current were compared. The comparison was a simple measure of the physical distance between the two predicted locations of each current at those downstream locations. After each pair of the 400,000 points was compared, a total

Euclidean distance between the two currents would be generated by summing up all the individual distances. Later a plot was generated which compares the step size used for each current with the total Euclidean distance of that current with the current generated using the 0.25 m step size. Figure 3.1 shows the overall result of this method, a total of 10,000 step sizes were used starting from 0.25 m to 3900 m.

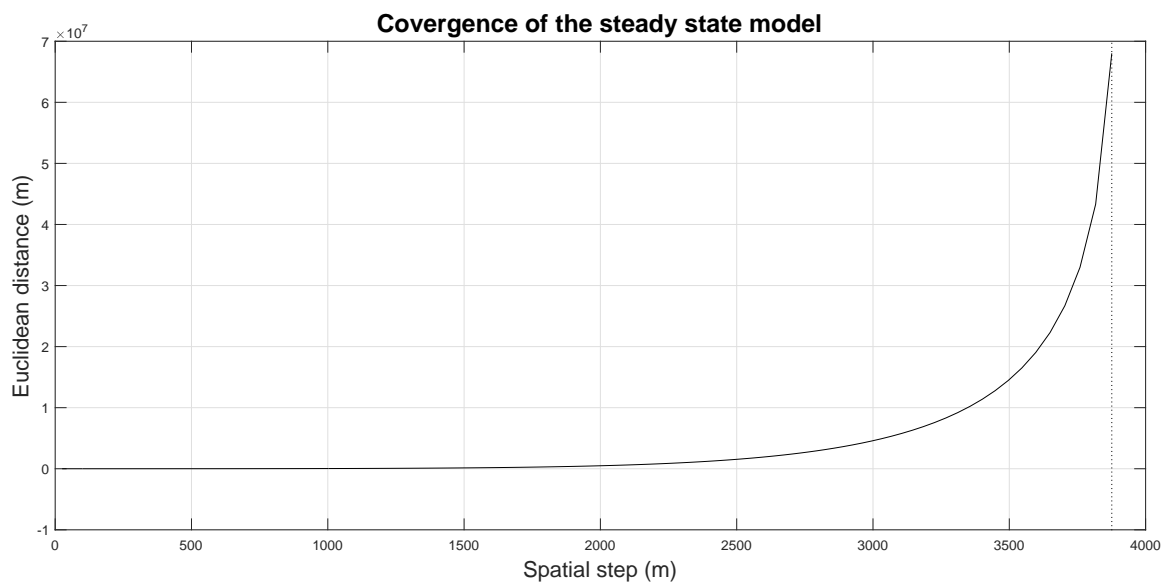


Figure 3.1: A convergence study for the numerical discretisation of the step size for the steady state current solutions using a total Euclidean distance approach.

It can be seen that the results, which are a tool to represent the position or location of the current path under investigation, depend on the numerical discretisation of the scheme used. The results are within line of the expected outcomes for a finite difference first order explicit scheme, as the spatial step is decreased a better accuracy for the final solution is achieved. Moving forward, due to the computation power available for this specific study, and looking at moving to the unsteady case, the results obtained here were used as a justification for choosing a step size which would allow a faster generation of results with an acceptable numerical error.

In order to do this, a more rigorous method was used to see how exactly the first order

system converges. A log-log graph, shown here in Figure 3.2, was generated using the data from Figure 3.1. The system was found to have two different regions of convergence. The total Euclidean distance was found to decrease by an order of 1.9 for spatial step sizes of 500m and less. For spatial step size larger than that, the total Euclidean distance was found to increase at magnitude with a high order.

To further quantify this, a step size of 500 *m* for a 100 *km* current, has a total Euclidean distance of under 6000 *m* when compared to a step size of 0.25 for the same current length using 400,000 data points along both currents. A total Euclidean distance of 6000 *m* over 400,000 data points translates to an average of 15 *mm* error for each data point. The maximum Euclidean distance measured when comparing all 400,000 data points for the two currents using the 0.25 and 500 *m* step sizes, was found to be just over 10 *m* which occurred in the first step of the current generated using the 500 *m* step size, with the minimum Euclidean distance coming being 0.01 *mm* at the end of the current. This increase reduces the computational time by a factor of nearly 1/100 which is very significant especially when moving onto the unsteady case where both time and space will be varied. These results were found to be good and justify using a spatial step size of 500 *m* moving forward.

This approach was repeated for twenty five different total current lengths, varying from 100 *m* to 50 *km*, and a convergence study was carried out for each current using the same method above. However, due to the lower total amounts of the Euclidean distances generated, especially for the shorter currents, a visual representation on the same graph was found to be unhelpful.

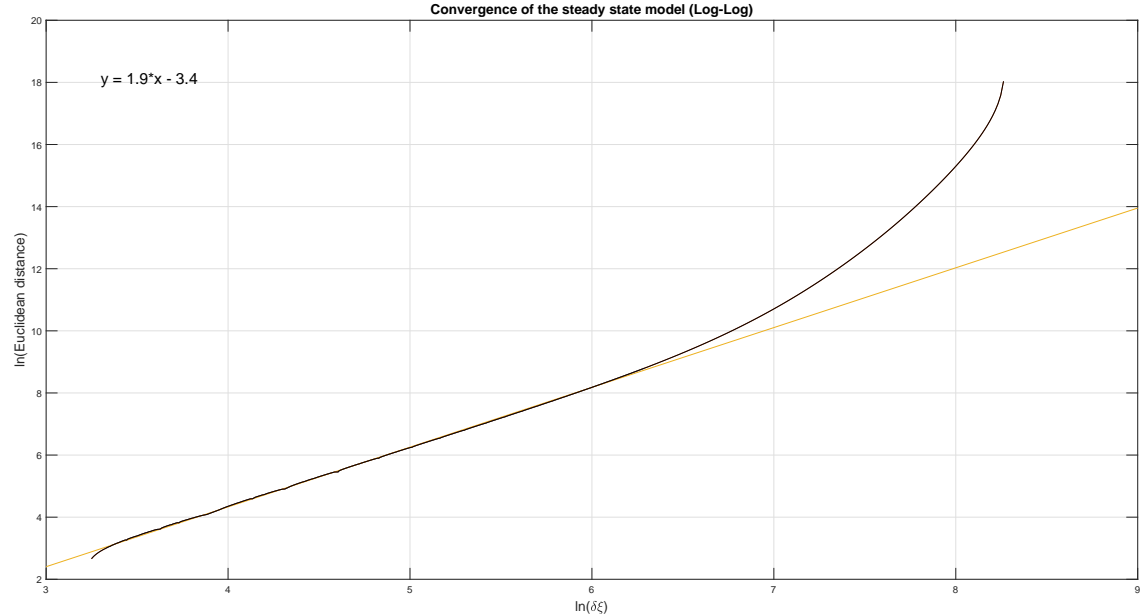


Figure 3.2: A Log-Log plot for the convergence study in Figure 3.1. Here the natural logarithms of both the spatial step size, and the total Euclidean distance are plotted against each other. A linear fit is plotted over the range from  $\ln(\delta\xi) = 3.4$  to 6.3 which is where the convergence was found to be linear.

After establishing the required spatial step for the steady state numerical solutions. The stability of the unsteady case was considered. When working with a finite difference method, in a two dimensional system, using an explicit numerical marching scheme, it is found that the Courant-Fredrick-Levy (CFL) condition limits the time step of the computation depending on the spatial step used, as well as the current's speed (Jameson [1983]; Jameson [1991]; Hamrick [1992]; Chang and Wang [2002]).  $CFL = u \times \Delta t / \Delta \xi$ , where  $u$  is the current velocity,  $\Delta \xi$  is the spatial step, and  $\Delta t$  is the temporal step of the computation.

In order to identify a time step that offers both stability and accuracy for the system. The spatial step was fixed and the time step was varied till the stability limit was found, the convergence of the system under the different time steps was also considered. This was repeated for 100 different spatial steps. It was found that the model was stable

for CFL values that are less than one, therefore the limit of the Courant-Fredrick-Levy number was set to be one, and all the results in the thesis were produced to allow for this limitation.

Figure 3.3 gives a visualisation of the convergence of the model when the spatial step size is set to 500 m. Here 1000 time steps were used starting from 1s to 500s. The current's final position after 12 days across all time steps was then compared with that of the position generated by the 1s step. The total Euclidean distance between each two current was then measured. It is important to note that using the Euclidean distance to generate a convergence study for a time step of a non linear model was not found to be the best approach. However, it was a very good indicator of when the current was stable. The problems faced were due to the current's position oscillating about the same physical location.

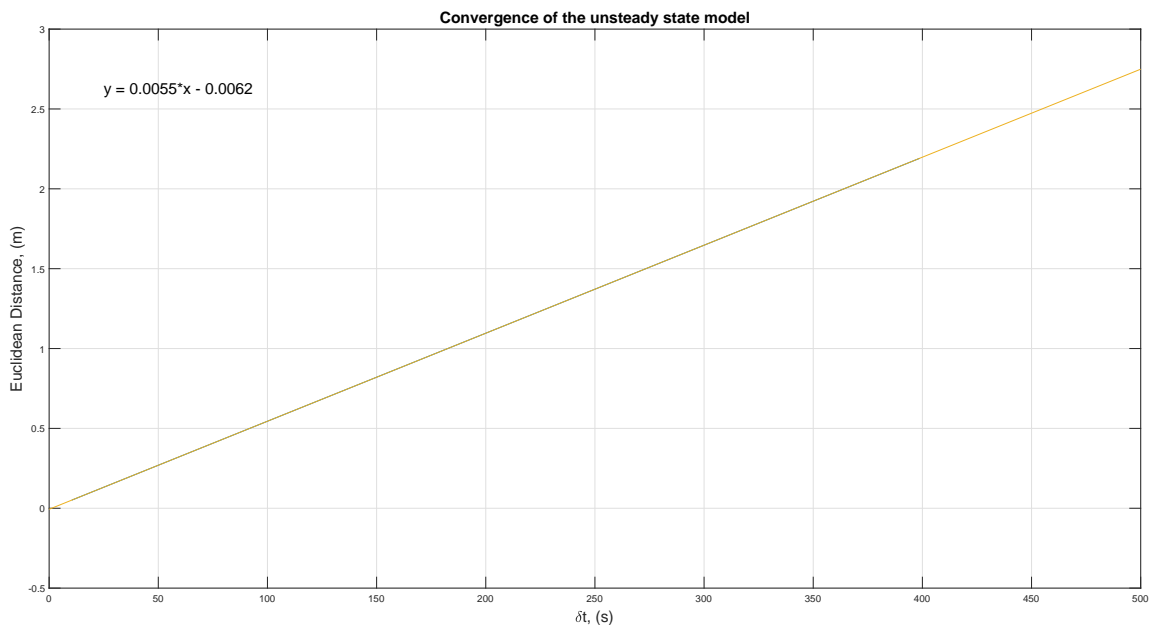


Figure 3.3: A convergence study for the numerical discretisation of the time step size for the unsteady state current solutions using a total Euclidean distance approach. The initial current's velocity was oscillated between  $0.92$  and  $1m.s^{-1}$  using a period of 24 hours. The current was modelled over a total time of 12 days.

## 3.2 Comparison with Smith (1975)

The newly developed system detailed in Chapter 2 is based on the steady state streamtube model used by Smith [1975] for modelling the Mediterranean and Norwegian outflows. The results obtained by Smith [1975] for the Mediterranean outflow are reproduced here using the new system. The source conditions chosen are taken from Smith [1975] ( Table 2) and are presented here in Table 3.1.

Mediterranean outflow		
Quantity	Symbol	Value $\pm$ error
Bottom slope	$s = \tan \alpha$	$(1.43 \pm 0.4) \times 10^{-2}$
Coriolis parameter	$\hat{f} = 2\Omega \cos \alpha$	$(0.854 \pm 0.060) \times 10^{-4} \text{ s}^{-1}$
Ambient stratification rate	$\hat{T} = T \cos \alpha$	$(1.00 \pm 0.15) \times 10^{-6} \text{ m}^{-1}$
Characteristic density	$\rho_0$	$1000 \text{ kg m}^{-3}$
Gravitational acceleration	$g$	$9.81 \text{ m s}^{-2}$
Initial density contrast	$\Delta\rho_0$	$1.25 \text{ kg m}^{-3}$
Initial cross-sectional area	$A_0$	$2.1 \times 10^6 \text{ m}^2$
Initial pitch angle	$\beta_0$	$0.7185 \text{ rad}$
Initial velocity	$\mu_0$	$0.96 \text{ m s}^{-1}$
Drag coefficient	$K$	$500 \text{ m}$
Entrainment coefficient	$E_0$	$50 \text{ m}$

Table 3.1: Physical constants and initial conditions for the Mediterranean outflow

In this case, the source conditions are kept constant, giving time derivatives equal to zero. It can be seen from Figure 3.4 that the red dots' plot matches that of the Mediterranean outflow of Smith [1975]. In the case of Smith, the entrainment and drag coefficients were

varied to try and match observations.

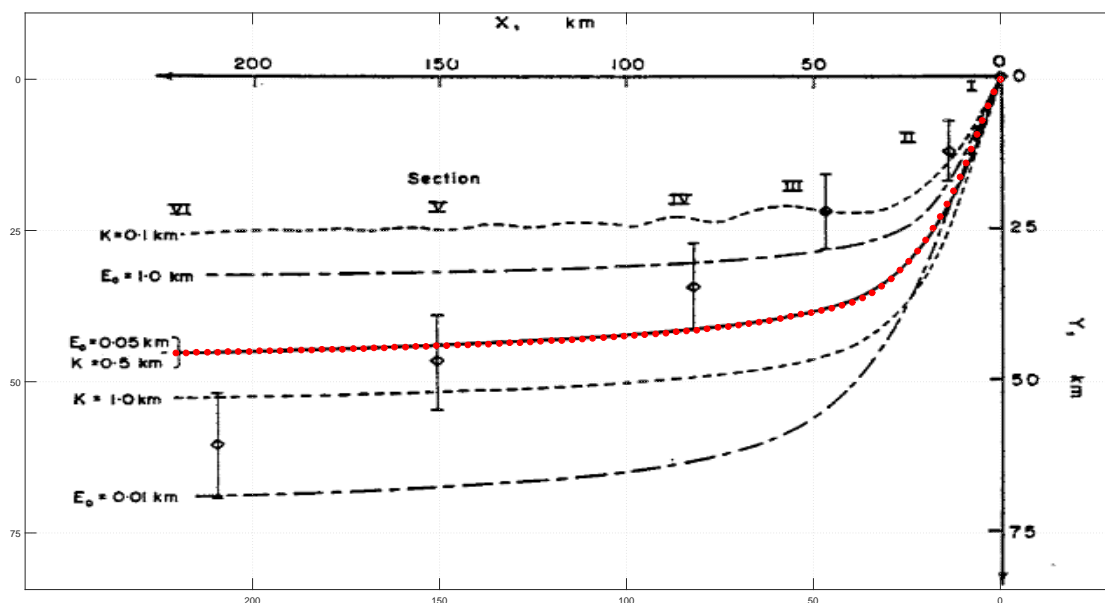


Figure 3.4: The results from Smith [1975] (Figure 12) are matched against the newly derived unsteady stream tube system of equations in chapter 2. The initial conditions are shown in Table 3.1 and the axes are fitted over a figure from Smith [1975]. The new result of the path is plotted in red dots.

Looking at Figure 3.4, it can be seen that for the dashed line plot labelled with the drag coefficient  $K=0.1$  km, the current experiences an oscillating (wave) behaviour as it starts travelling across the slope. As the current is travelling through a stratified ambient, it is expected to experience ‘internal’ waves [Cenedese and Adduce, 2008]. These waves have been studied both numerically (using ocean models) and experimentally as mentioned previously. However, this thesis will look into these waves using the streamtube approach, where the current is modelled as one coherent structure. Before this is carried out, the background stratification is removed and the effects of the state variables, and state parameters are investigated. This is done in order to isolate the effects of each of the variables and constants, and is carried out by changing the initial value of each of the variables, and investigating the effects this has on the propagation of the current.

### 3.3 The effects of different initial state variables

Taking the Mediterranean outflow conditions used in Smith [1975] and presented here in Table 3.1, each one of the four state variables is varied (i.e. three different steady state solutions are presented for each variable), and the current path for each set of initial conditions is plotted. In addition to the path the current propagates down, the downstream profiles of each of the state variables are plotted in order to study the effects that the change of each of the state variables has on the current down-stream physics and dynamics.

The current velocity at the source is given a value of  $0.96 \text{ m s}^{-1}$  [Smith, 1975], which is used for the first run when investigating the effects that the initial velocity has on the propagation of the current. The value of the initial velocity is then set to  $0.48 \text{ m s}^{-1}$  for the second run, before increasing it to  $1.44 \text{ m s}^{-1}$  for the third and final run. These values are chosen to equate to a 50% reduction and a 50% increase from the base case value which is  $0.96 \text{ m s}^{-1}$ . These values are not based on any physical observations; they are chosen to give an indication of how the current would behave under the condition of increasing/decreasing the specific state variable or parameter. The currents' paths generated from changing the initial velocity value are presented in the top left panel of Figure 3.5, whereas the down-stream profiles of the state variables associated with these three tests are plotted in Figure 3.6. The cross-sectional area for the Mediterranean outflow, as presented by Smith [1975], has an initial value of  $2.1 \times 10^6 \text{ m}^2$ . This is reduced to  $1.05 \times 10^6 \text{ m}^2$  (50% of the original value) for the second run, and then increased to  $3.15 \times 10^6 \text{ m}^2$ , which represents a 50% increase in the original value, for the third run. The top right panel of Figure 3.5 gives the three paths that the current would follow in the case of the three different initial cross-sectional areas, and Figure 3.7 shows the downstream profiles of the four state variables for these currents. Smith [1975] set the initial

current density to a value of  $1001.25 \text{ kg m}^{-3}$ , with an ambient density at the source of  $1000 \text{ kg m}^{-3}$ , and this gave a density anomaly of  $1.25 \text{ kg m}^{-3}$ . The initial density is then set to  $1000.624 \text{ kg m}^{-3}$ , with the ambient density kept at  $1000 \text{ kg m}^{-3}$ , giving a density anomaly of  $0.624 \text{ kg m}^{-3}$  for the second run. For the third density run, the initial current density is increased to  $1001.876 \text{ kg m}^{-3}$ , again keeping the ambient density constant at  $1000 \text{ kg m}^{-3}$ , which gives a density anomaly of  $1.876 \text{ kg m}^{-3}$ . The paths of the currents with different initial densities are plotted in the bottom left panel of Figure 3.5, with the state variables' down-stream profiles in Figure 3.8. Finally, the current's initial pitch angle or inclination ( $\beta$ ) is changed. The initial value for the Mediterranean outflow is found to be just under  $\pi/4$ , at 0.7185. This is first set to zero, and then to  $\pi/2$ , which means that the current is first directed across the slope in the positive  $x$  direction, then directly down the slope, along the positive  $y$  direction. The current's three paths are plotted on the bottom right panel of Figure 3.5, whereas the down-stream profiles of the four state variables are shown in Figure 3.9.

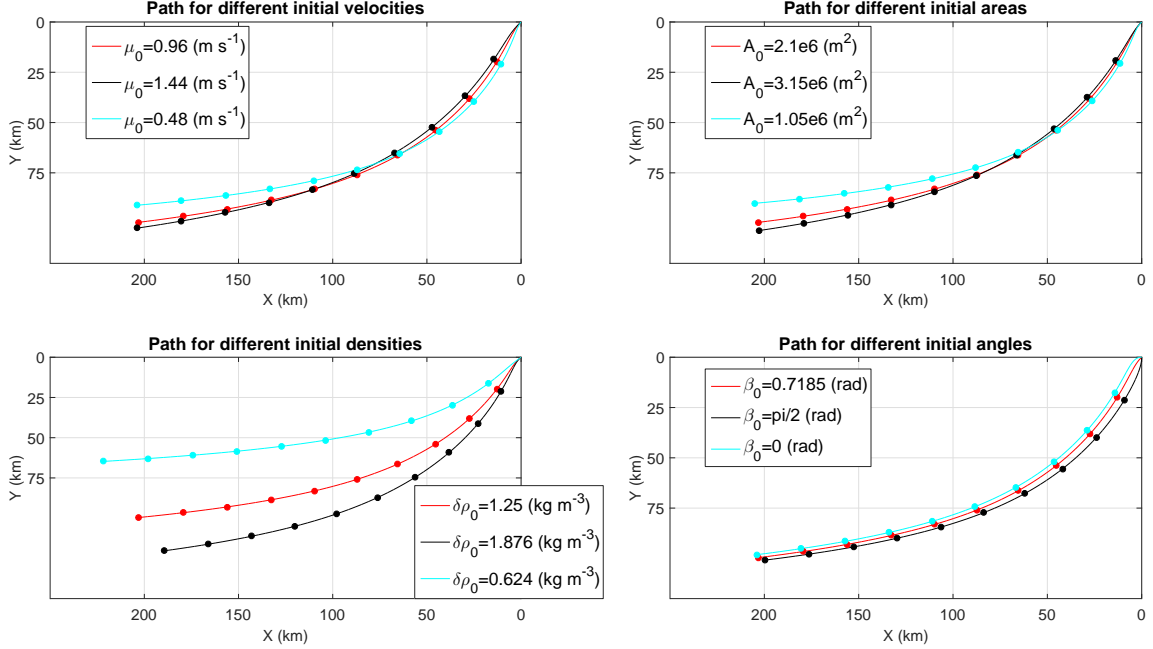


Figure 3.5: Four plots for the paths that the 12 different currents follow as they move in a stratified rotating ambient. The top left panel has three different currents with a varying initial cross-sectional area, whereas in the top right panel the parameter that is varied is the initial velocity. In the bottom left panel, the density anomaly is varied by varying the current's source density, and finally the initial angle between the current and the  $x$  axis is varied to obtain the bottom right panel. The dots represent 25 km intervals along the current path.

Figure 3.5 gives the paths for all 12 currents described above. Each panel has the Mediterranean outflow case plotted in red, with the lower value of the state variable associated with the panel in light blue, and the higher value in black. First of all, looking at both the initial cross-sectional area and velocity variations, it can be seen that the currents' paths experience a similar affect. Decreasing either the initial velocity or the initial cross-sectional area causes the dense current to have a trajectory that makes the current travel further down the slope initially before turning across the slope as can be seen in Figure 3.5. Killworth [1977] showed that dense currents can experience acceleration down the slope, but his results stem from the difference in temperature between the current and the ambient acting as a source of internal energy. However, the streamtube used here, based on Smith [1975], does not account for such variability. This motion of the

current can be explained by looking into the non-linear set of equations that govern this phenomena (Equations (2.118) and (2.121)). Looking at the two momentum equations in the streamwise (Equation 2.120) and spanwise (Equation 2.121) directions, and setting the time derivatives to zero, it can be seen that the smaller the velocity term ( $\mu$ ) is, the higher the buoyancy force would be in comparison with Coriolis, causing the current to be directed down the slope. In the case of the smaller initial cross-sectional area, the current slows down initially as it has less momentum. This deceleration affects the balance between buoyancy and Coriolis, causing the current to be directed down the slope first as explained above.

The change of the initial current density has the biggest effect on the current path, as can be seen in the bottom left panel of Figure 3.5. This outcome is expected, as the only driving force causing the current to travel down the slope is buoyancy. The smaller the density anomaly, the smaller the driving force is, hence, Coriolis dominates the flow. Finally, changing the current's initial inclination had the least effect on the current path. It was found that if the other three state variables are kept constant, then the current would follow the same profile, with a small adjustment near the source to account for the initial trajectory. The down-stream profiles of the state variables are investigated next.

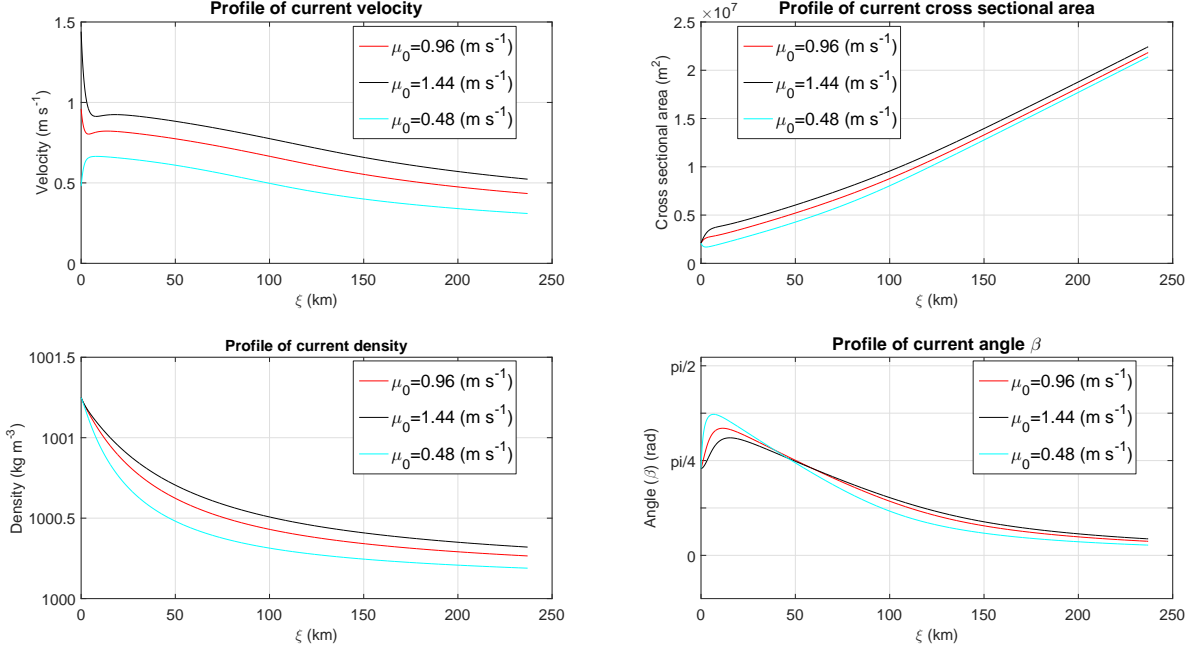


Figure 3.6: Four plots for the state variables' profiles, as a function of the down-stream distance. The initial velocity of the current at the source is the difference between each of the three currents.

Starting with the down-stream profiles for the different initial current velocities, it can be seen that the current first experiences a rapid change in the velocity profile depending on the initial velocity. For the lower initial velocity of  $0.48 \text{ m s}^{-1}$ , the current accelerates first before decelerating, and this is coupled with a reduction in the cross-sectional area of the current. As the cross-sectional area decreases while the current is entraining fluid from the ambient, the density of the current decreases faster than the other two currents, and this is due to the smaller cross-sectional area. The higher initial velocity of  $1.44 \text{ m s}^{-1}$  causes the current to decelerate first, which in effect increases the cross-sectional area to account for conservation of volume. With a higher initial velocity, the current initially travels across the slope further than a lower velocity current would. The plot for the current inclination shows that all three currents experience an initial change of direction causing them to move further down the slope before being redirected across it. For a static observer, the fact that the lower velocity current is directed closer to  $\pi/2$  than the

faster moving currents gives the suggestion that the higher velocity currents do not get directed down the slope, which is not the case.

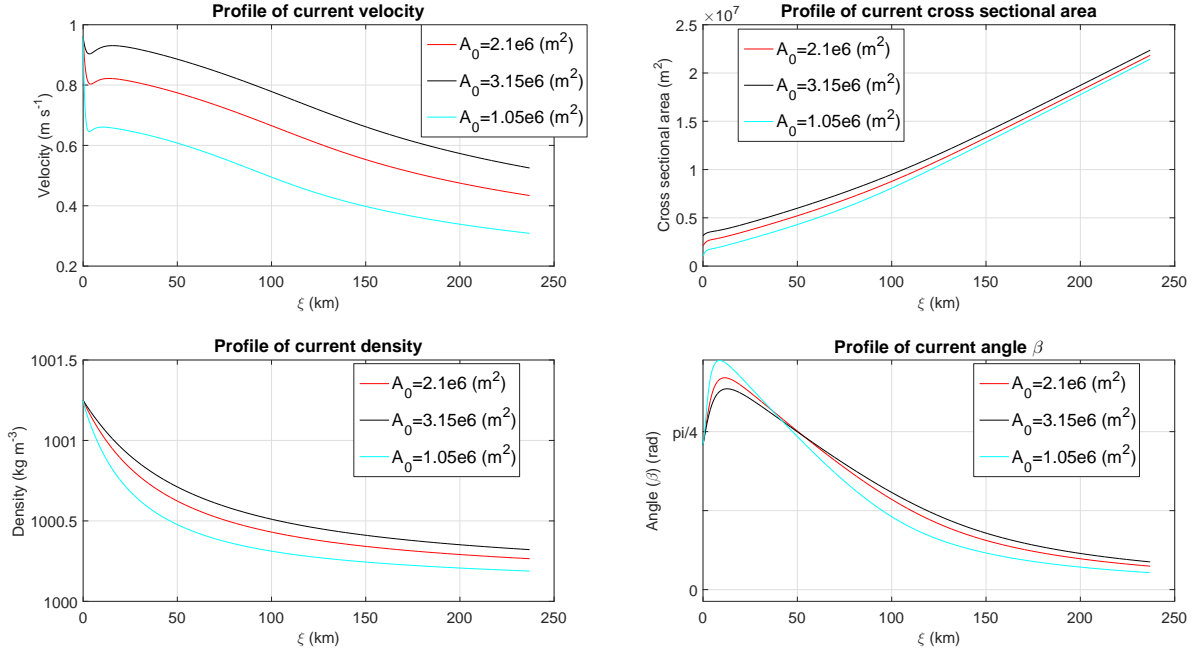


Figure 3.7: Four plots for the state variables' profiles as a function of the down-stream distance. The initial current cross-sectional area at the source is the difference between each of the three currents.

The down-stream profiles for the currents with different initial cross-sectional areas, shown above in Figure 3.7, give similar profiles for down-stream current inclination as do currents with different initial velocities. The currents plotted using the light blue color, corresponding to the lower cross-sectional area and velocity, get diverted further down the slope. However, the difference observed here is that all three currents experience a deceleration coupled with an increase in the cross-sectional area, with the lowest cross-sectional area experiencing more deceleration as it adjusts onto the slope. The down-stream density profiles show the expected. The smaller the cross-sectional area, the steeper the density falls as a function of the down-stream distance, as there is less mass for the ambient to mix with.

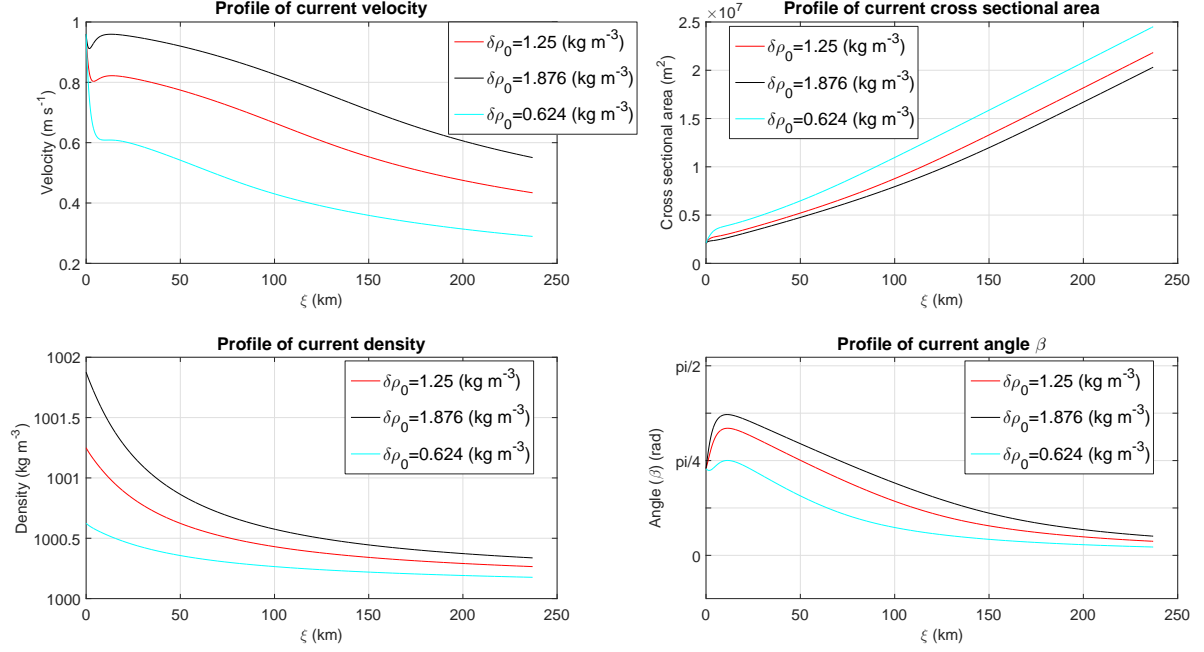


Figure 3.8: Four plots for the state variables' profiles, as a function of the down-stream distance. The initial source density is the difference between each of the three currents.

Looking at the currents with different initial densities, it can be seen from the down-stream profiles of the state variables in Figure 3.8, in comparison with the currents having different initial velocities and cross-sectional areas, that the density anomaly change has the biggest impact on the down-stream evolution of the current. Equation 2.121 indicates that a smaller density anomaly means that Coriolis would dominate the current path, as illustrated in Figure 3.5, where currents with the smaller density anomaly turn across the slope earlier than the currents with the higher density anomalies. However, by looking into the inclination profile plot, shown bottom right in Figure 3.8, it can be seen that the current with the smallest density anomaly (light blue) starts by turning across the slope first then down the slope, before being redirected across the slope again. This is explained by the fact that the current is dominated by Coriolis to start with, causing a rapid deceleration and an increase in the cross-sectional area, affecting the momentum balance, and redirecting the current briefly down the slope before Coriolis dominates again.

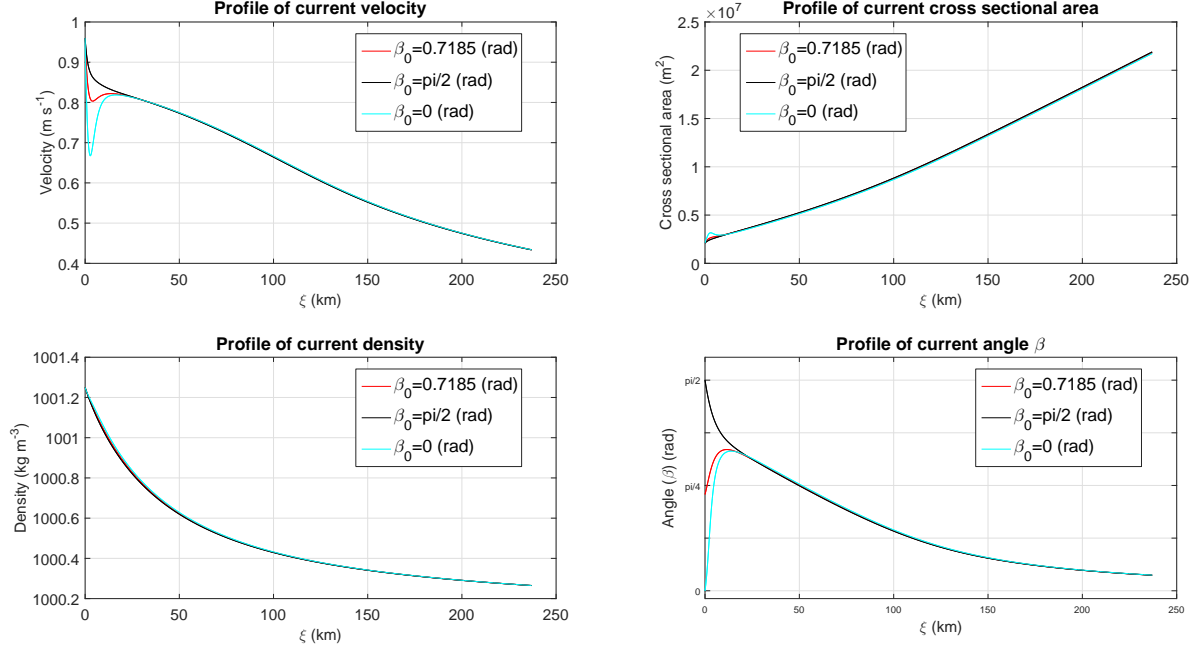


Figure 3.9: Four plots for the state variables' profiles, as a function of the down-stream distance. The initial pitch angle for the current is the difference between each of the three currents.

Figure 3.9 displays the down-stream profiles of the four state variables for three currents with different initial pitch angles ( $\beta$ ). These results show that the current down-stream evolution has very little dependency on the initial angle. After a short period of adjusting, which is due to the initial angle, the current will follow one solution for all the four state variable profiles that is dependant on the initial cross-sectional area, velocity, and density anomaly.

The above results show that the down-stream evolution of a dense steady state current, travelling through a homogeneous ambient, can be affected by the change of the initial state variables. For any set of initial conditions, the current has one state that it wants to follow, causing the current to readjust closer to the source to reach that state; this was observed in the rapid acceleration and deceleration of the currents, coupled with the change in the cross-sectional areas.

### 3.4 The effects of different state parameters

Having tested the effects that the changes in the initial values of the state variables have on the current's path and down-stream profiles, the state parameters' effects are now investigated in the same manner.

To start with, three values of each of the four state parameters are chosen, and the same approach taken to produce the results of section 3.3 is followed.

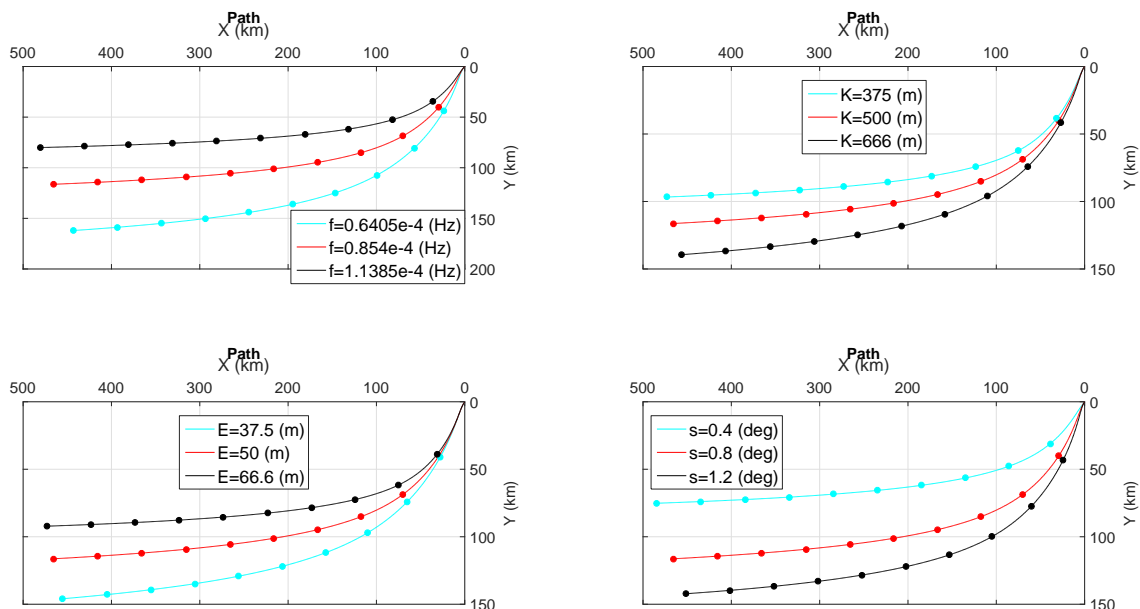


Figure 3.10: Four plots for the paths 12 different currents follow as they move in a homogeneous rotating ambient. The top left panel has three different currents with a varying Coriolis parameter, the top right panel the parameter that is varied is the drag coefficient. In the bottom left panel, the entrainment coefficient is varied. Finally the slope angle is varied to obtain the bottom right panel. The dots represent 50 km intervals along the current path.

Looking at the paths the twelve currents follow in Figure 3.10, it can be seen that a lower Coriolis and entrainment cause the current to travel further down the slope, whereas drag and slope angle act in the opposite manner, as the current would travel further down the slope in the case of increasing the drag or the slope angle. The main difference between changing the state variables in Figure 3.5, and the state parameters here, is that

the currents do not overlap, which indicates the two sets (state parameters and state variables) have different effects on the propagation of the dense currents. The results show that a dense current has one solution for each set of state parameters, and when a state variable is varied, the current tries to readjust to reach that one solution which is controlled by the state parameters.

In order to investigate the physics of changing each of the state parameters, the downstream profiles of the state variables are studied for each case.

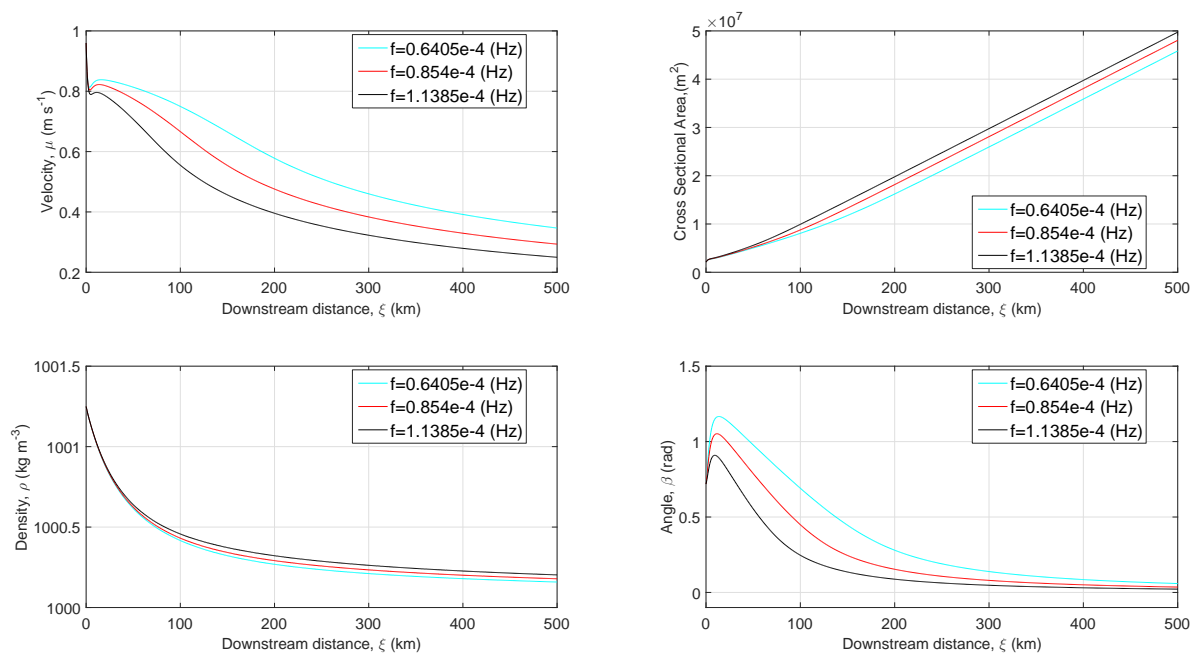


Figure 3.11: Four plots for the state variables' profiles, as a function of the down-stream distance. The Coriolis parameter is the difference between each of the three currents.

Showing the effects that the change of the Coriolis parameter value has on the dynamics of the dense current's down-stream evolution, Figure 3.11 indicates that, for a higher Coriolis parameter, the current would slow down faster. These results can be explained using the balance between the buoyancy and the rotation forces driving the current. As the Coriolis parameter gets larger, rotational forces dominate the current, deflecting it

across the slope. So as the current readjusts near the source, a lower Coriolis value would allow for more acceleration down the slope as can be seen in the top left, and bottom right panels. It follows that a readjustment to a higher velocity causes a smaller cross-sectional area, hence, a lower density anomaly.

Figures 3.12 and 3.13 display results obtained from varying the drag and entrainment coefficients respectively. The results agree with the model equations (Equations (2.118) and (2.121)). As the drag increases, the current velocity would decrease faster, causing the deceleration shown in the top left panel of Figure 3.12 for the black line plot. The decrease in the drag also affects the trajectory of the current, the smoother bottom boundary allows rotational forces to dominate the flow, leading to the current being directed across the slope sooner, as shown in the bottom right panel.

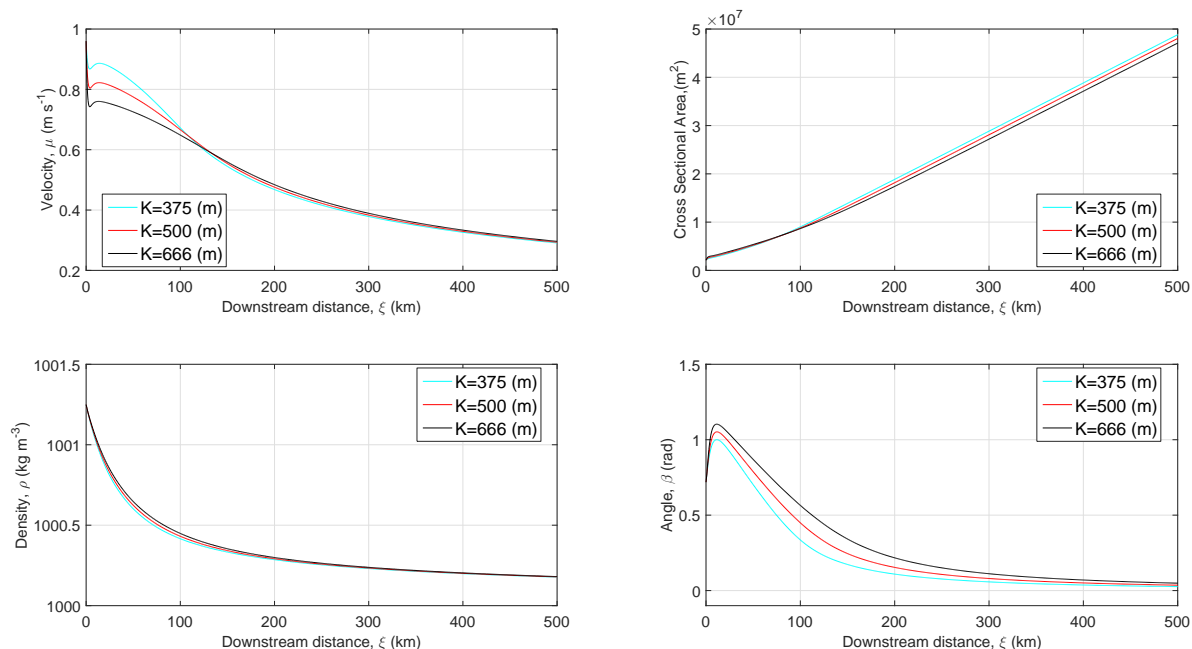


Figure 3.12: Four plots for the state variables' profiles, as a function of the down-stream distance. The drag coefficient is the difference between each of the three currents.

The coefficient of entrainment has the opposite effect to that of the drag coefficient. A

higher entrainment coefficient gives the current a higher cross-sectional area, hence a lower buoyancy force, leading to the current being directed across the slope sooner. It follows that a higher entrainment rate across the interface causes the density anomaly to drop faster as can be seen in the bottom left panel of Figure 3.13.

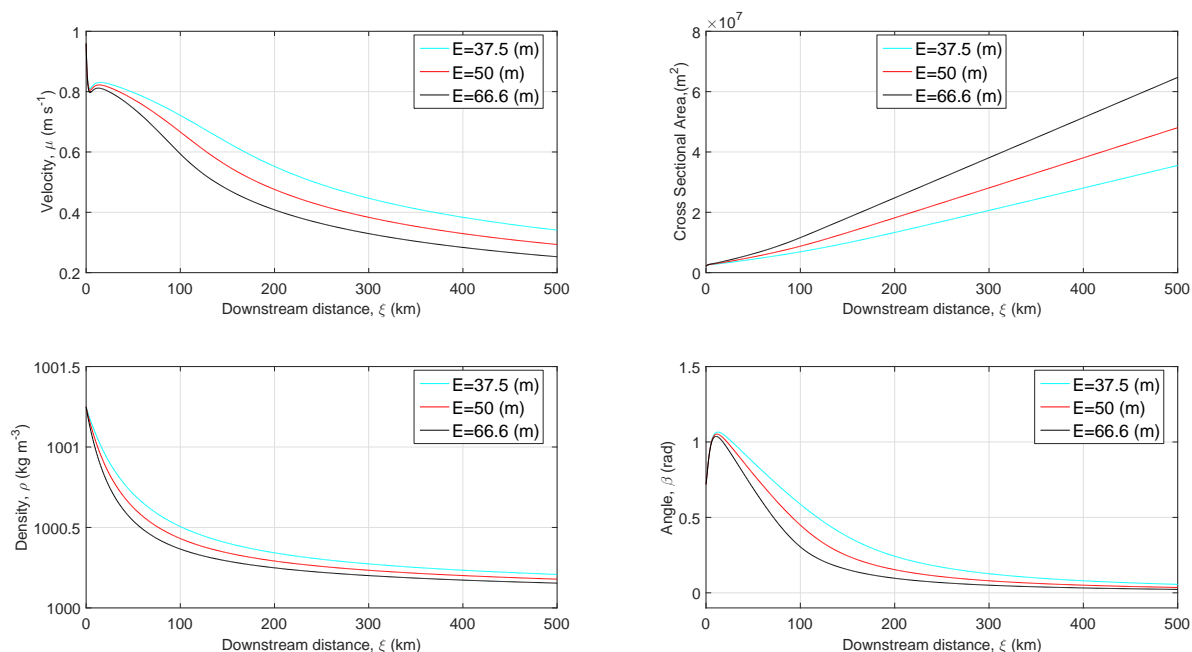


Figure 3.13: Four plots for the state variables' profiles, as a function of the down-stream distance. The entrainment coefficient is the difference between each of the three currents.

The fourth and final state parameter 'slope angle' is varied, and the down-stream state profiles are plotted in Figure 3.14. The base case plotted in red is for the Mediterranean outflow with an angle of  $0.8^\circ$ . This is halved to  $0.4^\circ$  for the current plotted in light blue, and increased to  $1.2^\circ$  for the black plot.

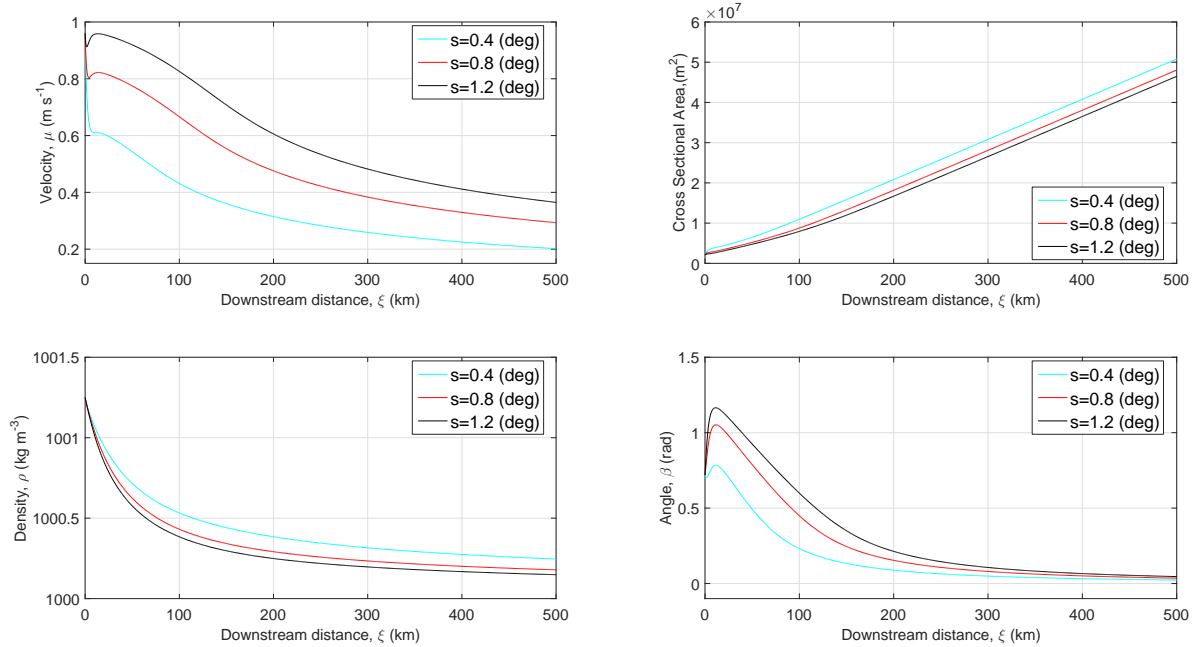


Figure 3.14: Four plots for the state variables' profiles, as a function of the down-stream distance. The slope angle is the difference between each of the three currents.

It can be seen that as the slope angle decreases, the current slows down faster, causing a fast increase in the cross-sectional area near the source. As the currents move downstream, the cross-sectional area increases in a linear fashion across all three slope angle values. Due to the increase of the cross-sectional area, the current density profile decreases less for a smaller slope angle, whereas the inclination profile illustrates that a shallower slope angle would cause the current to travel across the plane sooner than for a steeper slope. This is as Equation 2.121 indicates that as the slope ( $s$ ) gets smaller, Coriolis would dominate the flow.

Cenedese et al. [2004], and Cenedese and Adduce [2008] both showed experimentally that for slope angles ( $s < 0.3$ , i.e.  $16.7^\circ$ ), the current behaved as a laminar density current and very little mixing was observed. However, the mixing dependency was found to be consistent across all slope angle values below 0.3. It was also shown that for slope

angle values ( $0.3 < s < 0.5$ ), the current had a wave region after a laminar region near the source, which increased the mixing. For values of ( $0.5 < s < 1$ ), the waves grew in amplitude and broke in a three-dimensional fashion, further increasing the mixing between the current and the ambient. As the current model does not support wave breaking, it would not be possible to investigate slope angles that would cause the wave breaking regime, whereas for shallower slopes the model is in agreement with the findings of previous studies.

Having tested the four state parameters and their effects on dense steady state currents, it was found that the current behaviour is affected by the Coriolis parameter value, the drag and entrainment coefficients, and the slope angle. For any set of these parameters, the current would readjust near the source to one solution.

# Chapter 4

## Steady state currents and their oscillatory behaviour

Introducing a background density stratification to the ambient fluid can cause dense currents travelling through that ambient to experience oscillatory behaviour. This behaviour comes in form of the current being directed up the slope rather than across it only. The current would then travel back down the slope and so on. The current's path finally levels off and travels across the slope. The effects of the strength of the stratification rate, the value of the Coriolis parameter, and values of the drag and entrainment coefficients effecting these oscillations are now investigated.

### 4.1 The effect of the background ambient stratification

In order to investigate the effect that the change of the ambient background stratification rate strength has on oscillatory behaviour of a steady state current, a set of initial state

variables and state parameters were chosen, and the strength of the stratification rate was varied. The dense current path, along with the state variables' down-stream profiles were investigated for each stratification rate. The ambient density is a function of the distance down the slope. At the source it is always the same and is fixed at  $1000 \text{ kg m}^{-3}$ , whereas the stratification rate is changed for each of the runs (i.e. the deep water gets denser). For consistency, the source conditions of the Mediterranean outflow were chosen to be as shown in Table 3.1, with only the initial pitch angle changed so that the current is directed down the slope. This was done to help eliminate any oscillations in the current path near the source where the current is adjusting to the slope.

It is important here to state the method used by Smith [1975] to define the stratification rate. Smith gave the density anomaly as a function of the down-stream distance to be,  $\Delta\rho = \rho(\xi) - \rho_e(\xi)$ , where  $\rho_e$  is the ambient density and is a function of the down-stream distance  $\xi$ . It is defined as:  $\rho_e(\xi) = \rho_0[1 + sTY(\xi)]$ , where:  $s = \tan \alpha$  is a function of the slope angle  $\alpha$ ,  $T$  is the stratification rate normal to the slope in the ambient region, and  $\rho_0$  is the ambient density at the source.  $T$  has dimensions of  $\text{length}^{-1}$ . As  $T$  approaches 0, or in one of the two cases, if the seabed is flat, (i.e.  $s = 0$ ), or at the source where  $Y = 0$ , then the second term inside the square brackets will approach zero; this gives  $\rho_e = \rho_0$ . For example, the Mediterranean stratification rate given by Smith [1975] is  $T = 1 \times 10^{-6} \text{ m}^{-1}$ . For a slope angle  $\alpha = 0.8^\circ$  that equates to an increase of  $1.43 \times 10^{-5} \text{ kg m}^{-3}$  every 1m in the down slope  $Y$  direction. This study will use  $\frac{\Delta\rho}{\Delta y}$  to define the density stratification. This will help in relating the density stratification to the buoyancy frequency when analysing the oscillatory behaviour of the currents.

Starting with a stratification rate of  $1.43 \times 10^{-5} \text{ kg m}^{-4}$  to match the rate used by Smith [1975] for the Mediterranean outflow for the 1st run, the stratification rate is then decreased to  $0.715 \times 10^{-5} \text{ kg m}^{-4}$  (which represents a 50% decrease from the base case), before being increased to  $2.15 \times 10^{-5} \text{ kg m}^{-4}$  for the 3rd run, which equates to a 50%

increase from the Mediterranean outflow value.

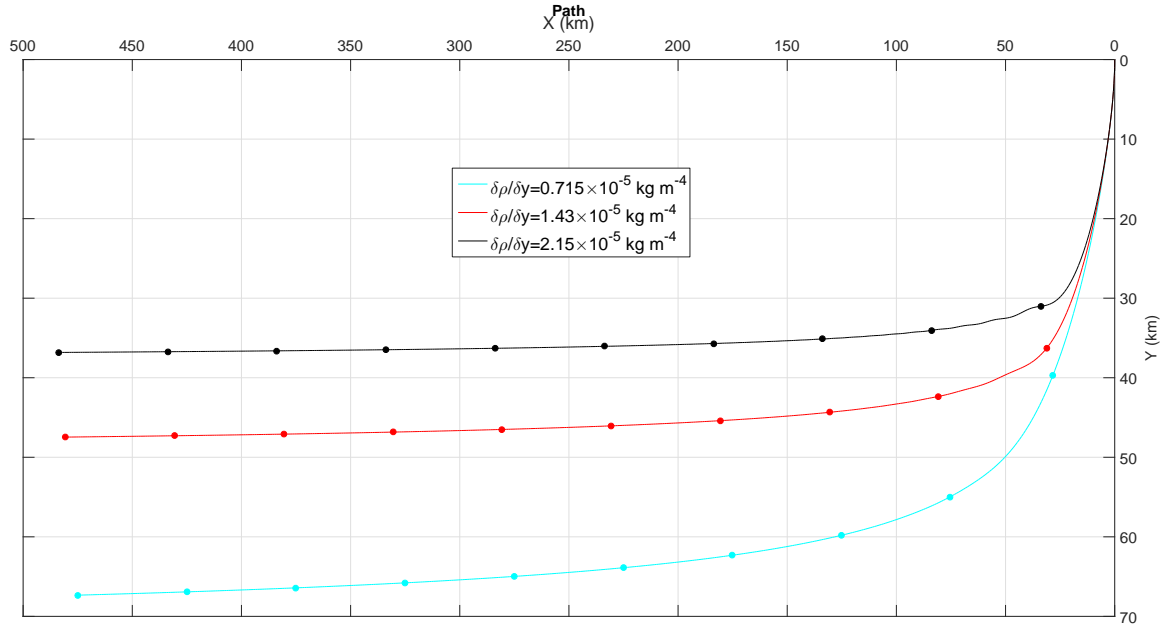


Figure 4.1: Three different stratification rates are used with the source conditions from the Mediterranean outflow for a steady state dense current in a rotating system. The source conditions are: cross-sectional area ( $A_0 = 2.1 \times 10^6 \text{m}^2$ ), velocity ( $\mu_0 = 0.96 \text{ m s}^{-1}$ ), and density ( $\rho_0 = 1001.25 \text{ kg m}^{-3}$ ), giving a density anomaly of  $\delta\rho_0 = 1.25 \text{ kg m}^{-3}$ . In addition to that, the currents' initial pitch angle is  $\pi/2$  rad measured to the positive  $x$  axis, meaning that the current starts being directed down the slope along the  $y$  axis. The three stratification rates as shown in the legend are:  $0.715 \times 10^{-5} \text{ kg m}^{-4}$  for the light blue line,  $1.43 \times 10^{-5} \text{ kg m}^{-4}$  for the red line, and  $2.15 \times 10^{-5} \text{ kg m}^{-4}$  for the black plot. The dots on each of the plots indicate intervals of a 50 km distance along each of the currents' paths.

Figure 4.1 shows the effects that the change of the stratification rate has on the path of a steady dense current in a rotating system. From the results it can be seen that the current path is affected by the rate of ambient stratification. As the stratification rate decreases, the currents are found to travel further down the slope before turning across the slope. In addition to that, the increase of the stratification rate is found to increase the oscillatory behaviour of the current. In order to understand these behaviours, each of the currents' individual state variables are looked at, as a function of the down-stream distance.

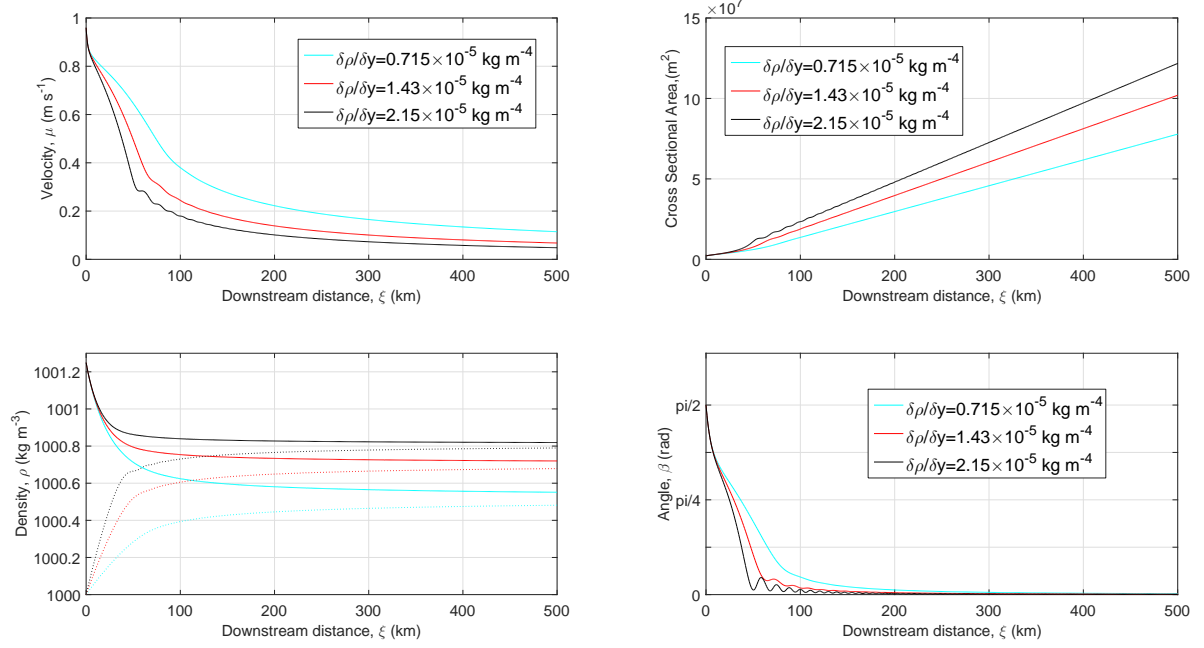


Figure 4.2: Three currents' state variables profiles, plotted against the down-stream distance. The currents are the same in Figure 4.1. The bottom left panel has three additional dotted lines, which represent the ambient density for each of the three currents.

Figure 4.2 shows the state variables as functions of the down-stream distance for the three currents in Figure 4.1. It can be seen that as the stratification rate increases, the current velocity decreases faster; this is due to the decrease in the buoyancy force in the current, which is caused by the current entraining denser fluid from the ambient due to the increase in the stratification rate. The current cross-sectional area is also found to increase more for a higher stratification rate. As the current decelerates, it takes longer to cover the full 500 km distance it is modelled over. It is found that the current travelling through the ambient with the highest stratification rate, plotted in black, takes 1590 hrs to cover the full 500 km distance, in comparison with 706 hrs for the current plotted in light blue, which represents the current in the ambient with the lowest stratification rate. This time difference makes the slower current able to entrain more fluid, even though a higher velocity current would entrain more if the comparison took a Lagrangian approach.

The density plot, in the bottom left panel of Figure 4.2, indicates that the current would approach its neutral density faster as the stratification rate is increased, hence, turning across the slope sooner which can be concluded from the current inclination ( $\beta$ ) plot in the bottom right panel. The important point here is that the currents turn across the slope before reaching their neutral density, meaning that a current will always be in a region of the ambient that has less density than that of the current.

It can also be seen that, as the background ambient stratification rate increases, the dense current experiences more noticeable oscillatory motion, not only in the path the current would follow, but also in the down-stream profiles of the current's state variables. To highlight these oscillations and be able to visualise them more, the first derivatives of the state variables are taken. This is carried out and plotted in Figure 4.3. It can be observed that as the currents travel down-stream, their oscillatory motion experiences an increase of frequency with a decrease in the amplitude.

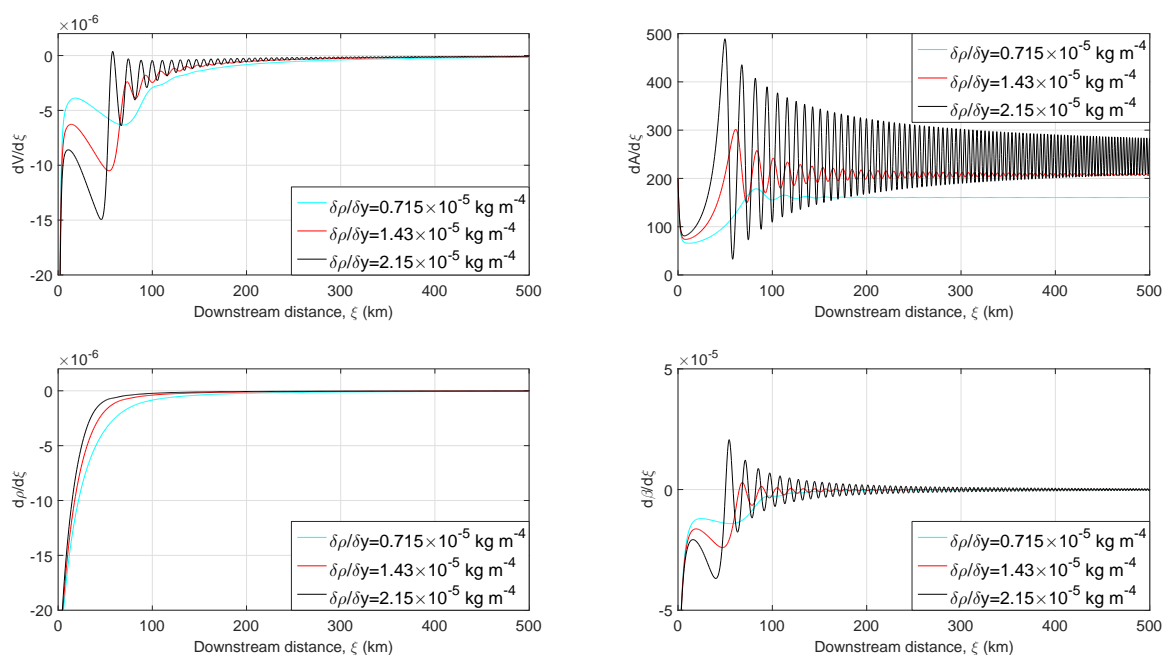


Figure 4.3: The first derivatives, as a function of the down-stream distance, of the state variables in Figure 4.2, plotted against the down-stream distance.

In order to investigate this oscillatory behaviour, the individual terms of the model equations (shown here in the steady state format, with all the terms on the lhs) are plotted.

$$(\mu A)_\xi - E_0 \mu = 0. \quad (4.1)$$

$$(\rho \mu A)_\xi - E_0 \mu \rho_e = 0. \quad (4.2)$$

$$(\rho A \mu^2)_\xi - g A \sin \alpha \Delta \rho \sin \beta + \rho K \mu^2 = 0. \quad (4.3)$$

$$\beta_\xi - \frac{g \sin \alpha \Delta \rho}{\rho \mu^2} \cos \beta + \frac{\hat{f}}{\mu} = 0. \quad (4.4)$$

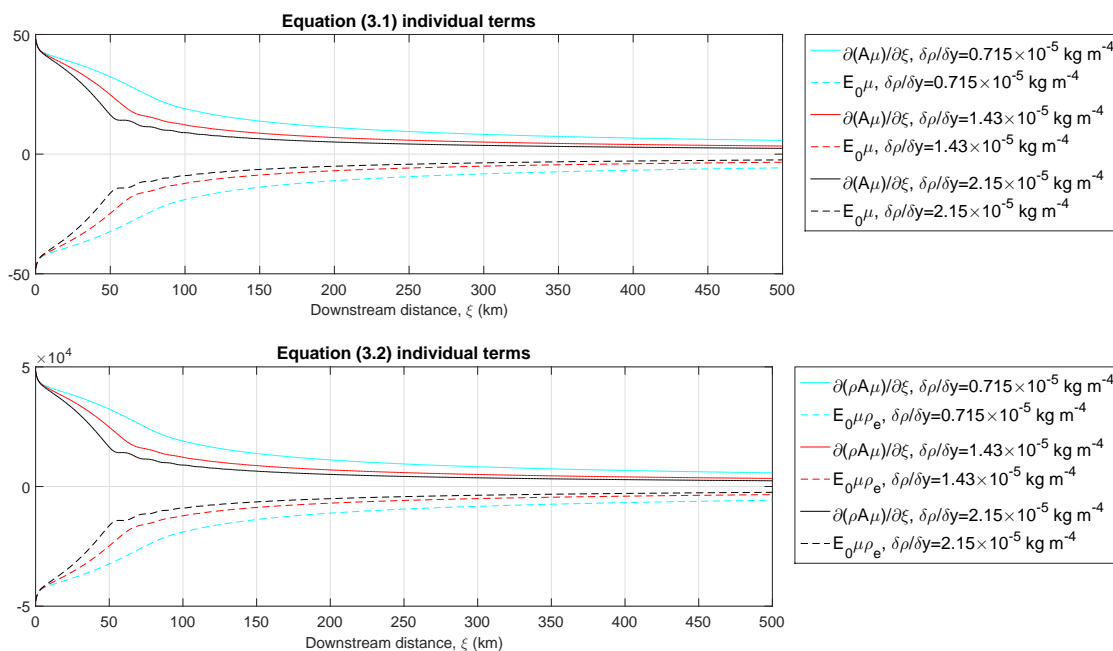


Figure 4.4: Plots for the terms in the 1st and 2nd equations from the steady state system from Smith [1975]. The three colours represent the currents presented in Figure 4.1. The individual terms are plotted against each of the currents' down-stream distances.

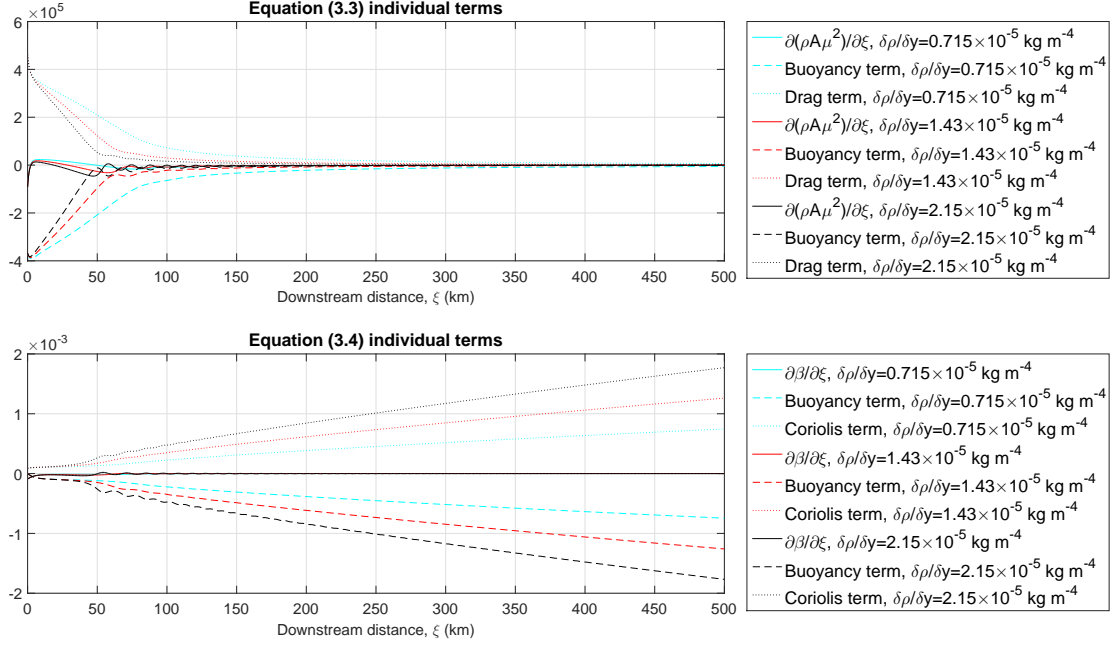


Figure 4.5: Plots for the terms in the 3rd and 4th equations from the steady state system from Smith [1975]. The three colours represent the currents presented in Figure 4.1. The individual terms are plotted against each of the currents' down-stream distances.

Looking at the plots of the individual terms of the equations above, it can be seen that all the terms experience some oscillatory behaviour. It was found that the oscillation starts with the Equation 4.4, specifically with the balance between Coriolis and buoyancy. When the term  $(\hat{f}/\mu)$  becomes smaller than  $(g \sin \alpha \Delta \rho \cos \beta / (\rho \mu^2))$ , at this point the spatial derivative  $(\beta_\xi)$  becomes positive, which in turn directs the current back down the slope, affecting the momentum balance through Equation 4.3. As the current readjusts through a balance between the velocity and cross-sectional area, the inclination derivative changes again as  $\beta$  tends to zero again. This continues with a diminishing amplitude and an increasing frequency. The homogeneous case ( $T = 0 \text{ m}^{-1}$ ) was tested, and it was found out that the term  $(\hat{f}/\mu)$  always remains bigger than  $(g \sin \alpha \Delta \rho \cos \beta / (\rho \mu^2))$  as  $\beta$  tends to zero. It is also noted that all the terms tend to zero, except the buoyancy and Coriolis terms in the 4th equation as they are divided by the velocity which is tending to zero.

Taking the term  $C(\xi)$  as a representation of the buoyancy term, to be  $C = g \sin \alpha \Delta \rho \cos \beta / (\rho \mu)$ , Figure 4.6 shows the relationship between  $C$  and  $f$ , which represents the Coriolis term. It can be seen from the left panel that in the case of the homogeneous ambient,  $C(\xi)$  is asymptotic to  $f$ , whereas this does not stand for a stratified fluid, as demonstrated in the right panel. This oscillation seen in the buoyancy term is the reason that a steady state dense current travelling through a stratified ambient starts experiencing the oscillation behaviour. An in depth investigation is carried out in 4.3 in order to establish where the oscillations come from and if there is a threshold beyond which the oscillations occur.

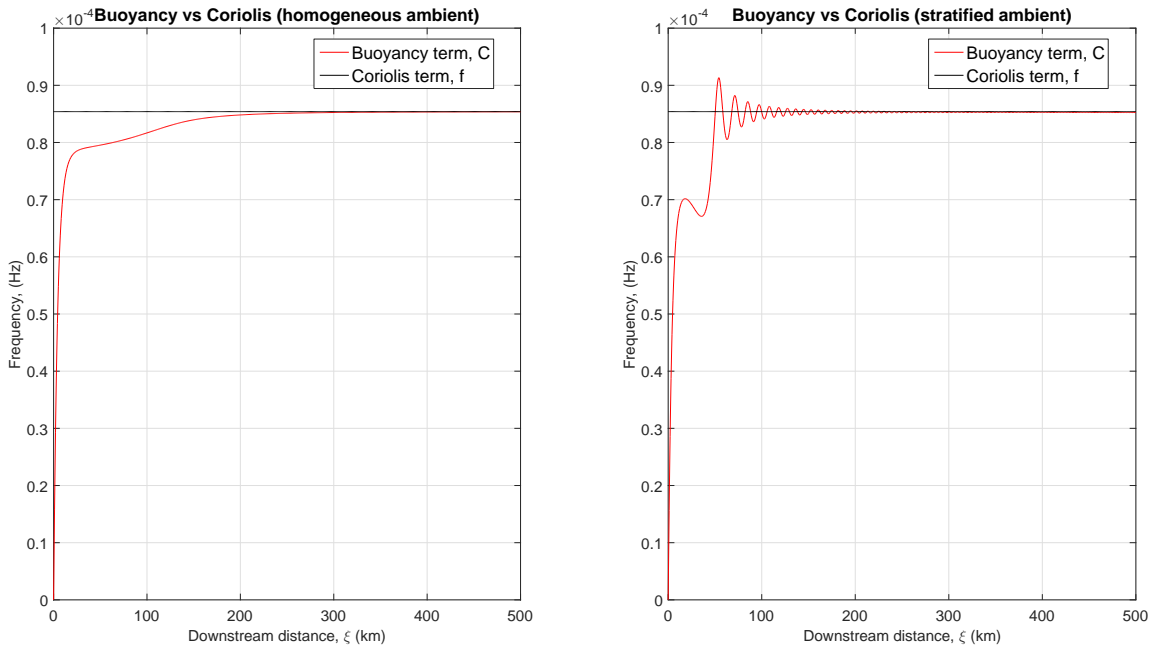


Figure 4.6: Two plots for the the variable  $C$ , plotted against the Coriolis parameter  $f$ . The left panel is for a homogeneous ambient, whereas the right panel is for a stratified fluid, with a density stratification of  $2.15 \times 10^{-5} \text{ kg m}^{-4}$ .

The behaviour of the current oscillation is next examined by changing from a Eulerian representation to a Lagrangian, and then applying a fast Fourier transformation in order to observe the frequencies that the currents oscillate at. The outcome of the Fourier transformations is plotted on the graphs below. The vertical lines labelled with  $(N)$  represent the natural buoyancy frequency of each of the three stratification rates, whereas

the vertical line labelled with ( $f$ ) shows the rotational frequency of the system.

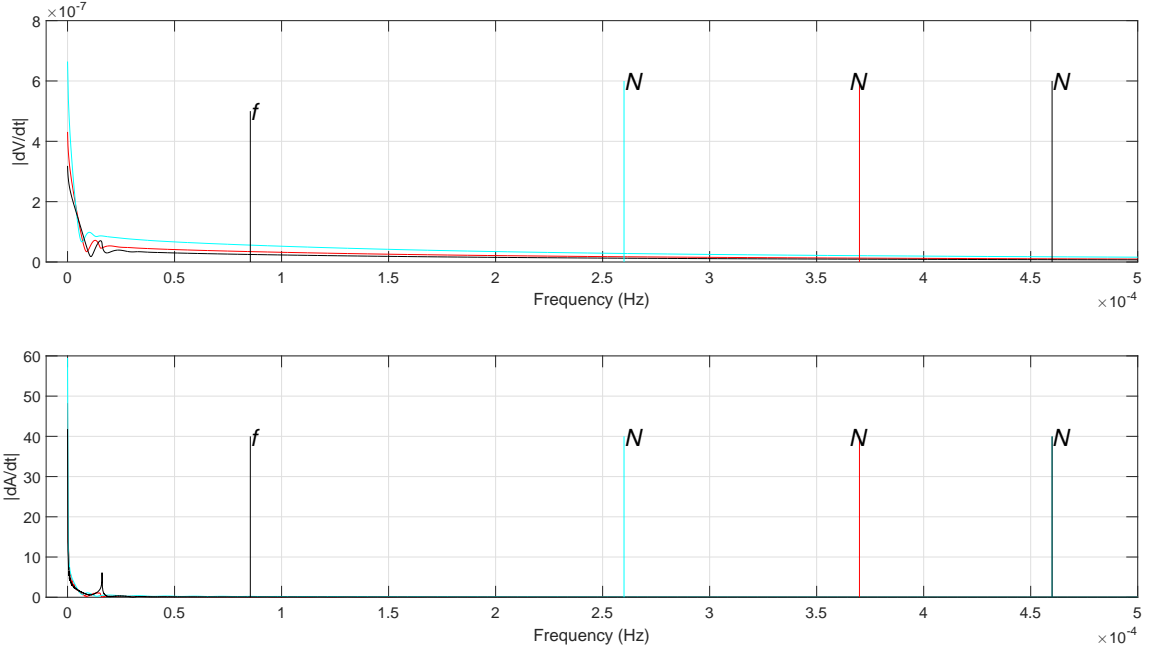


Figure 4.7: A fast Fourier transformation for the oscillations of the currents' velocities and cross-sectional areas.

From Figure 4.7, it is found that the current travelling through the ambient with the weakest stratification rate of  $0.715 \times 10^{-5} \text{ kg m}^{-4}$  has an oscillatory peak in the velocity profiles at  $1.03 \times 10^{-5} \text{ Hz}$ , and  $9.92 \times 10^{-6} \text{ Hz}$  for the cross-sectional area. The ambient with the stratification rate that matches the Mediterranean of  $1.43 \times 10^{-5} \text{ kg m}^{-4}$  caused the current to oscillate at a mode of  $1.30 \times 10^{-5} \text{ Hz}$  in the velocity profiles, and  $1.32 \times 10^{-5} \text{ Hz}$  for the cross-sectional area. The currents travelling through the strongest ambient stratification rate of  $2.15 \times 10^{-5} \text{ kg m}^{-4}$  oscillated at modes of higher frequencies, with the velocity profiles peaking at a frequency of  $1.55 \times 10^{-5} \text{ Hz}$  in the velocity profiles, and  $1.61 \times 10^{-5} \text{ Hz}$  in the cross-sectional area profiles. It can also be noticed that the current travelling through the ambient with the strongest stratification rate had a more defined mode that it peaked at. No peak oscillations were experienced at either the ambients' buoyancy frequencies, or the rotational frequencies of the system.

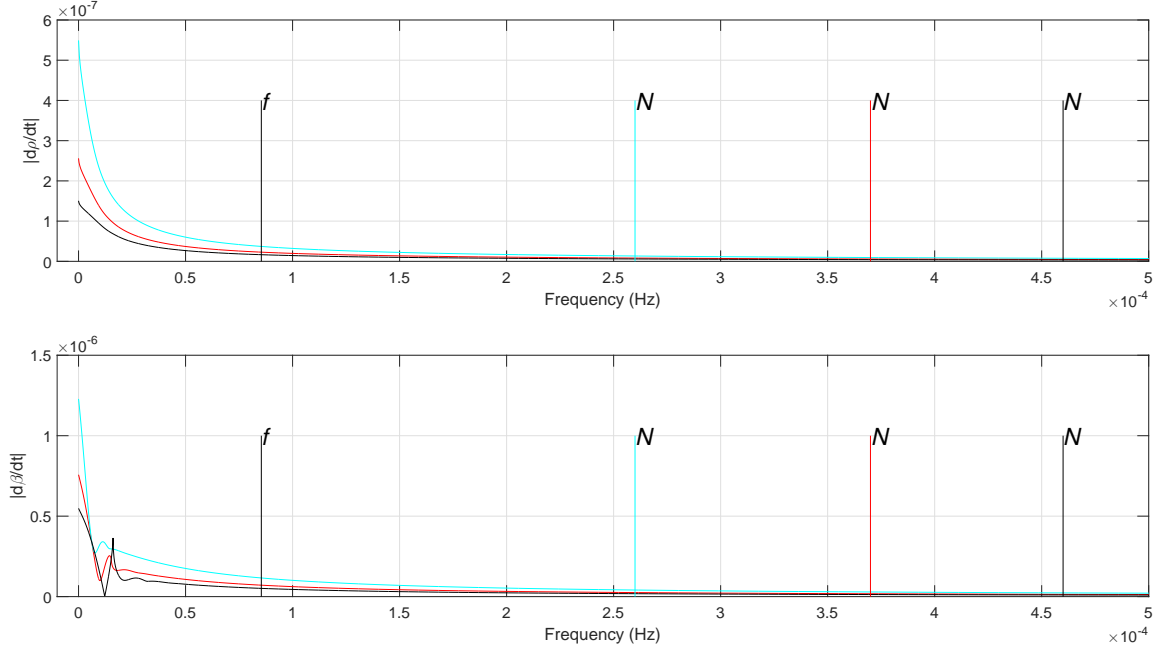


Figure 4.8: A fast Fourier transformation for the oscillations of the currents' densities and inclinations.

Figure 4.8 gives the results of the Fourier transformation for the profiles of the currents' densities and inclinations. The densities' profiles are found not to experience any oscillatory behaviour, as the densities of all three currents are always decreasing with the down-stream distance. The currents' paths do oscillate, and this reflects in the transformation applied to the inclination profiles of the currents. Starting with the current travelling through the ambient with the weakest stratification rate plotted in light blue, it was found to peak at a mode of  $1.14 \times 10^{-5}$  Hz, whereas the current travelling through the Mediterranean system, peaked at a mode of  $1.45 \times 10^{-5}$  Hz, and the strongest stratification rate caused the current's oscillation to peak at a mode of  $1.61 \times 10^{-5}$  Hz. Again, there was no oscillatory behaviour near the buoyancy frequencies of the ambients, nor the rotational frequencies.

From the results, it can be seen that dense currents experience an oscillatory behaviour, in the presence of a background stratification. The oscillation is caused by a balance

between Coriolis and buoyancy as the current turns across the slope, with a decaying amplitude down-stream and an increase in the frequency of the oscillations.

## 4.2 The effects of changing the state parameters

Having investigated the effects that the strength of the background ambient stratification has on the dense current's oscillation, now the effects of changing the state variables on these oscillations are studied. From the four state variables, the slope angle will not be presented; this is because a change in the effect of changing the slope angle is in effect a change in the stratification rate, as the stratification rate is taken along the slope. It was found that an increase in the slope angle affected the current oscillations exactly in the same manner as the increase of the stratification rate.

### 4.2.1 Coriolis

In reality, a rotational rate for a fixed point on the planet is always constant. However, understanding the effects of the different magnitudes of the Coriolis parameter is important in rationalizing the behaviour of these oscillations. In order to do so, three different values for the Coriolis parameter were chosen, the 1st of which was taken from the conditions set by Smith [1975] for the Mediterranean outflow, and had a value of  $0.854 \times 10^{-4}$  Hz. The rotational frequency was then reduced for the 2nd run to a rate of  $0.598 \times 10^{-4}$  Hz, equating to a reduction of 30% from that of the Mediterranean value. For the 3rd run, a value of  $1.708 \times 10^{-4}$  Hz was given; this is double that of the rate used for the 1st run.

In addition to changing the Coriolis parameter, the background ambient stratification rate was set to  $2.15 \times 10^{-5} \text{ kg m}^{-4}$ , which is the highest of the three stratification rates

used in section 4.1. This was done in order to maximise the effect of the stratification rate and increase the internal wave amplitudes.

The same approach used in section 4.1 is applied for the rest of this chapter, where the data is presented as a function of the down-stream distance (Eulerian) in the same way it was presented by Smith [1975]. The data was then changed to a time domain (Lagrangian), before applying the fast Fourier transformation to look into the dominant frequencies in each of the state variables' oscillations.

Figure 4.10 shows the different paths the current would follow from the Mediterranean outflow in the three different cases of the Coriolis parameter values chosen above. A higher Coriolis parameter means that that the current would experience a higher rotational rate, hence, from Equation 2.121, would turn across the slope sooner under the condition that the rest of the parameters and variables remain the same, which is evident in Figure 4.10. What is also clear here is that the oscillations under study have a higher amplitude in the current travelling through the system with the lower Coriolis parameter.

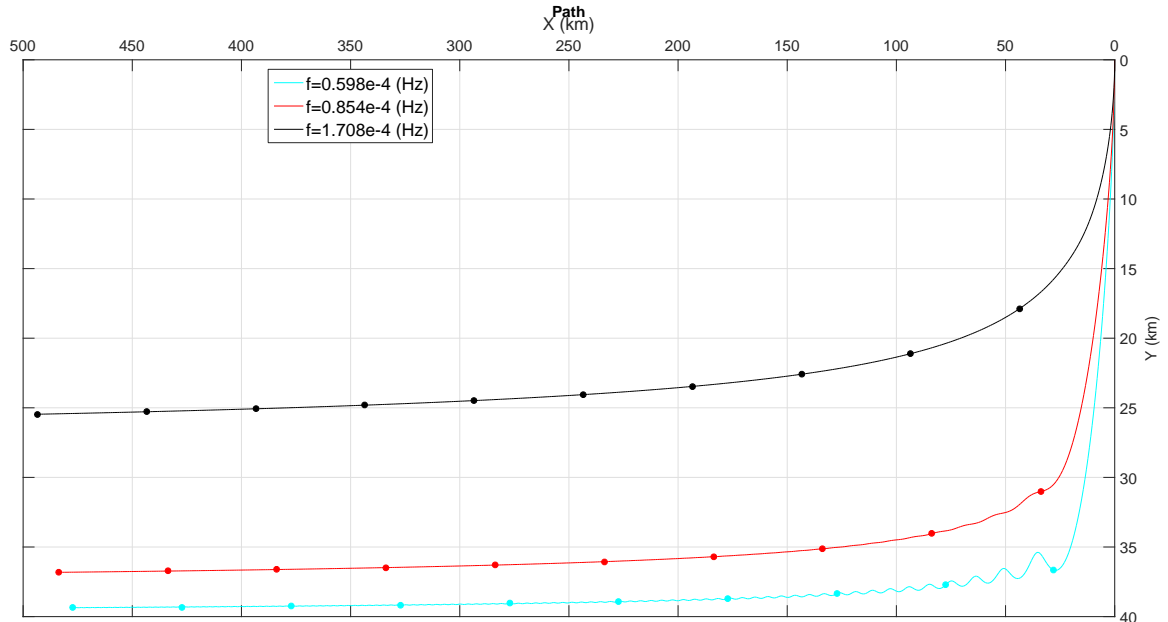


Figure 4.9: Three rotational rates are used with the state variables of the Mediterranean outflow source, in order to model a steady state dense current. The three Coriolis parameters are:  $0.598 \times 10^{-4}$  Hz for the light blue line,  $0.854 \times 10^{-4}$  Hz for the red line, and  $1.708 \times 10^{-4}$  Hz for the black plot. The dots on each of the plots indicate intervals of a 50 km distance along the current's path.

The higher Coriolis parameter of  $1.708 \times 10^{-4}$  Hz does not only dominate the behaviour of the current by causing the current to turn across the slope further up the slope, but also controls the behaviour of the current's oscillatory motion. From the plot of the path, it can be seen that there are no oscillatory motions in the black line which represents the higher Coriolis parameter.

Next the results from applying the fast Fourier transformation to the currents in Figure 4.9 are presented in Figures 4.10 and 4.11.

In each of the four panels, the vertical line plot labelled  $N$  indicates the buoyancy frequency of the ambient fluid, whereas the other three lines indicate the rotational frequencies of the three systems used to test the effects of rotation on the current.

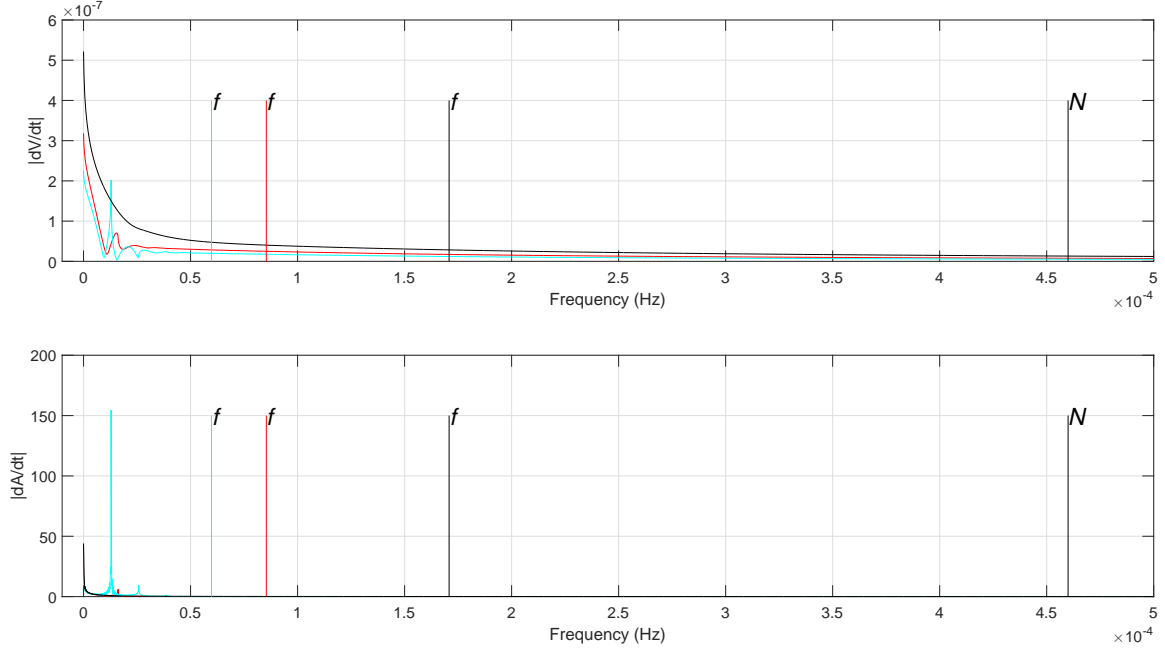


Figure 4.10: A fast Fourier transformation for the oscillations of the currents' velocities and cross-sectional areas.

From analysing the results of the lowest Coriolis parameter,  $0.598 \times 10^{-4}$  Hz, it was found that the current peaks at more than one frequency mode. In the velocity profile oscillation (top panel of Figure 4.10), the current peaked at  $3.82 \times 10^{-5}$  Hz,  $2.82 \times 10^{-5}$  Hz,  $2.07 \times 10^{-5}$  Hz, and  $1.29 \times 10^{-5}$  Hz. Looking at the bottom panel of Figure 4.10, the oscillation of the cross-sectional area of the current, the dominant frequencies were found to be  $2.58 \times 10^{-5}$  Hz, and  $1.29 \times 10^{-5}$  Hz. Looking at the two panels in Figure 4.11, it is found out that first: from the density profile oscillation in the top panel, the same conclusion was reached as to that of changing the stratification rate, that there are no oscillations as the density is always decreasing as a function of the down-stream distance; and the bottom panel shows that for oscillations in the final state variable profile, the path inclination ( $\beta$ ) gave peaks at  $3.90 \times 10^{-5}$  Hz,  $3.11 \times 10^{-5}$  Hz,  $2.58 \times 10^{-5}$  Hz, and  $1.29 \times 10^{-5}$  Hz.

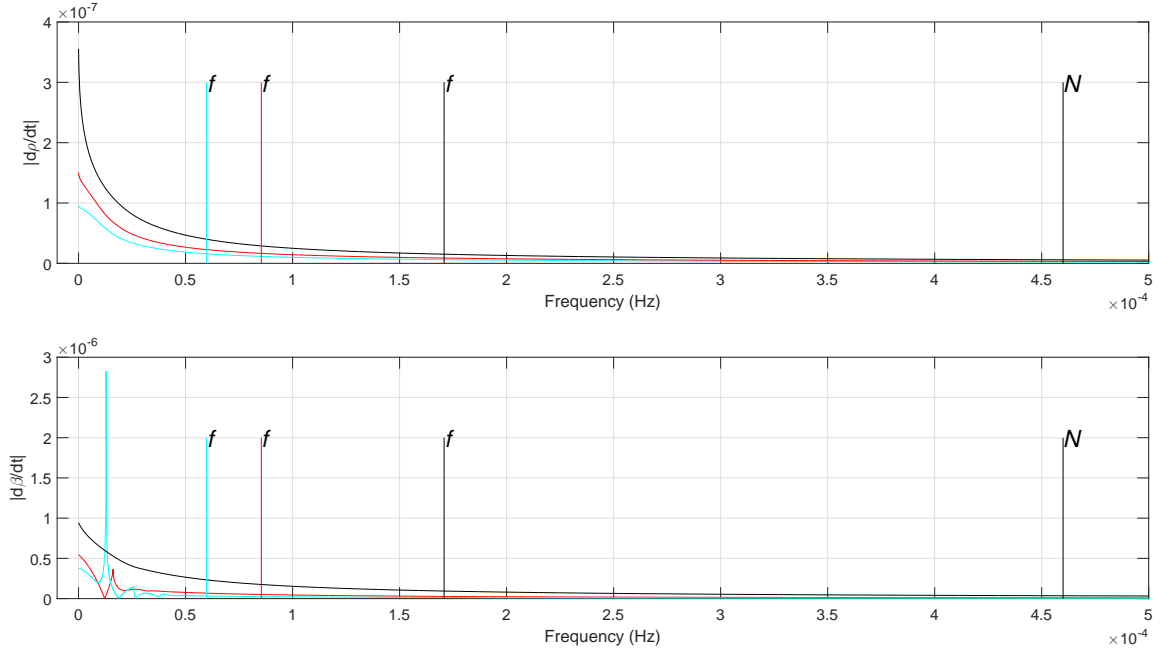


Figure 4.11: A fast Fourier transformation for the oscillations of the currents' densities and inclinations.

Looking at the results for the other two currents, it can be seen that increasing the Coriolis parameter was found to decrease the current oscillation. The current experiencing the highest rotational rate of  $1.708 \times 10^{-4}$  Hz had no oscillations in any of the four state variable profiles.

For the plots in red, relating to the Coriolis parameter of  $0.854 \times 10^{-4}$  Hz, the current velocity profile had two peak modes at,  $1.54 \times 10^{-5}$  Hz, and  $2.38 \times 10^{-5}$  Hz, whereas the cross-sectional area oscillation peaked at  $1.61 \times 10^{-5}$  Hz, which was the same frequency that the current's path inclination oscillation was found to peak at.

From the analysis of the results above, it can be concluded that the Coriolis parameter has an impact on the oscillations that a dense current, travelling through a stratified ambient, would experience. An increase in the rotational rate of the system causes the oscillations to decrease in amplitude, but increase in frequency.

## 4.2.2 Drag coefficient

The effects of the drag coefficient on the oscillation of a dense current are examined next. This is done by changing the the drag coefficient value for three currents, while keeping the rest of the variables and parameters the same.

The three drag coefficients were: 375 m, 500 m, and 666 m, noting that these are the same values used for testing the effect of drag on a dense current in a homogeneous ambient in Section 3.4. Figure 4.12 shows the three different paths that the current follows for three different drag coefficients. It can also be seen that the current travels further down the slope as the drag is increased, which matches with the results presented in Smith [1975].

Looking at the three paths in Figure 4.12, it is clear to see the wave behaviour of the current as it turns across the slope, with the lower drag in the light blue plot experiencing more oscillations.

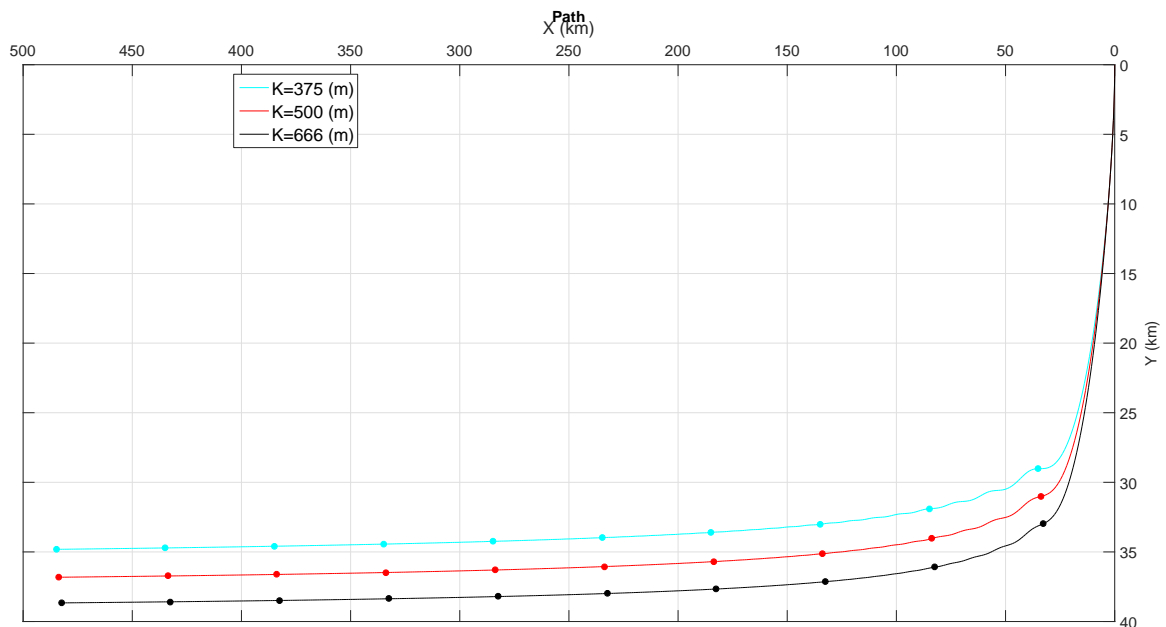


Figure 4.12: Three different drag coefficients are used to test the effects of drag on the oscillations of a dense current. The three drag coefficients as shown in the legend are: 375 m for the light blue line, 500 m for the red line, and 666 m for the black plot. The dots on each of the plots indicate intervals of a 50 km distance along the current's path.

The fast Fourier transformation of the oscillations of the currents in Figure 4.12 is presented in Figures 4.13 and 4.14.

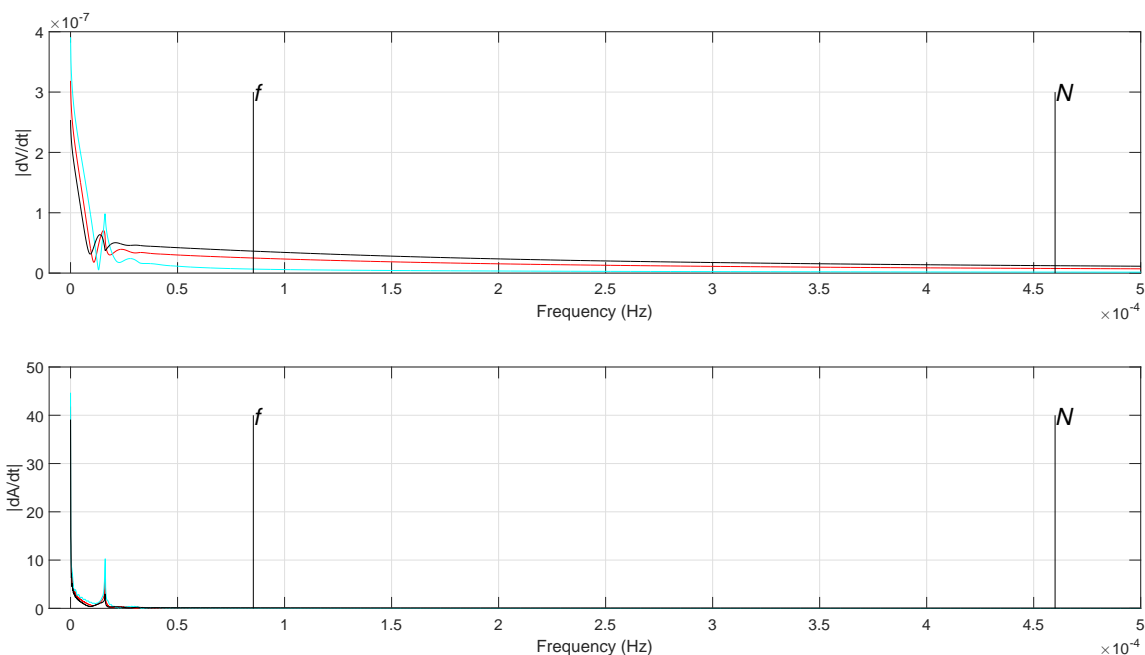


Figure 4.13: A fast Fourier transformation for the oscillations of the currents' velocities and cross-sectional areas.

Looking into the Fourier transformation results, we find out that the currents peak at lower frequencies for higher drag coefficients. Taking the velocity profiles in the top panel of Figure 4.13, it is found that the currents' oscillations peak at  $1.44 \times 10^{-5}$  Hz,  $1.30 \times 10^{-5}$  Hz, and  $1.15 \times 10^{-5}$  Hz for the drag coefficients 375 m, 500 m, and 666 m respectively, whereas from the cross-sectional area profiles, it is found that the current oscillates the most at the following frequencies:  $1.52 \times 10^{-5}$  Hz,  $1.42 \times 10^{-5}$  Hz, and  $1.29 \times 10^{-5}$  Hz. For the  $\beta$  profiles of the currents, the lower drag gives the highest amplitude at  $1.52 \times 10^{-5}$  Hz, the red middle panel plot which uses the coefficient for the Mediterranean outflow of 500 m peaks at a frequency of  $1.45 \times 10^{-5}$  Hz, and the highest drag peaks at  $1.30 \times 10^{-5}$  Hz.

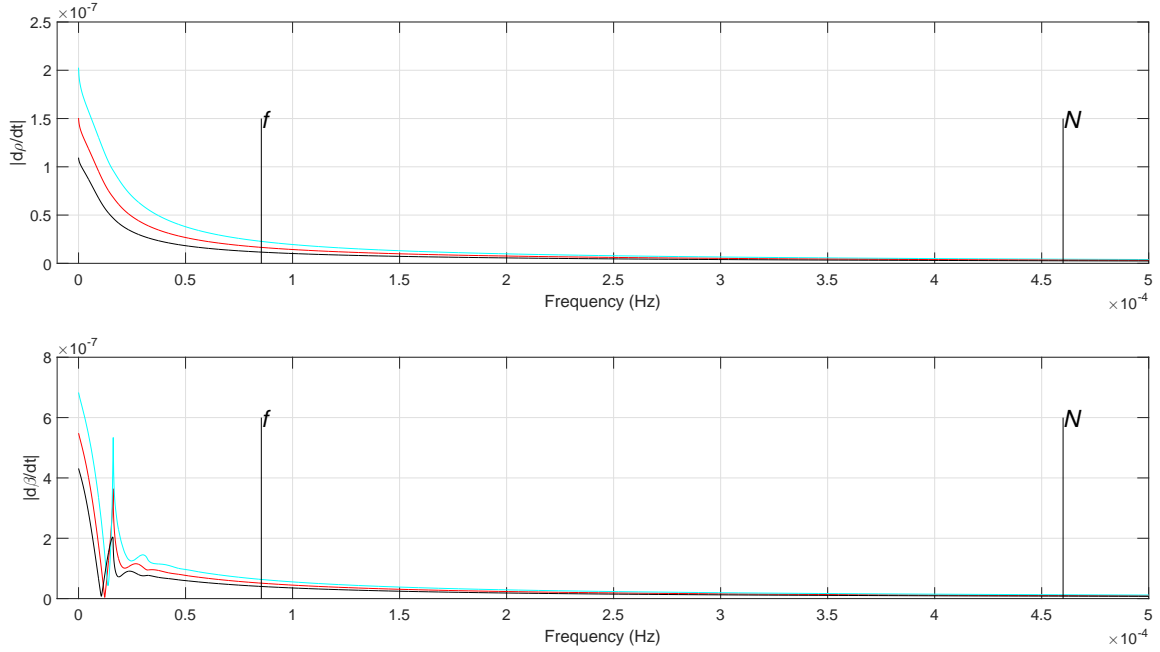


Figure 4.14: A fast Fourier transformation for the oscillations of the currents' densities and inclinations.

From the results of analysing the effects of the drag on the oscillations a dense current, it can be seen that the frequency of these oscillations does not get affected considerably by the change of the drag coefficient. On the other hand, an increase of the drag causes the current to oscillate at higher amplitudes. This result is expected from analysing the moment equation (Equation 2.120).

### 4.2.3 Entrainment coefficient

Finally the affect of changing the entrainment coefficient is considered. Applying the same method used for the previous state variables, the path of the current with different entrainment coefficients is plotted in Figure 4.15. The increase of the entrainment rate causes the current to travel less down the slope due to the decrease in the buoyancy force, which drives the current down the slope. It can be seen that currents experience

oscillation as they turn across the slope and with  $\beta$  tending to zero, as shown in Figure 4.6. The results obtained from the fast Fourier transformation for the oscillation of the state variables of the currents are presented in Figures 4.16 and 4.17.

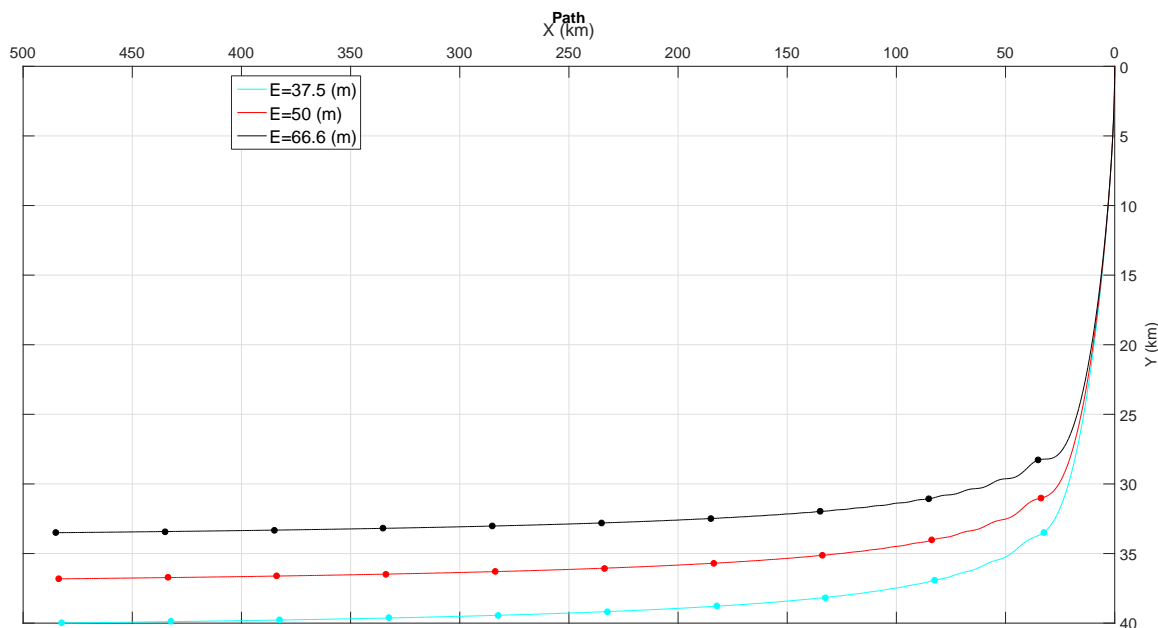


Figure 4.15: Currents' paths, for three currents with different entrainment coefficients. The three entrainment coefficients are: 37.5 m for the light blue line, 50 m for the red line, and 66.6 m for the black plot. The dots on each of the plots indicate intervals of a 500 m distance along the current's path.

From the results, for the entrainment coefficients of 37.5 m, 50 m, and 66.6 m, it is found that the currents' velocity oscillations peak at  $1.22 \times 10^{-5}$  Hz,  $1.28 \times 10^{-5}$  Hz, and  $1.38 \times 10^{-5}$  Hz, while the cross-sectional area profiles peaked at  $1.25 \times 10^{-5}$  Hz,  $1.41 \times 10^{-5}$  Hz, and  $1.52 \times 10^{-5}$ , with the current inclination giving modes at  $1.33 \times 10^{-5}$  Hz,  $1.45 \times 10^{-5}$  Hz, and  $1.52 \times 10^{-5}$ .

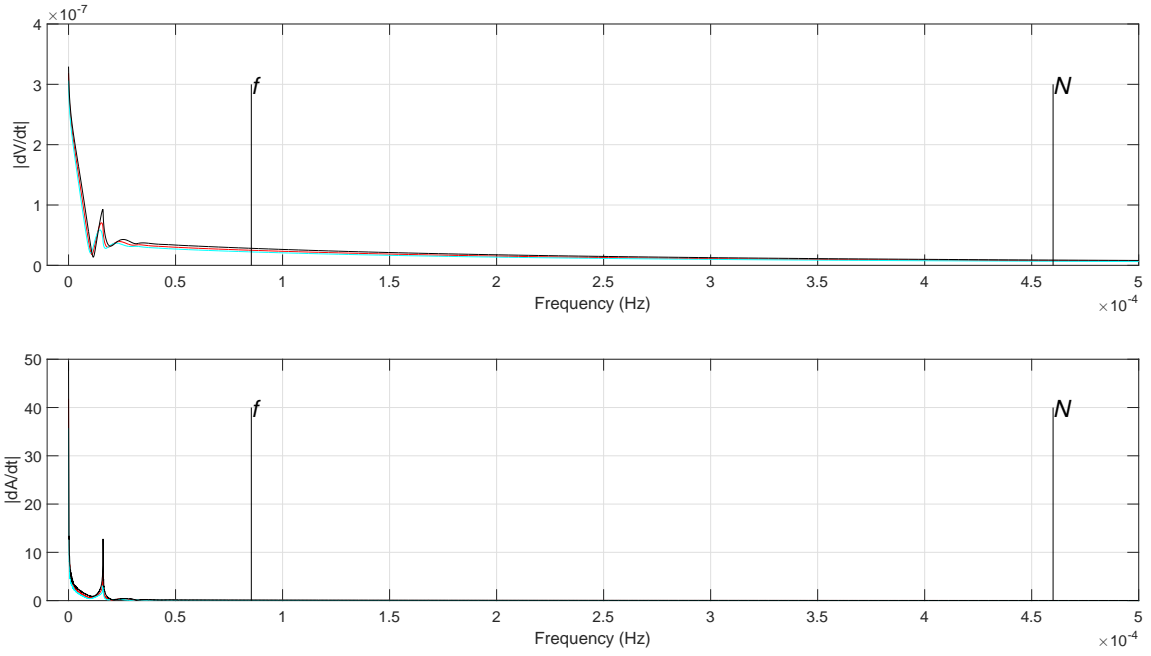


Figure 4.16: A fast Fourier transformation for the oscillations of the currents' velocities and cross-sectional areas.

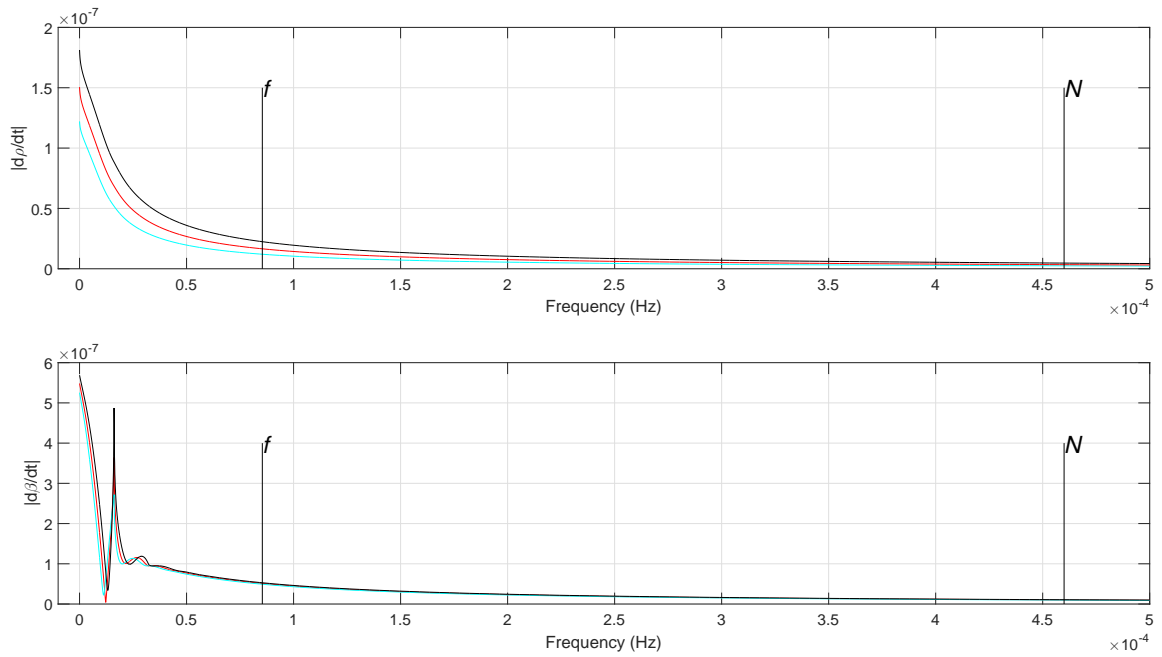


Figure 4.17: A fast Fourier transformation for the oscillations of the currents' densities and inclinations.

The results from varying the entrainment coefficients indicate that the amplitude of the oscillatory behaviour of a dense current flowing through a stratified ambient in a rotating system is affected by the change of the entrainment coefficient of that flow. It was also found that the frequency of the oscillations do not vary considerably with the change of the entrainment.

### **4.3 The limiting cases of the oscillations in the steady state currents**

Having established that a steady state current would experience an oscillatory behaviour under certain conditions, and having identified the parameters that effect these oscillations. This section sets out to establish the limiting states and values beyond which these oscillations occur.

In order to reach the required results, a rigorous numerical analysis was adopted in order to extract data that would aid in predicting this phenomena. To help with this as a first step, a hypothesis was assumed based on the results so far and leading from 4.6. This hypothesis states that “there is a dimensionless quantity that would have a critical value above which a steady state current would experience oscillation while travelling through a rotating ambient fluid”. Based on the results presented obtained from the analysis so far, it was known that the oscillations were effected by the four parameters: Drag, Entrainment, Coriolis and Stratification (buoyancy frequency). It was also found that the oscillations increase in amplitude with the increase of both the stratification of the ambient and the entrainment coefficient of the current. The other finding was that the oscillations diminish as the drag and the Coriolis were increased.

This lead to the following assumption:

$$M_e = \frac{N * E}{f * K},$$

where:  $N$  is the ambient fluid's buoyancy frequency,  $E$  is the current's entrainment coefficient,  $f$  is the Coriolis parameter, and  $K$  is the system's drag coefficient.  $M_e$  was a new constant that was introduced, where a critical value,  $M_{ec}$ , is to be found.

The critical value,  $M_{ec}$ , is when a steady state current with entrainment coefficient  $E$ , travelling through an ambient with a background stratification that has a buoyancy frequency of value  $N$  rotating due to a Coriolis parameter  $f$ , while exerting a drag of  $K$  starts experiencing oscillations.

Leading from the findings that oscillatory behaviour exists when a background stratification is introduced, the numerical system was set up to discover at what values of buoyancy frequency and Coriolis do the oscillations in the steady state current appear. This was repeated for 100 currents with different state parameters and variables. For each current, the stratification rate was increased starting from zero and the required Coriolis parameter to suppress the oscillations was determined numerically. This was continued until the highest Coriolis parameter for a real life situation, a value of  $1.454 \times 10^{-4}$  was reached. For each current fifty pairs of Buoyancy frequency and Coriolis parameter at the boundary between oscillatory behaviour and none oscillatory behaviour were determined. The boundary is shown in Figure 4.18. The orange line and the equation in Figure 4.18 are the approximation of the boundary from the data collected. The approximation is linear as this provided the closest result. The region below the orange line showed no oscillatory behaviour, whereas currents that had a pair of Coriolis parameter and buoyancy frequency values that lie in the upper region above the orange line experienced oscillatory behaviour downstream.

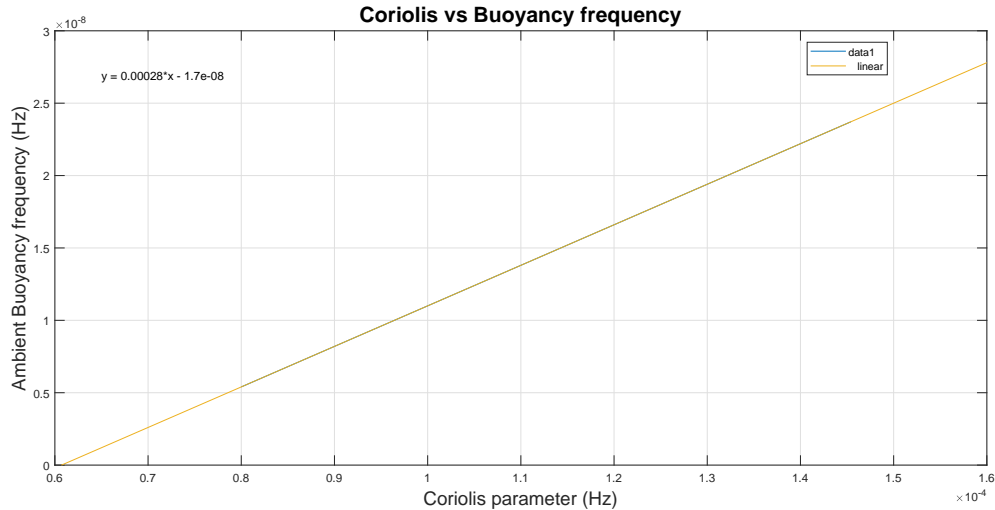


Figure 4.18: A phase diagram for steady state oscillations. The data (in blue) with the linear fitted line (in orange) represent the boundary between oscillations/no oscillations. This graph is an accumulation of 100 tested currents all of length 100 km. A numerical first order explicit marching scheme was used to solve each current with a step size used was 100 m. Random source conditions, drag and entrainment coefficients were chosen for each current, and the values of the Coriolis parameter and ambient buoyancy values of when the steady state current starts to oscillate were recorded.

Moving on from here, 10,000 currents were tested with random ranges of both currents' state variables and state parameters along with the stratification rate of the ambient fluid ensuring that the relationship between the stratification rate and the Coriolis parameter behaviour adhered with the previous finding. The tests were carried out to determine at which values of the individual variables would the specific current experience oscillations. The aim of the numerical method was to test a wide range of current entrainment against system drag. For this to be carried out, the rest of the parameters and variables would be fixed, the entrainment coefficient would be changed till oscillations are detected, at this point the system drag would be increased till the oscillations are suppressed. The numerical values of each were taken to two significant figures, and for each set of current state variables and state parameters, 100 pairs of drag and entrainment coefficients that lie on the boundary of oscillatory behaviour were determined.

Analysis of the results yields a dimensionless quantity of:

$$C_1 = \frac{E}{K},$$

and a critical value of 0.2 was found to control the appearance oscillations as the current travelled down the slope. Currents with  $C_1$  values of above 0.2 would have a current path that would get redirected up the slope downstream before being directed down it again, currents with values of  $C_1$  below the critical limit of 0.2 would turn along the slope approaching a right angle with the downstream direction as an asymptote. Physically, this dimensionless quantity is a measure between how much fluid is being entrained into the current and how much resistance is the current experiencing while moving through the ambient. This is in line with the plots from Smith [1975] where the current with low drag of value 0.1 was found to experience oscillations as it travelled down the slope. This is due to the current having a  $C_1 = 0.5$ . These results also establish that in the absence of the background stratification, a current with a value for  $C_1$  below the threshold would still oscillate as it travelled down the slope.

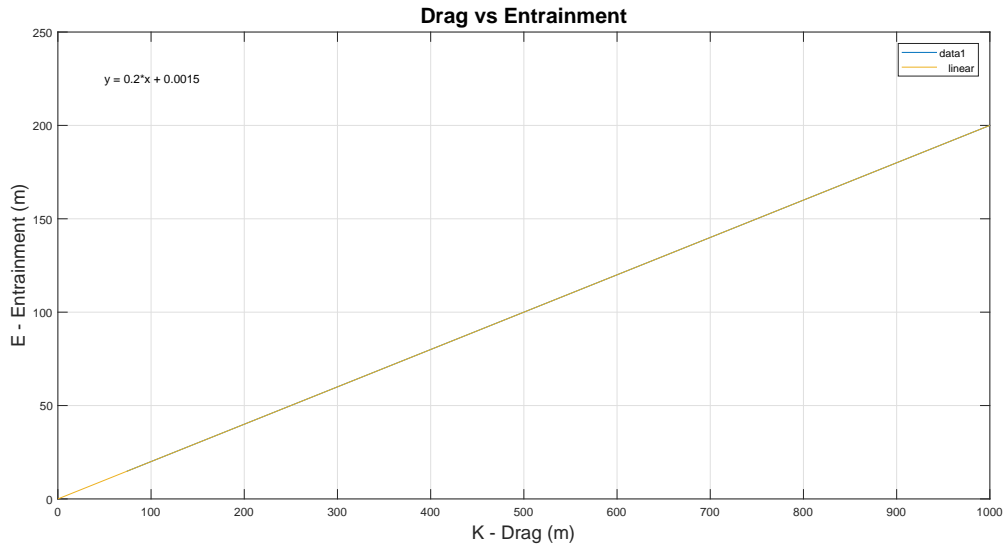


Figure 4.19: A phase diagram for steady state oscillations. The data (in blue) with the linear fitted line (in orange) represent the boundary between oscillations/no oscillations. This graph is an accumulation of 100 tested currents all of length 100 km. A numerical first order explicit marching scheme was used to solve each current with a step size used was 100 m. Here the source conditions were fixed and a random generator was used to vary the Coriolis parameter and the ambient fluid stratification. The entrainment coefficient was then varied from 10 m to 200 m in steps of 2 m, at each step of the entrainment changing, the drag coefficient was varied in order to find the limit at which the current starts to oscillate.

It is important to note that both tests that were carried out in order to determine the threshold where the oscillatory behaviour occurs were implemented on shallow slopes varying from one to ten degrees.

# Chapter 5

## The unsteady model

This chapter covers the results from the newly derived unsteady system in Chapter 2. Having matched the results from the steady case, time dependent perturbations to the source conditions were introduced.

As recent research shows that tidal movements affect the source conditions for the rotating dense currents under investigation [Holland, 2011] through a ‘pulsed source’ effect, or a change in the current’s initial path, the two effects were examined. To begin with, the current’s initial cross-sectional area, velocity, and density were varied, in order to give the pulsed source effect. After that, the current’s initial angle was varied to investigate the effect of changing the current’s path. This will all be carried out for homogeneous ambients initially. The next step examined the effect of changing the background ambient stratification rate on the time-dependent dense current. In addition to that, the effects of changing the rotational rate, drag and entrainment coefficients, along with changes to the amplitude and frequencies of the source oscillations were also investigated.

However, before any results are to be obtained from the new unsteady system, the stability of the new model is addressed. The ill-posedness of the unsteady model developed by

Scase et al. [2006] based on the steady system by Morton et al. [1956], was shown by Scase and Hewitt [2012]. This ill-posedness arises from the rapid growth of linear high-frequency/small-wavelength perturbations, leading to any time-marching numerical method being fundamentally flawed [Holland et al., 2014].

## 5.1 Stability of the unsteady model

Holland et al. [2014] showed that using a theoretical approach, it was possible to prove the well-posedness of the [Holland, 2011]. For this model, theoretical approach was taken similar to that implemented by [Holland et al., 2014]. However, this was unsuccessful due to a dimensional steady solution to being obtained from the Smith [1975] model. The decision was to move to a numerical approach and try to establish a stability of the model. After applying the CFL limitation to the numerical explicit method, the current was oscillated at arbitrary high frequencies and low amplitude. The model was found to be stable and no rapid downstream growth was detected. This approach was carried out on all state variables, and the outcome results show that the model is stable for low amplitude high frequency oscillations.

Here we present three cases for unsteady currents with oscillating source velocity, cross sectional area, and density:

### 5.1.1 Velocity

First to test against the stability of the model is the varying of the source velocity at an arbitrary and low amplitude.

Here the velocity is varied between 0.96022 and 0.95978  $m.s^{-1}$  at a frequency of 6 oscil-

lations per day, or  $6.9444 \times 10^{-5} \text{ Hz}$ . The rest of the state parameters are kept constant and the current's downstream trajectory and the state parameters values as a function of the downstream distance are plotted against the steady state solutions obtained from the limits the velocity was varied between.

The results show a perfect match between the the profiles obtained from the steady state model and the unsteady model.

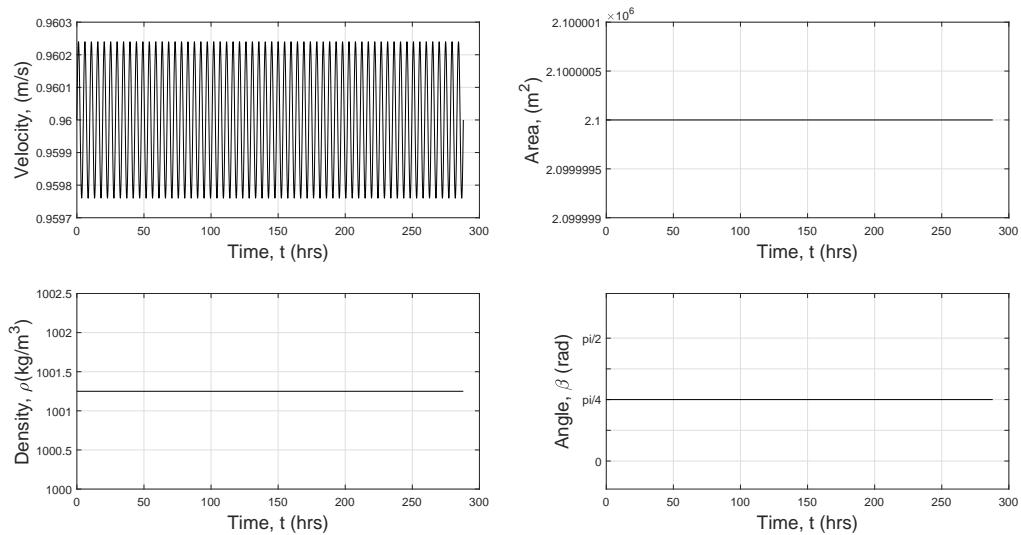


Figure 5.1: The four figures here shows the source conditions used to model a current with the initial velocity experiencing a change over time. The velocity is varied between  $0.96022$  and  $0.95978 \text{ m.s}^{-1}$  at a frequency of  $6.9444 \times 10^{-5} \text{ Hz}$  while the rest of the source conditions are kept constant.

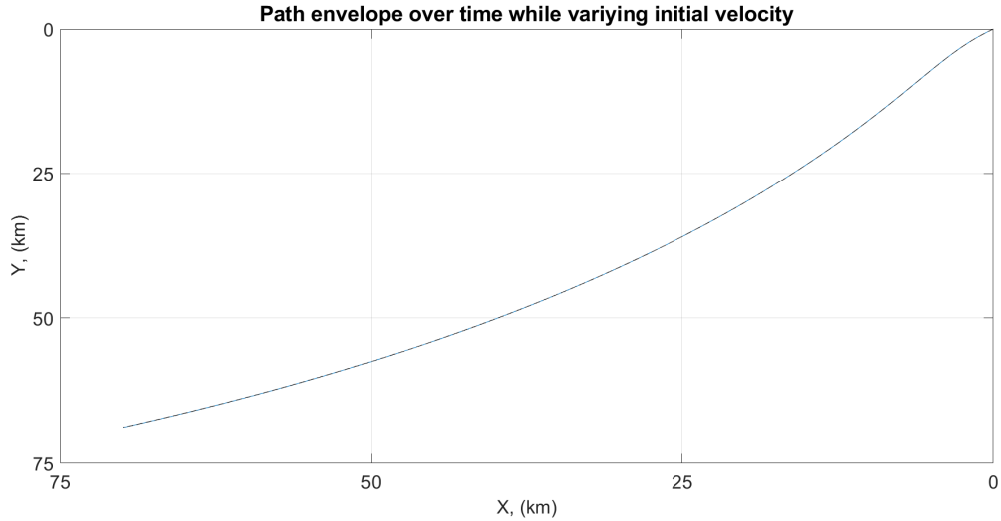


Figure 5.2: This plot shows the downstream propagation of the unsteady current with the varying source velocity. The downstream envelopes are plotted every 2 hours. The result is achieved using an explicit numerical method with a spatial step of 400 m and a temporal step of 200 s giving a CFL number of 0.48 as the initial velocity was taken as  $0.96 \text{ m.s}^{-1}$ .

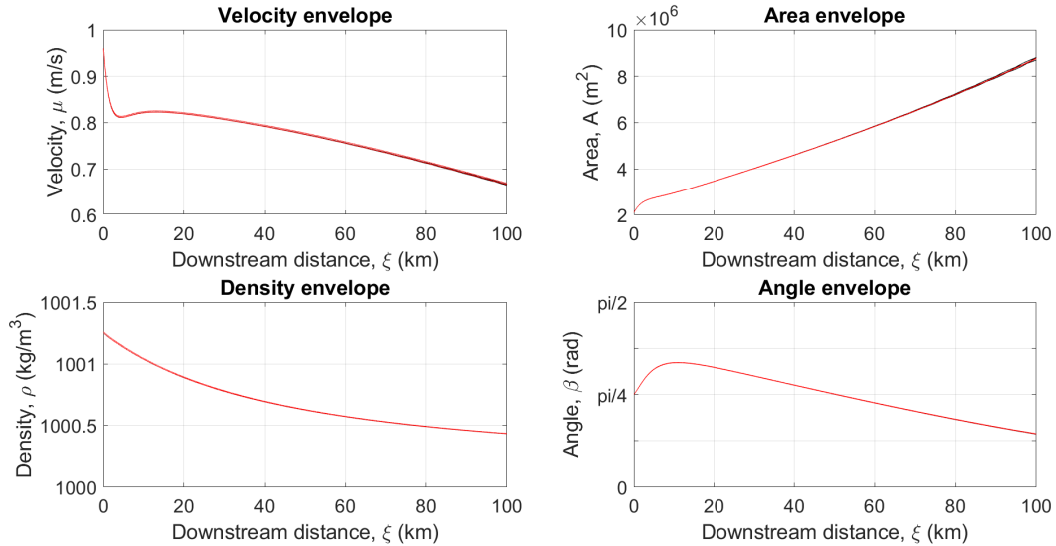


Figure 5.3: Four graphs representing the envelopes of the state variables as a function of the downstream distance. Plotted in red are the two solutions obtained using the two limits which the velocity is varied between. Plotted in black are the downstream envelopes every two hours. The unsteady results were obtained using an explicit numerical method with a spatial step of 400 m and a temporal step of 200 s giving a CFL number of 0.48 as the initial velocity was taken as  $0.96 \text{ m.s}^{-1}$ . The two steady state results in red were obtained using a spatial step size of 400 m.

## 5.1.2 Cross sectional area

Having tested the stability of the model using a high frequency oscillation at the source velocity, the cross sectional area effect is now tested. The frequency is set to 12 oscillations per day,  $1.3889 \times 10^{-4} \text{ Hz}$ , with the limits of the cross sectional area at the source set between 2.0995 and 2.1005  $\text{m}^2$ . The rest of the state variables as source conditions remain constant. The figure below represents the source conditions. From the three figures showing the results below, it can be seen that The current does not experience any “odd” behaviour and that the unsteady results obtained from the new model are within the range predicted by the steady Smith’s (1975) model solved here numerically.

The results for the steady state cases were solved using a marching explicit finite difference numerical method with a step size in the spatial domain of 300  $\text{m}$ . The unsteady results were obtained using a temporal step of 200  $\text{s}$  while the spatial step remained the same as that from the steady state results. This gave a  $CFL$  of 0.64 which is below the critical value of one.

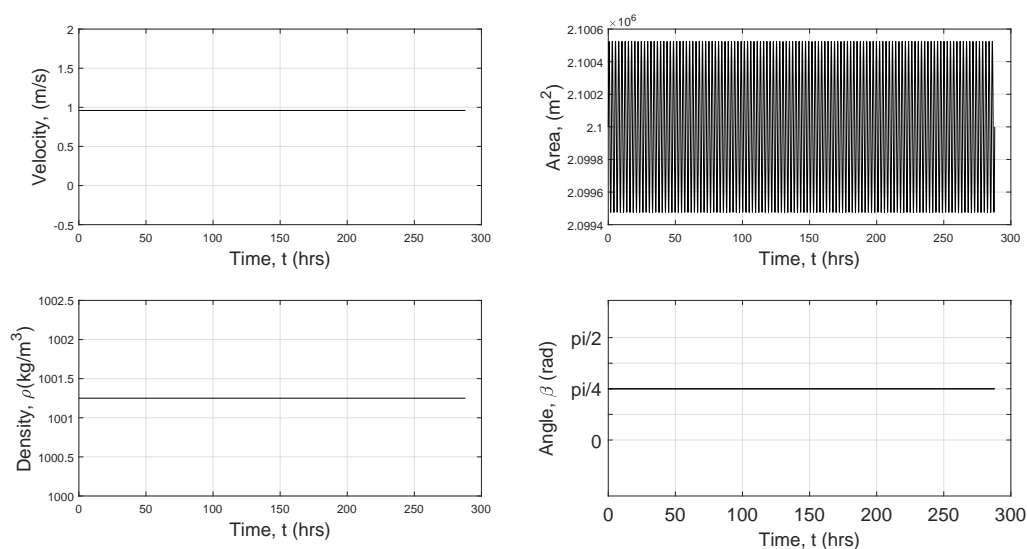


Figure 5.4: The four figures here show the source conditions used to model a current with the initial cross sectional area at the source experiencing a change over time. The cross sectional area is varied between 2.0995 and 2.1005  $\text{m}^2$  at a frequency of  $1.3889 \times 10^{-4} \text{ Hz}$  while the rest of the source conditions are kept constant.

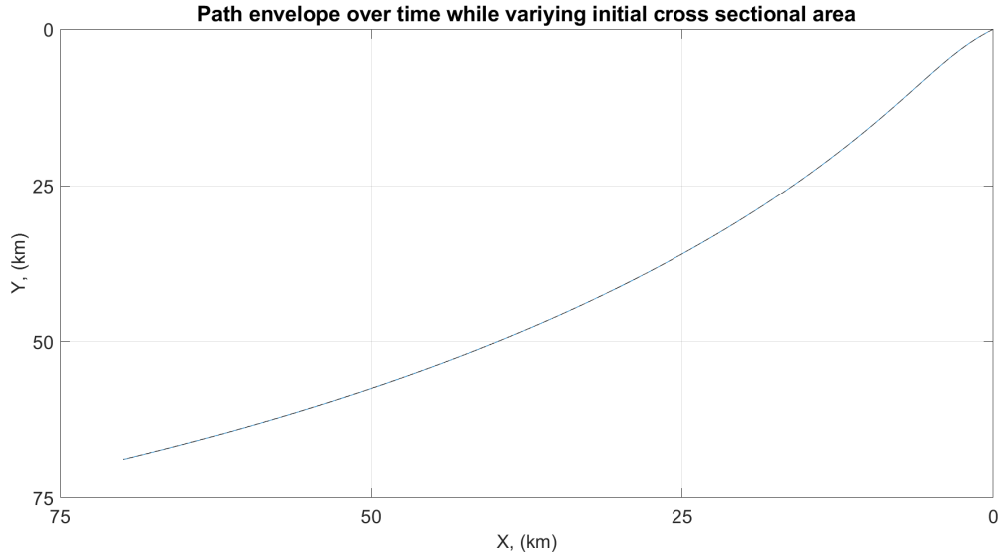


Figure 5.5: This plot shows the downstream propagation of the unsteady current with the varying source cross sectional area. The downstream envelopes are plotted every 2 hours. The result is achieved using an explicit numerical method as explained above.

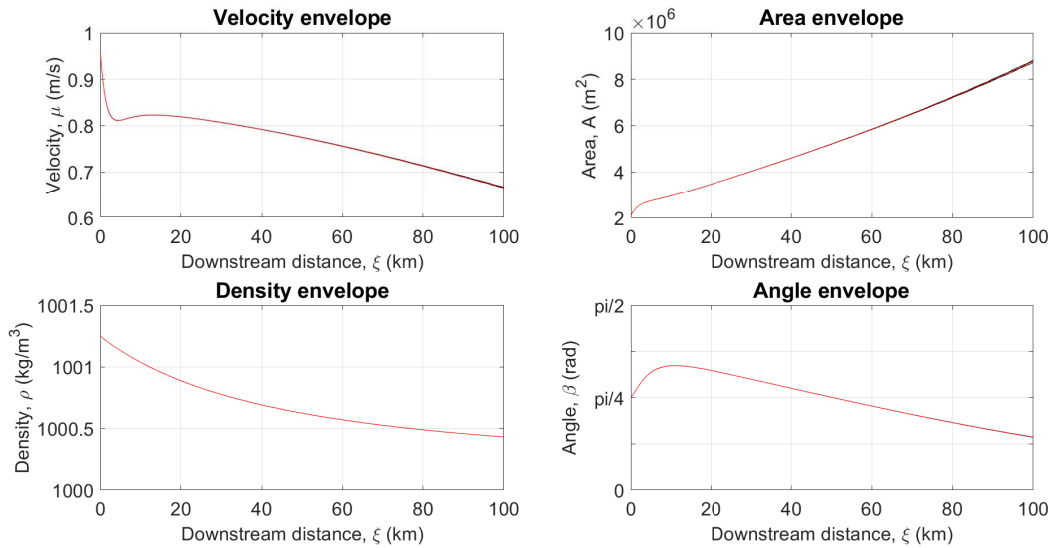


Figure 5.6: Four graphs representing the envelopes of the state variables as a function of the downstream distance. Plotted in red are the two solutions obtained using the two limits which the cross sectional area is varied between. Plotted in black are the downstream envelopes every 2 hours. The unsteady results were obtained using an explicit numerical method with a spatial step of  $300\text{ m}$  and a temporal step of  $200\text{ s}$  giving a CFL number of  $0.64$  as the initial velocity was taken as  $0.96\text{ m}\cdot\text{s}^{-1}$ . The two steady state results in red were obtained using a spatial step size of  $300\text{ m}$ .

### 5.1.3 Density

Having tested the unsteady model stability against initial source conditions for both velocity and cross sectional area, the density difference at the source is now used as the final step for the measurement of the model stability. In order to carry out this test, the current density at the source is varied between  $1001.2495 \text{ kg.m}^{-3}$  and  $1001.2505 \text{ kg.m}^{-3}$ , while the ambient fluid density is kept constant at  $1000 \text{ kg.m}^3$ . The variation is carried out over a time that allows for 10 cycles per day, giving a frequency of  $1.1574 \times 10^{-4}$ .

Here the envelope of the current path is plotted in the figure below. The current downstream propagation is plotted every 2 hours over a total time of 280 hours.

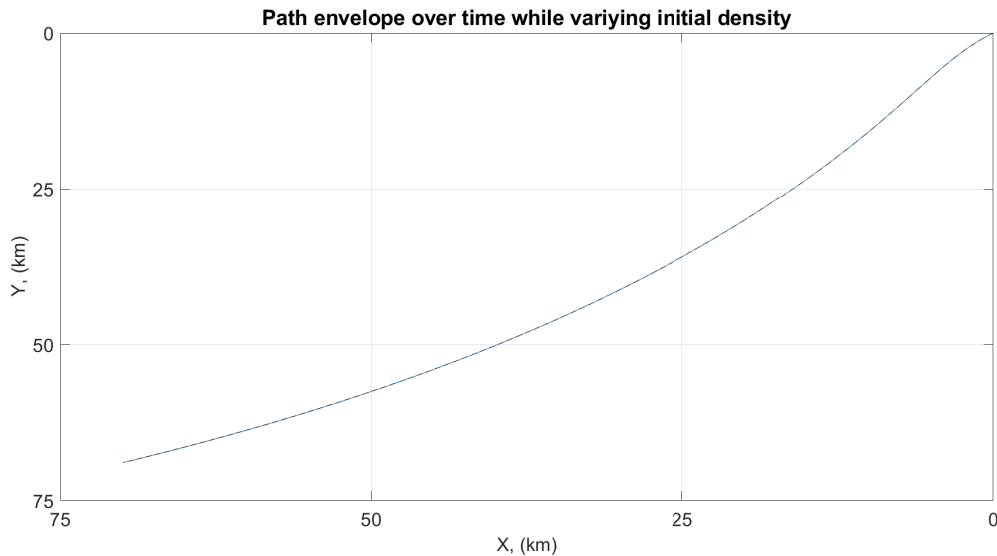


Figure 5.7: A figure showing the downstream propagation of the unsteady current with the varying density. The downstream envelopes are plotted every 2 hours. The result is achieved using an explicit numerical method. The temporal step step is taken to be  $200 \text{ s}$  where the spatial step for the computation is taken at  $300 \text{ m}$ , which gives a CFL of 0.64.

The results from the stability check using the variation of the initial source density show that the results from the unsteady model are in line with the results that are obtained from the steady state model.

## 5.2 The effect of a pulsing source

In order to create the pulsed source effect, the initial conditions of the current's velocity, cross-sectional area, and density are varied over time. Each test run will have one of the three variables varied only.

For all three tests the following conditions were used: the initial state variables were  $\mu_0 = 0.96 \text{ m s}^{-1}$ ,  $A_0 = 2.1 \times 10^6 \text{ m}^2$ ,  $\rho_0 = 1001.25 \text{ kg m}^{-3}$ , and  $\beta_0 = \pi/4$ , the rotational rate was set to  $f = 0.854 \times 10^{-4} \text{ Hz}$ , the slope angle was  $\alpha = 0.8^\circ$ , the ambient was homogeneous with a density of  $\rho_e = 1000 \text{ kg m}^{-3}$ , gravitational acceleration was  $g = 9.81 \text{ m s}^{-2}$ , and the drag and entrainment coefficients were  $K = 500 \text{ m}$ , and  $E = 50 \text{ m}$  respectively.

Each of the three variables' (velocity, cross-sectional area, and density) initial values were oscillated individually then. For example, Figure 5.8 gives the source conditions for a current experiencing a variation in the value of the initial velocity. Here the initial velocity is  $0.96 \text{ m s}^{-1}$ , and is then varied between  $0.88 \text{ m s}^{-1}$ , and  $1.04 \text{ m s}^{-1}$ , over a period of 24 hrs. It can be seen that the rest of the source conditions do not change over time.

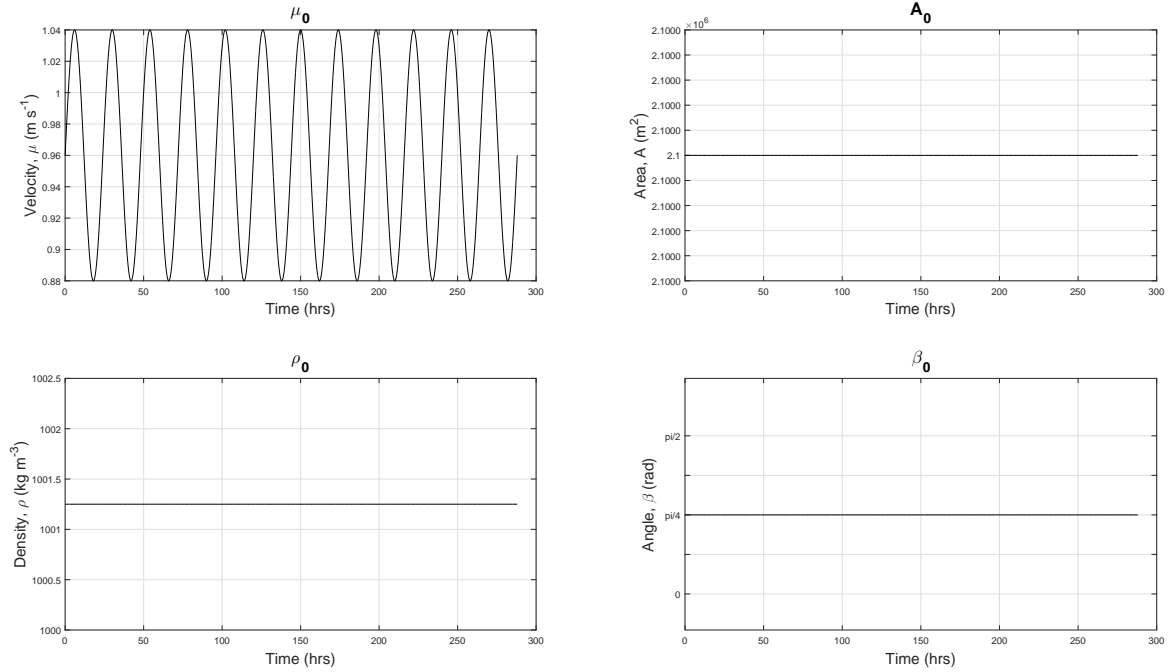


Figure 5.8: An example for the source conditions that a time-dependent dense current could experience. Here the current's initial velocity is oscillated between  $0.88 \text{ m s}^{-1}$  and  $1.04 \text{ m s}^{-1}$ , and the rest of the state variables remain the same with a cross-sectional area  $A_0 = 2.1 \times 10^6 \text{ m}^2$ , a density  $\rho_0 = 1001.25 \text{ kg m}^{-3}$ , and an inclination  $\beta_0 = \pi/4$ .

The same method was used for the oscillation of the initial cross-sectional area and density.

Here the results could be presented in two different manners. The first option would be to plot the graphs as functions of the current's state variables and compare those to the steady state results produced using the limitations of the oscillations. The second option would be to plot the downstream evolution of the linearised harmonic perturbations. As the focus of this research is to compare the effect of the unsteadiness of the source on the downstream current's state variables, the first option is used here to present the findings. However, Figure 5.9 shows an example of a downstream evolution of the linearised harmonic perturbations system for the source conditions presented in Equation 5.1.

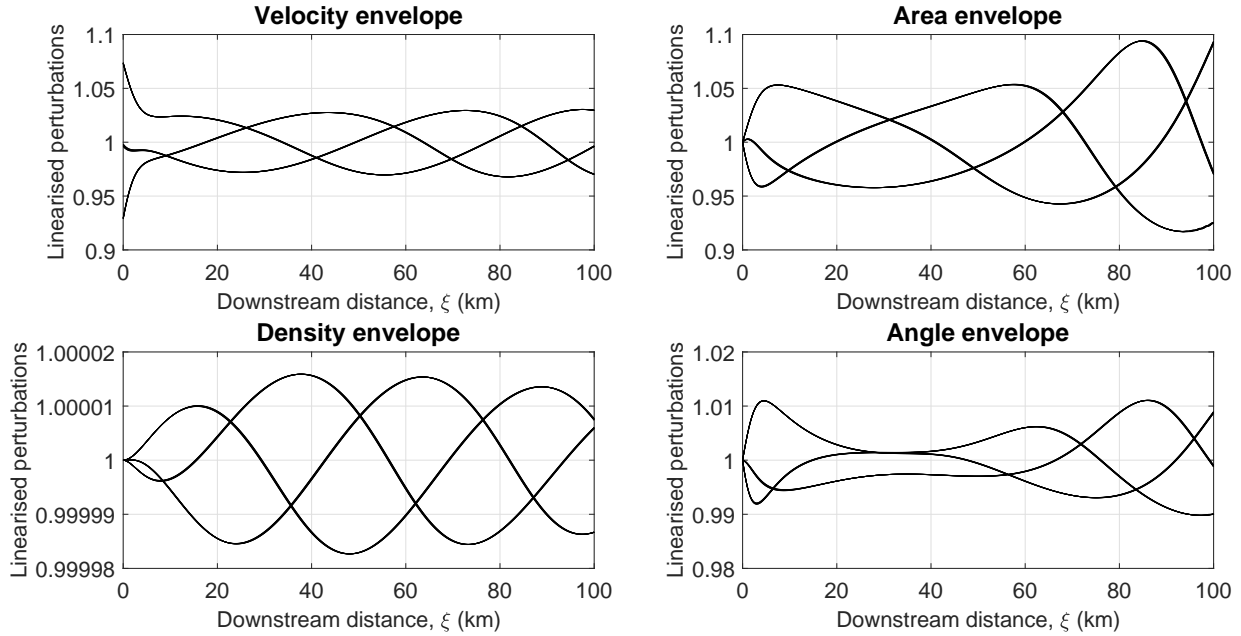


Figure 5.9: An example for the downstream evolution of the linearised harmonic perturbations of the current for the source conditions shown in Equation 5.1.

### 5.2.1 Varying the initial velocity

The first variable to be oscillated is the velocity. Here the source conditions shown in Figure 5.8 are applied, and the down-stream profiles of the current's state variables are presented in Figure 5.10. The black lines show the solution from the time-dependent model, where profiles are plotted every 4 hours. The red lines are steady state solutions for three source velocities. Here those values are  $0.88 \text{ m s}^{-1}$   $1.04 \text{ m s}^{-1}$ , which represent the the two values that the initial velocity is oscillated between, and  $0.96 \text{ m s}^{-1}$ , the base value which the current source started at.

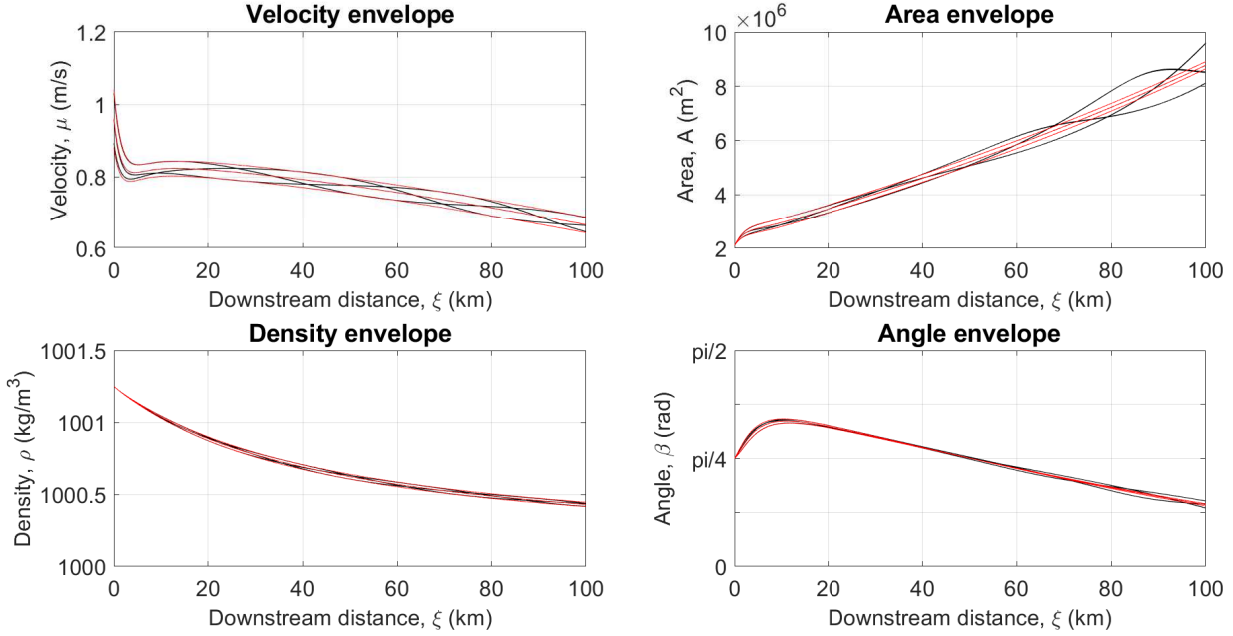


Figure 5.10: Down-stream envelopes of the four state variables for a time-dependent dense current in a rotating system. The initial velocity is oscillated between  $0.88 \text{ m s}^{-1}$  and  $1.04 \text{ m s}^{-1}$  over a period of 24 hours. The black lines represent the down-stream profiles and are plotted every four hours. The red lines are the steady state solutions using initial velocity values of  $0.88 \text{ m s}^{-1}$ ,  $0.96 \text{ m s}^{-1}$ , and  $1.04 \text{ m s}^{-1}$ .

Figure 5.10 shows that the current down-stream profiles change over time, with the current velocity and density remaining within the ‘limiting’ steady state solutions. However, the current cross-sectional area and inclination are not bound by the solutions from the steady state sources, and an increasing ‘overshooting’ in the cross-sectional area with the down-stream distance can also be noticed.

## 5.2.2 Varying initial cross-sectional area

The same oscillation period of 24 hours is used for testing the effects of the oscillation of the cross-sectional area, as well as the density. Here in the cross-sectional area test, the initial value of  $2.1 \times 10^6 \text{ m}^2$  is decreased to  $1.925 \times 10^6 \text{ m}^2$  and then further increased to  $2.275 \times 10^6 \text{ m}^2$  over the oscillation period of 24 hours. The down-stream profiles of the

state variables are plotted every 4 hours, in addition to the steady state results produced using the three values of the cross-sectional area mentioned above, and the results are plotted in Figure 5.11. It can be seen from the results that the current's cross-sectional area profiles are not bound by the results obtained from the steady state results from the limits of the oscillations. The response of the current to the oscillation in the initial cross sectional-area at the source is similar to that of the oscillation in the initial velocity at the source.

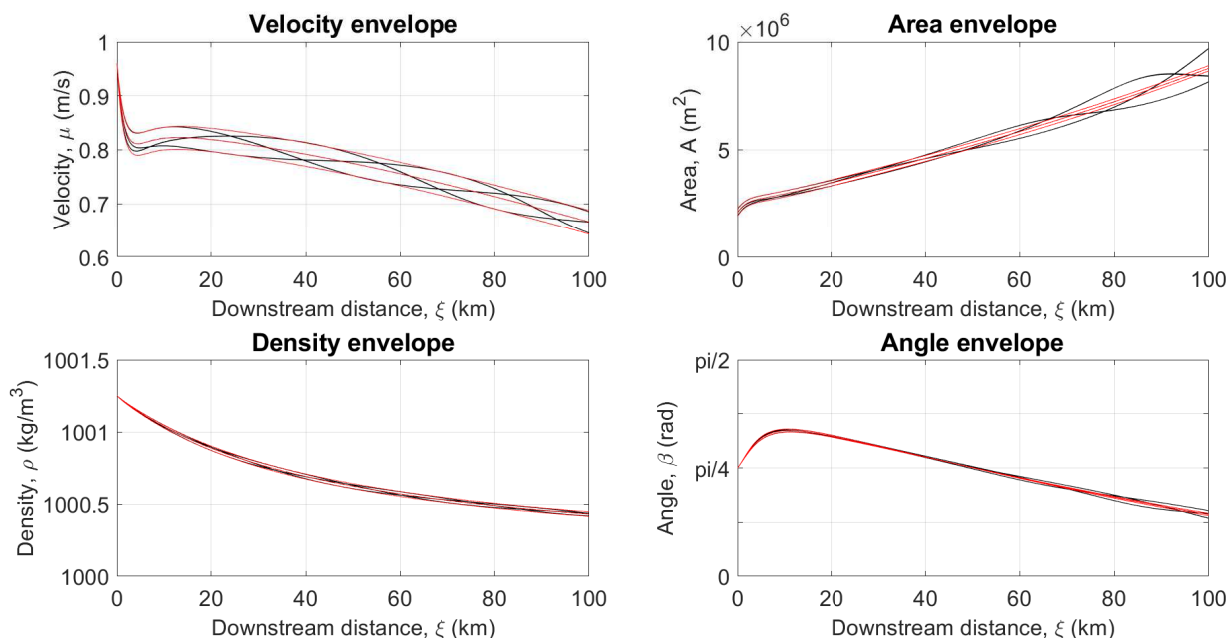


Figure 5.11: Down-stream envelopes of the four state variables for a time-dependent dense current in a rotating system. The initial cross-sectional area is oscillated between  $1.925 \text{ m}^2$  and  $2.275 \text{ m}^2$  over a period of 24 hours. The black lines represent the down-stream profiles and are plotted at four hour intervals. The red lines are the steady state solutions using initial cross-sectional area values of  $1.925 \text{ m}^2$ ,  $2.1 \text{ m}^2$ , and  $2.275 \text{ m}^2$ .

### 5.2.3 Varying the initial density

For the case of the pulsed source, the change of the current's initial density (i.e. the change of the initial density anomaly) is the last variable to be tested. The initial current density anomaly is oscillated between  $1.094 \text{ kg m}^{-3}$  and  $1.407 \text{ kg m}^{-3}$  over the period of

24 hours. In the same manner as the previous two sections, the results obtained from the oscillation of the initial current density are shown in Figure 5.12. The current behaviour here is similar to the behaviour obtained from the oscillation of the initial velocity and cross-sectional area. However, the overshooting of the current's cross-sectional area is found to be bigger when the initial density anomaly is being oscillated. It is found that the cross-sectional area overshooting is directly proportional to the size of the downstream velocity envelope created by the steady state results, which are obtained from the limits of the oscillations.

The overshooting of the current's cross-sectional area is analysed against the change of the oscillation behaviour, as well as the change of the systems' state parameters. Following that, the individual terms of the equations are plotted and the results are analysed to study what causes the overshooting and what elements of the flow control it.

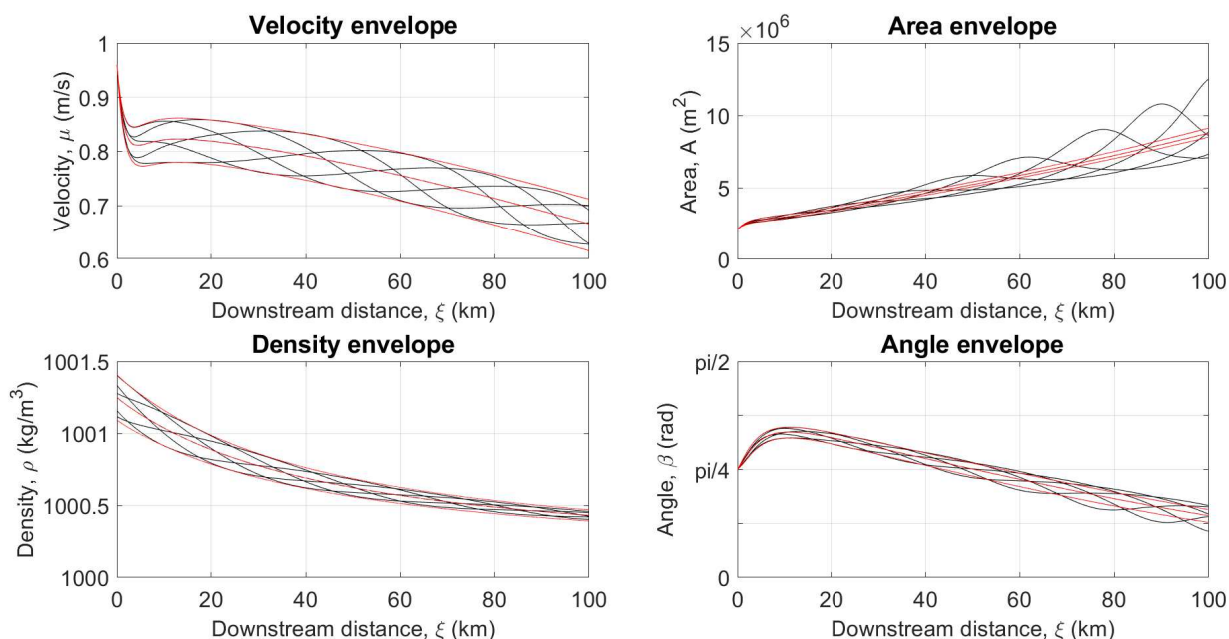


Figure 5.12: Down-stream envelopes of the four state variables for a time-dependent dense current in a rotating system. The initial density anomaly is oscillated between  $1.094 \text{ kg m}^{-3}$  and  $1.407 \text{ kg m}^{-3}$  over a period of 24 hours. The black lines represent the down-stream profiles and are plotted at four hour intervals. The red lines are the steady state solutions using initial density anomaly values of  $1.094 \text{ kg m}^{-3}$ ,  $1.25 \text{ kg m}^{-3}$ , and  $1.407 \text{ kg m}^{-3}$ .

### 5.3 The effect of changing the initial current path

Having studied the effects of a pulsed source on the descent of a dense current in a rotating homogeneous ambient, the effect of changing the current's initial pitch angle is now investigated. The current's initial velocity, cross-sectional area, and density anomaly are kept constant, and the initial angle is oscillated between  $\pi/2$  and zero over a 24 hour period. This translates to the current being directed directly down the slope along the positive  $y$  axis, and directly across the slope along the positive  $x$  axis. The current's state variables down-stream profiles are plotted every four hours and the results are presented in Figure 5.13.

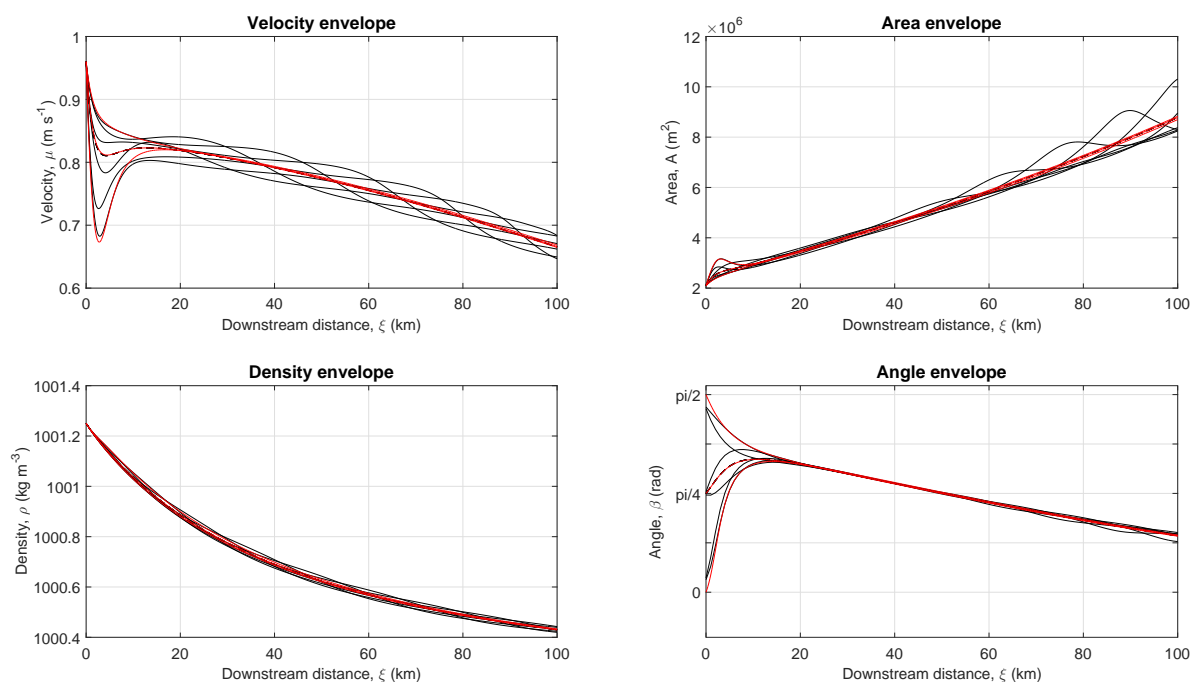


Figure 5.13: Down-stream envelopes of the four state variables for a time-dependent dense current in a rotating system. The initial current path is oscillated between an angle of  $\pi/2$  and zero (measured to the positive  $x$  direction). The period of oscillation is 24 hours

Looking at the results from the dense current with the varying initial path shown in Figure 5.13, it can be seen that the unsteady envelopes do not follow the predicted results

estimated by the steady state solutions plotted in red. In the steady state case, the current readjusts to find the single solution which matches the initial set of state variables and state parameters as illustrated in Chapter 4. However, when the variation of the current path is continuous, the current adjustment is also found to be continuous, which causes the current to not follow the steady state solutions. The amount of overshooting is found to be affected by both the oscillation properties, as well as the system set up of the current, especially the ambient fluid stratification rate.

## **5.4 The effects of the amplitude and frequency of the oscillations**

Having presented the effects of both the pulsed source and the change of the initial current path, the effects of changing the oscillations frequency and amplitude are next studied. In order to carry that out, the change of the initial current velocity is chosen to be the state variable being oscillated.

### **5.4.1 Change of the oscillation amplitude**

First, keeping the period of oscillation fixed at 24 hours, the same as subsection 5.2.1, the initial velocity is oscillated between  $0.66 \text{ m s}^{-1}$  and  $1.28 \text{ m s}^{-1}$ , giving an amplitude of  $0.62 \text{ m s}^{-1}$ , in comparison to an amplitude of  $0.16 \text{ m s}^{-1}$  in subsection 5.2.1. The results are presented in the same manner, by giving down-stream profiles of the four state variables every four hours. These are plotted in Figure 5.14. From the results and in comparison with Figure 5.10, it can be seen that the overshooting observed in the cross-sectional area of the current increases with the increase of the oscillation amplitude. In addition to that, the transition and propagation of the wave-like behaviour, observed in the profiles

of the state variables, is found to become steeper as the amplitude is increased, as well as getting steeper with the down-stream distance. Alongside these two results, the current experiences a “pinch off” down-stream, which can be seen in the envelopes of both the cross-sectional area and velocity.

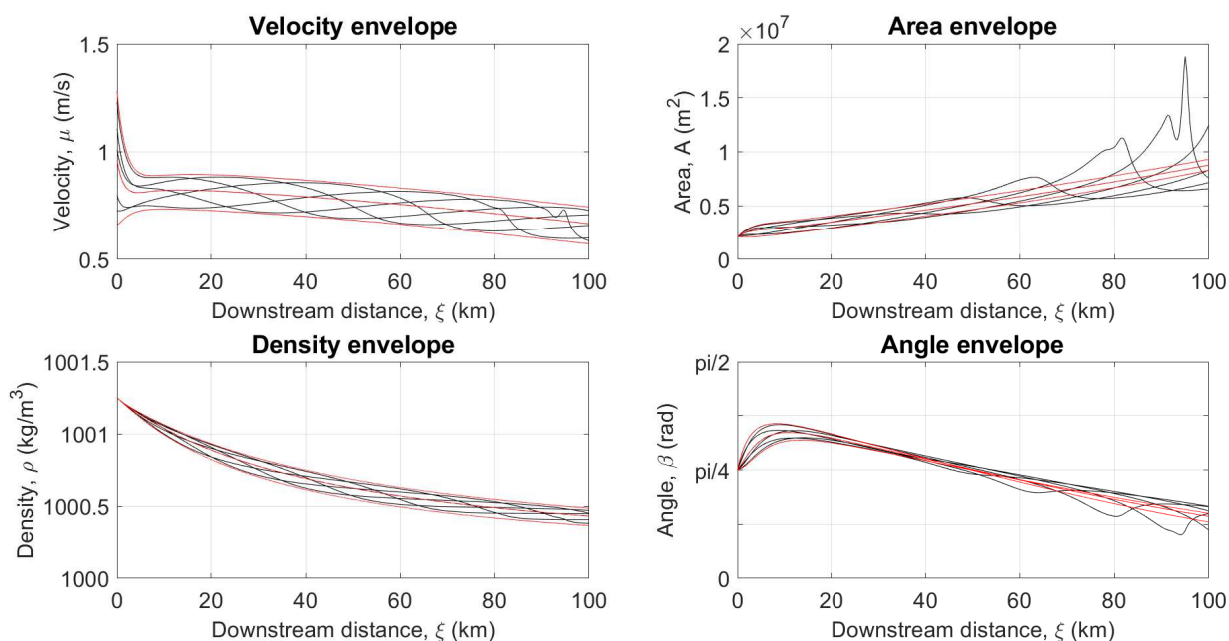


Figure 5.14: The four state variables’ envelopes plotted against the down stream distance with a varying initial source velocity for an unsteady dense current. The initial velocity is oscillated between  $0.66 \text{ m s}^{-1}$  and  $1.28 \text{ m s}^{-1}$ , with a period of 24 hrs.

### 5.4.2 Change of the oscillation frequency

The effects of changing the oscillation frequency is presented in this section. The oscillation amplitude of  $0.62 \text{ m s}^{-1}$  is carried on from the previous section, while the period of oscillation is first increased to 48 hours, then further to 96 hours, and the results are presented in Figures 5.15 and 5.16 respectively.

Figure 5.15 shows the down-stream profiles of the four state variables for a dense current under a pulsed source effect. With a period of oscillation of 48 hours, the profiles are

plotted every 8 hours. It can be seen that the current experiences an overshooting in the cross-sectional area envelope in comparison with the steady state solutions that are plotted using the limits of the oscillations of the initial velocity. The waves propagating through the current are found to become steeper as a function of the down-stream distance. Further increasing the period of oscillation to 96 hours, the results presented in Figure 5.16 also show a slight overshooting in the cross-sectional area. However, from comparing the three frequencies of oscillations, it can be seen that the current overshooting and wave behaviour decreases with the increase of the period of oscillation. It was also found that decreasing the frequency even further makes the current behave in a Quasi-steady way where a series of steady state solutions could be used to predict the down-stream behaviour of the current.

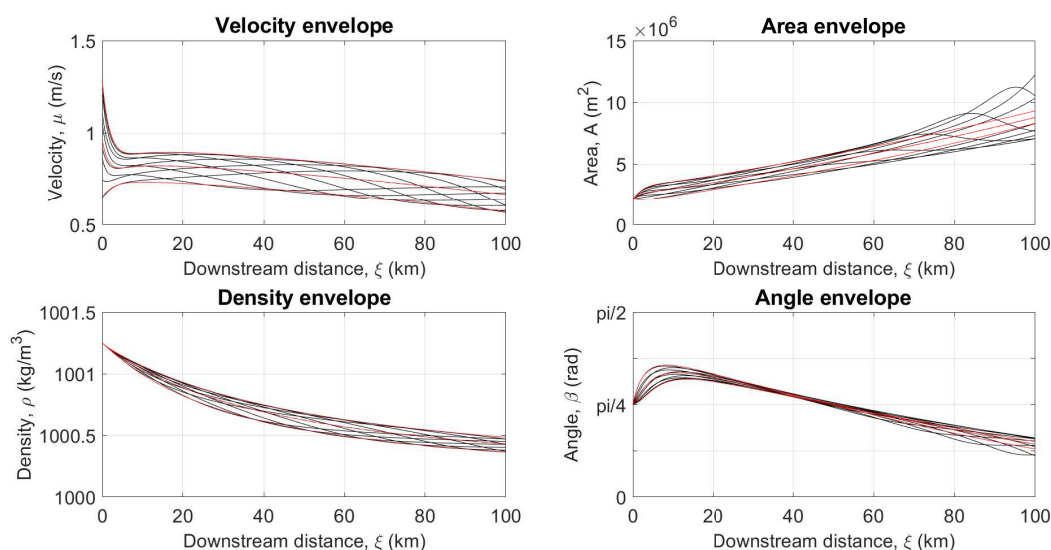


Figure 5.15: The four state variables' envelopes plotted against the down stream distance with a varying initial source velocity for an unsteady dense current. The initial velocity is oscillated between  $0.66 \text{ m s}^{-1}$  and  $1.28 \text{ m s}^{-1}$ , with a period of 48 hrs.

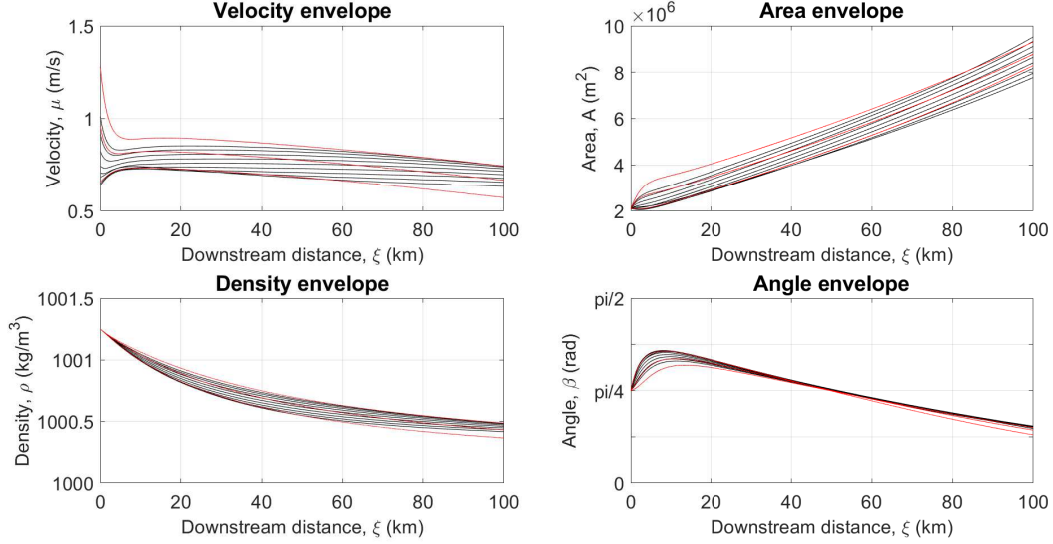


Figure 5.16: The four state variables' envelopes plotted against the down stream distance with a varying initial source velocity for an unsteady dense current. The initial velocity is oscillated between  $0.66 \text{ m s}^{-1}$  and  $1.28 \text{ m s}^{-1}$ , with a period of 96 hrs.

## 5.5 The effect of changing the stratification

The next parameter to be tested is the stratification rate of the ambient fluid. From the results presented in Chapter 4, it was found that the introduction of a background stratification rate causes the appearance of standing inertial waves. These waves were found to depend on the strength of the stratification as well as the Coriolis parameter and the drag coefficient of the system. Here the effects of the stratification rate strength on the unsteady currents are studied.

Starting with oscillating the initial current velocity, the amplitude ( $0.62 \text{ m s}^{-1}$ ) and oscillation period (96 hrs) from Figure 5.16 is carried forward. In the previous sections, the background ambient was kept homogeneous with a constant density of  $1000 \text{ kg m}^{-3}$ . Here the stratification rate is increased by  $T = 0.5 \times 10^{-6} \text{ m}^{-1}$  three times.

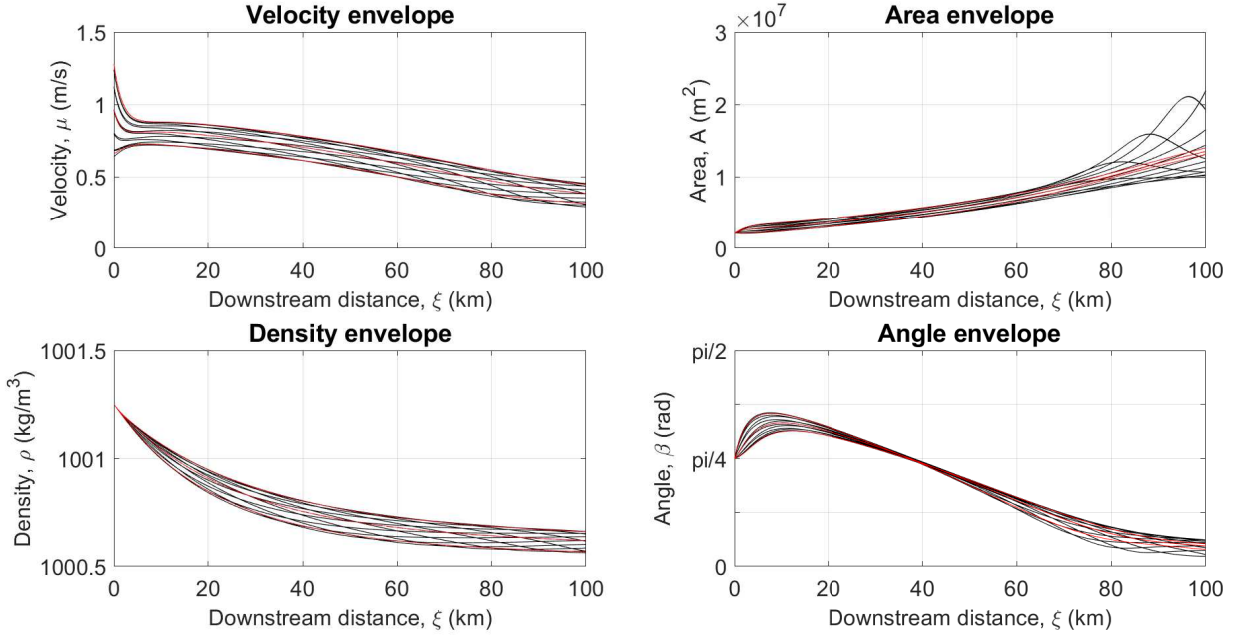


Figure 5.17: The four state variables' envelopes plotted against the down stream distance with a varying initial source velocity for an unsteady dense current. The initial velocity is oscillated between  $0.66 \text{ m s}^{-1}$  and  $1.28 \text{ m s}^{-1}$ , with a period of 96 hrs. The ambient stratification rate is set to  $\Delta\rho/\Delta y = 7.15 \times 10^{-6} \text{ kg m}^{-4}$ , which corresponds to  $T = 0.5 \times 10^{-6} \text{ m}^{-1}$  in the definition used by Smith [1975].

The first change in the stratification rate strength gives an ambient background with a stratification rate of  $\Delta\rho/\Delta y = 7.15 \times 10^{-6} \text{ kg m}^{-4}$ . The results from this are presented in Figure 5.17. The introduction of the background stratification rate, while keeping the rest of the system's parameters and variables the same, causes the introduction of the standing waves in the steady state case as was shown in Chapter 4. Moving onto the unsteady case, the overshooting in cross-sectional area of the dense current is found to be affected by the change in the stratification rate. From the top right panel of Figure 5.17, it can be seen that the down-stream cross-sectional area of the dense current under investigation overshoots the steady state solutions plotted in red more than the case when the ambient stratification was homogeneous (Figure 5.16). The current down-stream density and velocity profiles are found to remain within the “bounding” steady state solutions even with the introduction of the background ambient density stratification.

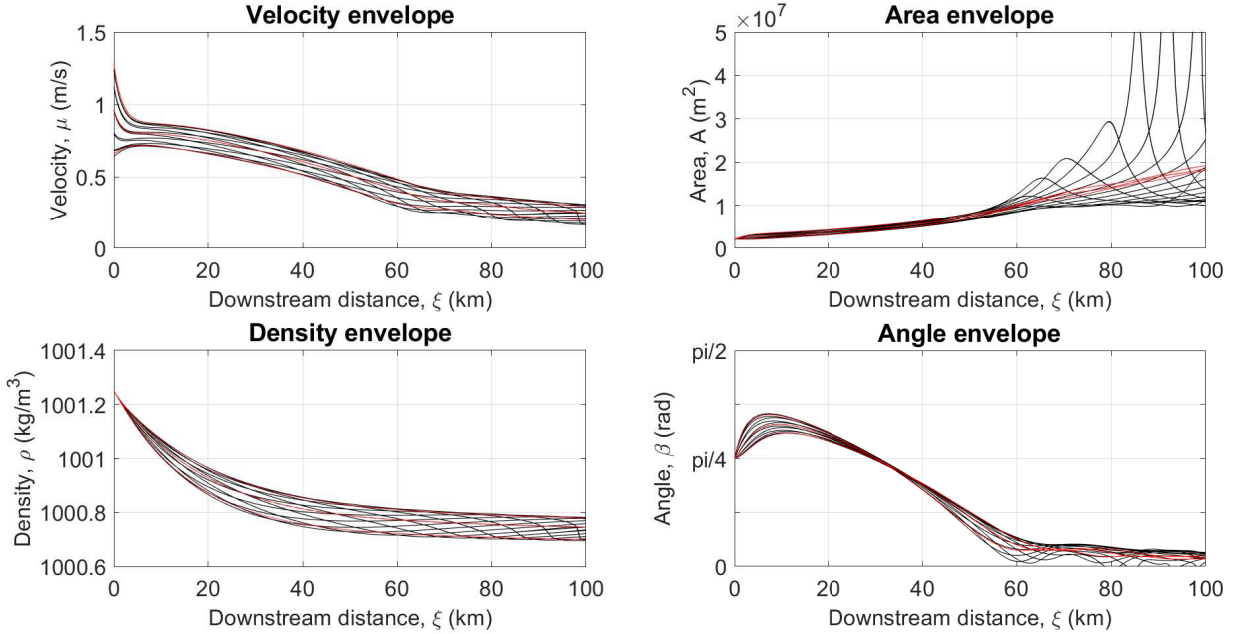


Figure 5.18: The four state variables' envelopes plotted against the down stream distance with a varying initial source velocity for an unsteady dense current. The initial velocity is oscillated between  $0.66 \text{ m s}^{-1}$  and  $1.28 \text{ m s}^{-1}$ , with a period of 96 hrs. The ambient stratification rate is set to  $\Delta\rho/\Delta y = 1.43 \times 10^{-5} \text{ kg m}^{-4}$ , which corresponds to  $T = 1 \times 10^{-6} \text{ m}^{-1}$  in the definition used by Smith [1975].

Further increasing the stratification rate gives rise to more overshooting in the cross-sectional area of the dense current. This is demonstrated in Figure 5.18.

Figure 5.18 gives the results for a dense current travelling through an ambient with a background stratification rate of  $\Delta\rho/\Delta y = 1.43 \times 10^{-5} \text{ kg m}^{-4}$ . Here the inertial waves in the steady state solutions plotted in red have higher spatial gradients than those shown in Figure 5.17, and as demonstrated in Chapter 4. The bigger standing waves in the steady state solutions indicate that the unsteady current has a changing background gradient that it needs to adapt to. This causes the overshooting of the waves in the unsteady current case to be directly proportionate to the background stratification rate of the ambient fluid. However, the second stratification rate causes the current to be beyond the threshold of the steady state oscillations. It can be seen that once this threshold is crossed, the current overshooting increases. In addition to the increase found in the

overshooting of the cross-sectional area of the dense current's downstream envelope, the current is found to experience a wave motion through its body as it moves down-stream. This wave is found to depend on the background stratification rate of the ambient fluid. From the results presented, the higher the stratification rate, the steeper the wave is found to be.

Before moving onto analysing the the results found here, and drawing conclusions as to why the overshooting takes place, the unsteady current behaviour is investigated under different state parameters to study the contribution these have on the overshooting that occurs here.

## 5.6 The effect of changing the state parameters

Having studied the effects of changing the initial source conditions of the state variables on the dense currents, attention is now turned to understanding how the state parameters affect the dense current down-stream behaviour. In order to do this, a base case of a dense current with a varying initial density is chosen. The source conditions are shown in Figure 5.19.

As can be seen from the figure, the initial current density at the source is varied between  $1000.62 \text{ kg m}^{-3}$  and  $1001.88 \text{ kg m}^{-3}$  while the ambient density at the source is kept constant at  $1000 \text{ kg m}^{-3}$ . This gives a variation in the density anomaly at the source between  $0.62 \text{ kg m}^{-3}$  and  $1.88 \text{ kg m}^{-3}$ .

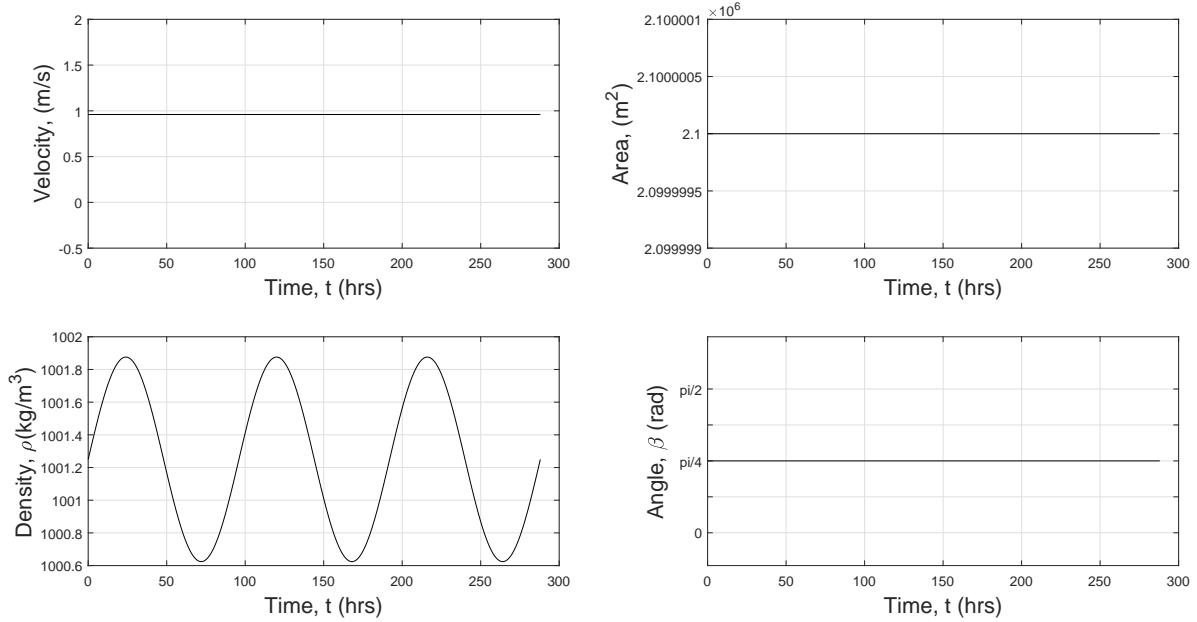


Figure 5.19: Dense current source conditions, showing the oscillations in the initial source density over time. The oscillation is between  $1001.88 \text{ kg m}^{-3}$  and  $1000.62 \text{ kg m}^{-3}$ , for an oscillation period of 96 hours. The ambient density is kept constant at  $1000 \text{ kg m}^{-3}$ , which means the density anomaly oscillates between  $0.62 \text{ kg m}^{-3}$  and  $1.88 \text{ kg m}^{-3}$ . The rest of the state variables are kept constant at the source.

The rest of the state variables' initial values at the dense current source are kept constant over time. These values are taken from the initial conditions from the Smith [1975] Mediterranean outflow.

In order to illustrate the effects of changing the state parameters, the ambient fluid is made to be homogeneous with no density stratification. This was chosen to eliminate any standing inertial waves which will arise in the presence of a background stratification as was shown in Chapter 4.

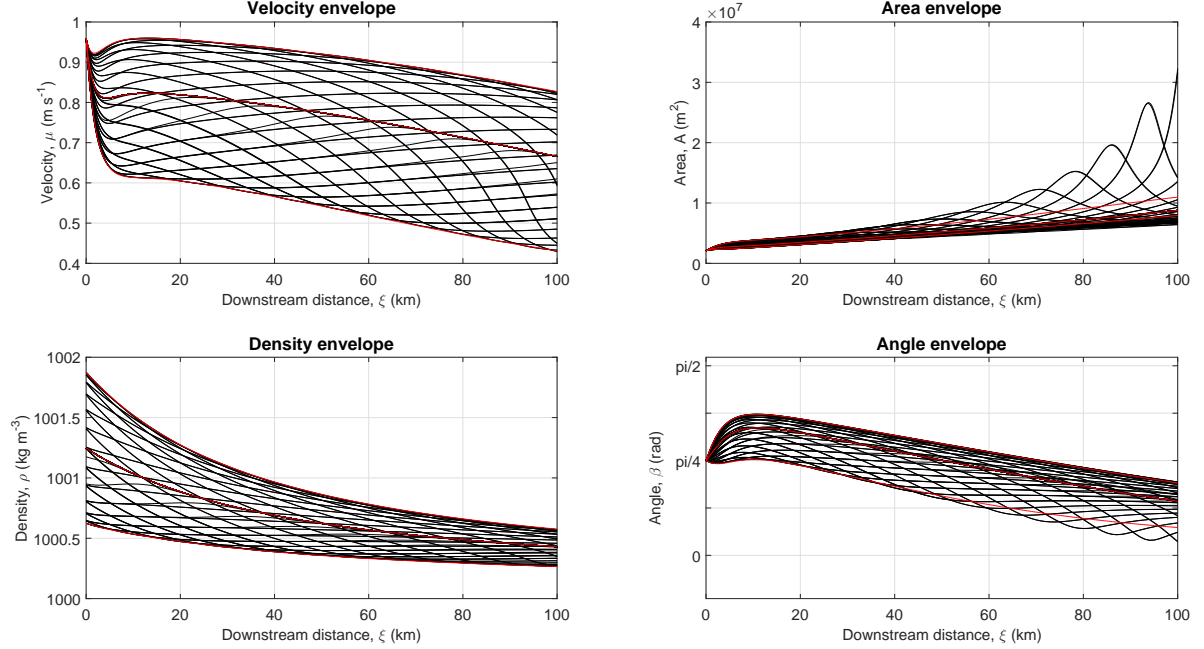


Figure 5.20: Down-stream envelopes of the four state variables for a time-dependent current in a rotating system. The source conditions are shown in Figure 5.19, where the initial current density at the source is oscillated over time. The red lines represent the steady state solutions obtained using the limits of the oscillations applied here. The state parameters are those of the Mediterranean outflow used in Smith [1975], with the ambient fluid being of a homogeneous structure.

Figure 5.20 gives the down-stream envelopes of the base case chosen to test the effects of changing the state variables. Here the Coriolis parameter has a value of  $0.854 \times 10^{-4} \text{ s}^{-1}$ , and the entrainment coefficient is set to 50 m, with 500 m for the drag coefficient. Using the source conditions shown in Figure 5.19, and plotting the down-stream envelopes every 8 hours, it can be seen that the current overshoots the cross sectional area envelopes (in red) predicted by the steady state solutions, with a maximum cross sectional area of over  $3 \times 10^7 \text{ m}^2$  100 km down-stream.

### 5.6.1 Coriolis

First the Coriolis parameter is varied. This is done by choosing a higher and a lower value than that of the base case, while the rest of the dense current set up is kept the same.

Initially the Coriolis parameter is reduced to  $0.598 \times 10^{-4} \text{ s}^{-1}$ , and the results are shown in Figure 5.21. It can be seen that the behaviour of the current is much smoother than that of a higher Coriolis parameter, and this causes the cross sectional area to overshoot, as well as softens the steepness of the waves travelling down-stream. This is further investigated by increasing the Coriolis parameter to  $0.598 \times 10^{-4} \text{ s}^{-1}$ , and the results are plotted in Figure 5.22. The increase in the rotational frequency of the system causes the current to overshoot more from the predicted cross sectional area envelope using the steady state solutions. In addition to that, the transition throughout the current of the waves is much steeper. This is due to the higher rotational rate of the system which causes the current to travel across the slope much sooner and at higher velocities as shown in Chapter 4. This is combined with the oscillation of the current initial density at the source, giving rise to more fluid being introduced to the system which is accelerating towards fluid moving at a slower velocity, causing more overshooting to occur.

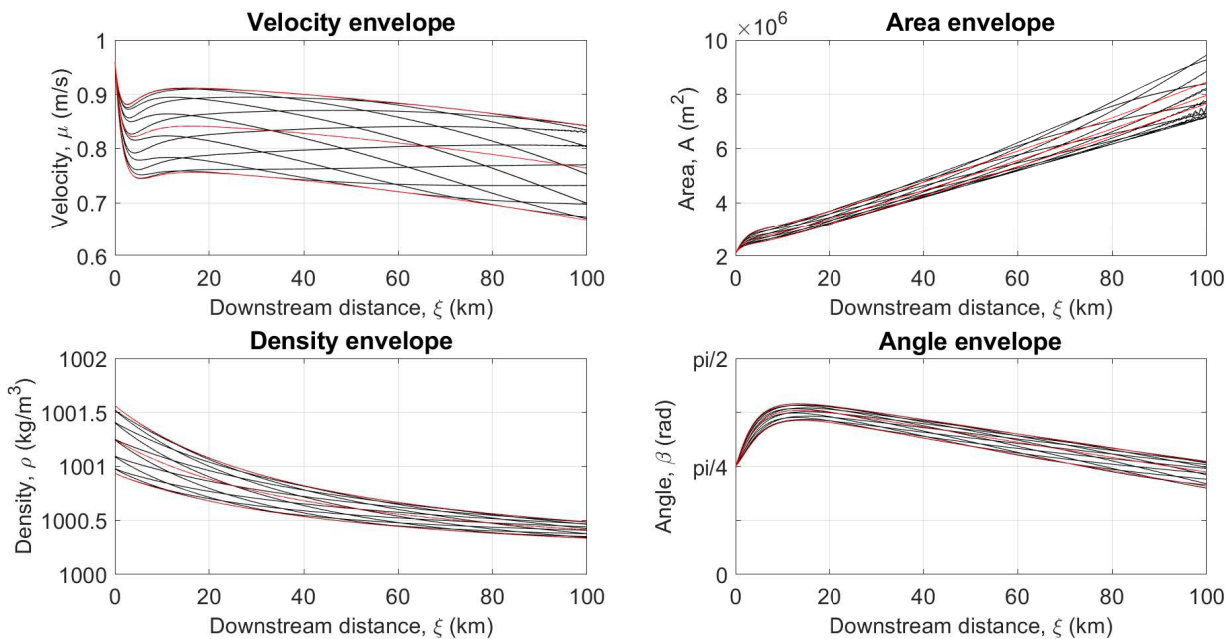


Figure 5.21: Down-stream envelopes of the four state variables for a time-dependent current in a rotating system. The source conditions are shown in Figure 5.19, where the initial current density at the source is oscillated over time. The red lines represent the steady state solutions obtained using the limits of the oscillations applied here. The state parameters are those of the Mediterranean outflow used in Smith [1975], with the ambient fluid being of a homogeneous structure, and the Coriolis parameter decreased to  $0.598 \times 10^{-4} \text{ s}^{-1}$ .

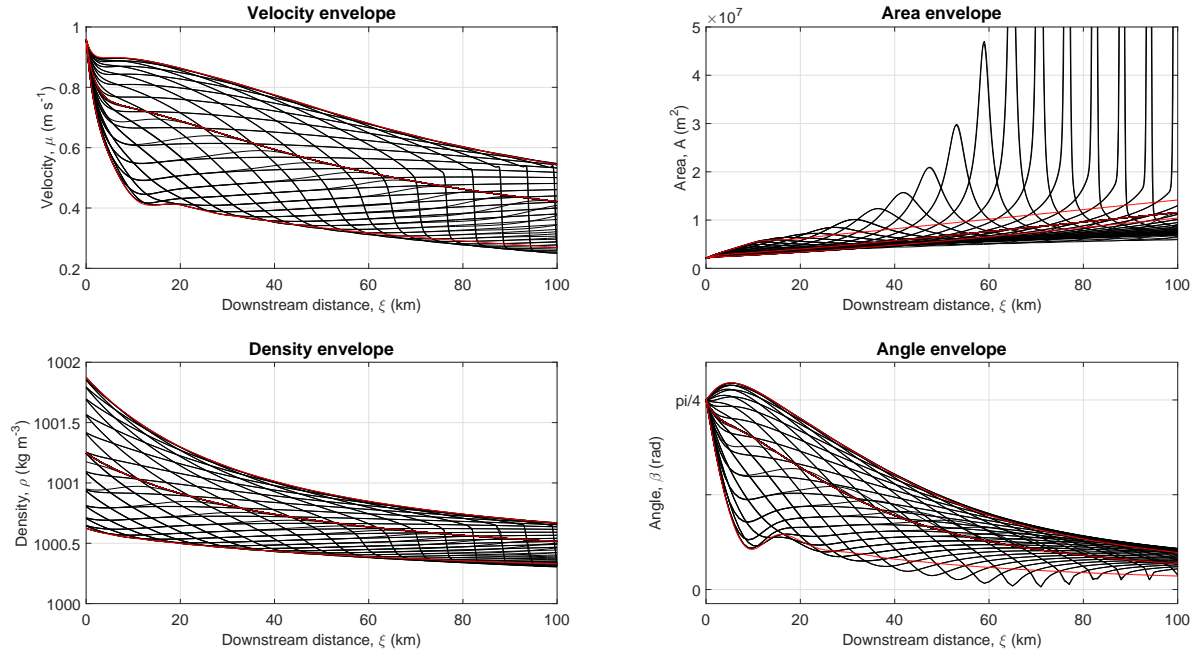


Figure 5.22: Down-stream envelopes of the four state variables for a time-dependent current in a rotating system. The source conditions are shown in Figure 5.19, where the initial current density at the source is oscillated over time. The red lines represent the steady state solutions obtained using the limits of the oscillations applied here. The state parameters are those of the Mediterranean outflow used in Smith [1975], with the ambient fluid being of a homogeneous structure, and the Coriolis parameter increased to  $1.708 \times 10^{-4} \text{ s}^{-1}$ .

Similar to the change in the stratification rate, the third Coriolis parameter used to obtain the results in Figure 5.22 is beyond the threshold of the steady state oscillatory behaviour. Here the current would experience oscillations due to two different physical phenomena.

## 5.6.2 Drag coefficient

Having looked into the effects of changing the Coriolis parameter on an unsteady dense current, the second state parameter to be investigated is the drag coefficient. The approach to do this is exactly the same as that carried out for the Coriolis parameter, where the initial base case variables and parameters are kept constant and only the drag coefficient is changed from one case to another.

The drag coefficient for the case plotted in Figure 5.20 is set to 500 m, which is the same value used by Smith [1975]. This value is first reduced to 375 m, and then increased to 666 m, and the current behaviour under each situation is studied.

Figure 5.23 gives the current down-stream envelopes over time for the dense current travelling under a drag coefficient of 375 m. The decrease in the drag coefficient causes the current to experience a higher cross sectional area overshooting. This is coupled with an increase in the steepness of the waves travelling through the system. The decrease in the drag gives less resistance to the fluid motion giving higher velocities, which in turn affects the current's cross sectional areas. In turn, increasing the drag coefficient, as shown here in Figure 5.24 where the drag is set to 666 m, causes the current to have a slower velocity profile. This affects the overshooting of the current cross sectional area, and the overshooting is found to decrease with the increase of the drag coefficient.

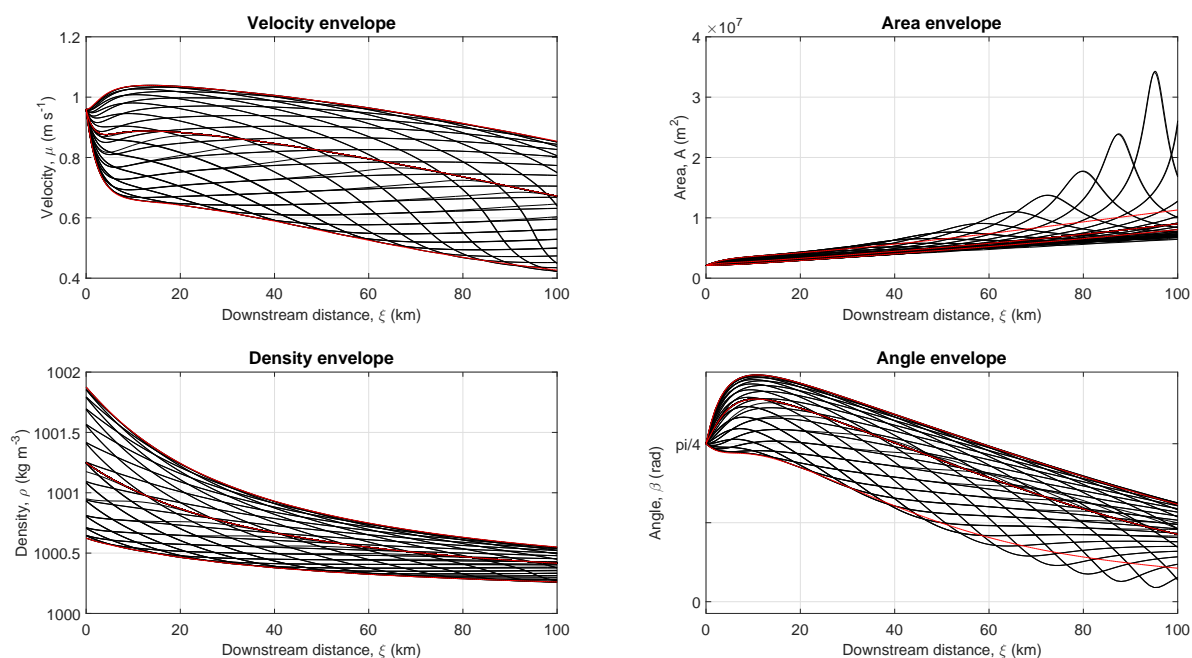


Figure 5.23: Down-stream envelopes of the four state variables for a time-dependent current in a rotating system. The source conditions are shown in Figure 5.19, where the initial current density at the source is oscillated over time. The red lines represent the steady state solutions obtained using the limits of the oscillations applied here. The state parameters are those of the Mediterranean outflow used in Smith [1975], with the ambient fluid being of a homogeneous structure, and the drag coefficient decreased to 375 m.

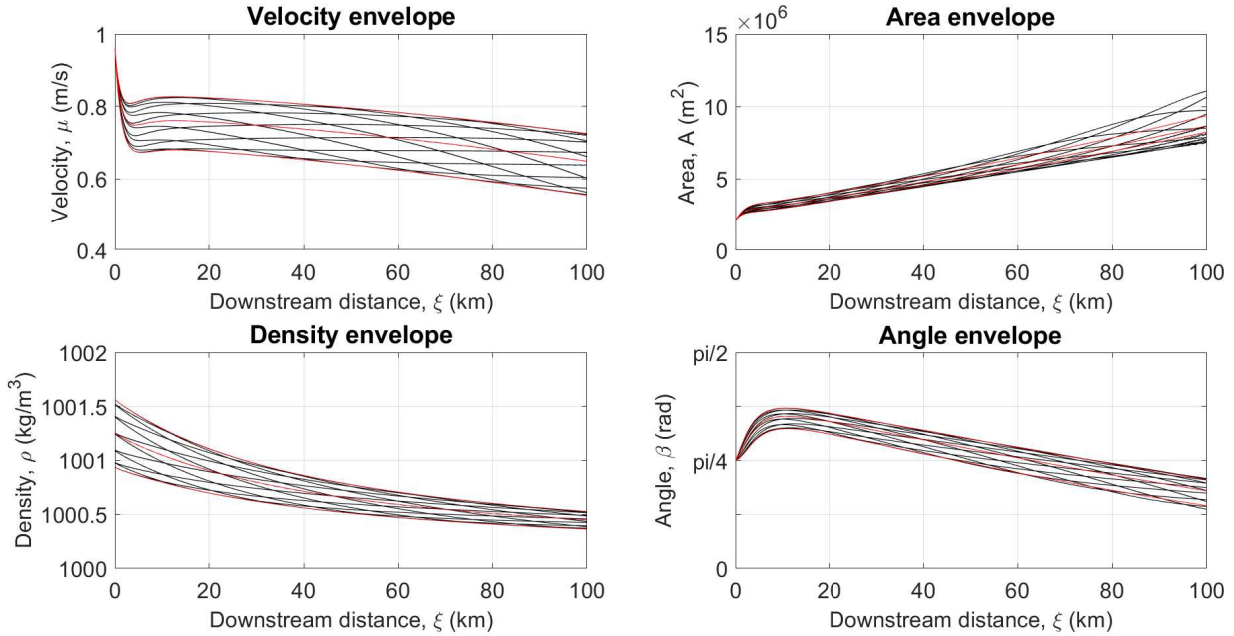


Figure 5.24: Down-stream envelopes of the four state variables for a time-dependent current in a rotating system. The source conditions are shown in Figure 5.19, where the initial current density at the source is oscillated over time. The red lines represent the steady state solutions obtained using the limits of the oscillations applied here. The state parameters are those of the Mediterranean outflow used in Smith [1975], with the ambient fluid being of a homogeneous structure, and the drag coefficient increased to 666 m.

### 5.6.3 Entrainment coefficient

The last state variable to be investigated is the entrainment coefficient. The case for the current shown in Figure 5.20 is produced using an entrainment coefficient of 50 m. This value is initially reduced to 37.5 m and the results from this are shown in Figure 5.25, and then increased to 666 m where the results are shown in Figure 5.26.

From the results it can be seen that the increase of the entrainment coefficient causes the dense current cross sectional to overshoot more. This is expected as the amount of fluid entrained into the dense current is directly proportionate to the entrainment coefficient. The result are consistent with the results from Section 3.4, where it is found that the lower entrainment coefficient gives a higher overall velocity profile, which is the case here

as well. The interesting result found is that the entrainment coefficient change does not have an effect on the steepness of the wave behaviour throughout the current.

Having looked into the effects of both the prime variables and state parameters on the evolution of the dense currents in the unsteady systems, the actual cause of the overshooting is now analysed.

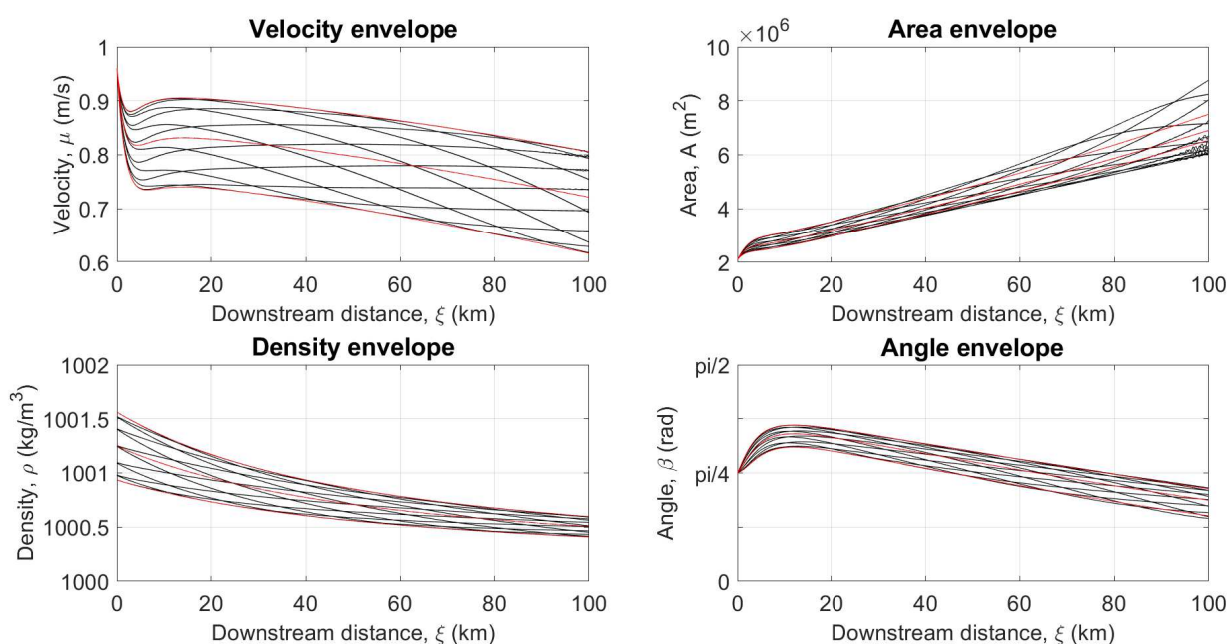


Figure 5.25: Down-stream envelopes of the four state variables for a time-dependent current in a rotating system. The source conditions are shown in Figure 5.19, where the initial current density at the source is oscillated over time. The red lines represent the steady state solutions obtained using the limits of the oscillations applied here. The state parameters are those of the Mediterranean outflow used in Smith [1975], with the ambient fluid being of a homogeneous structure, and the entrainment coefficient decreased to 37.5 m.

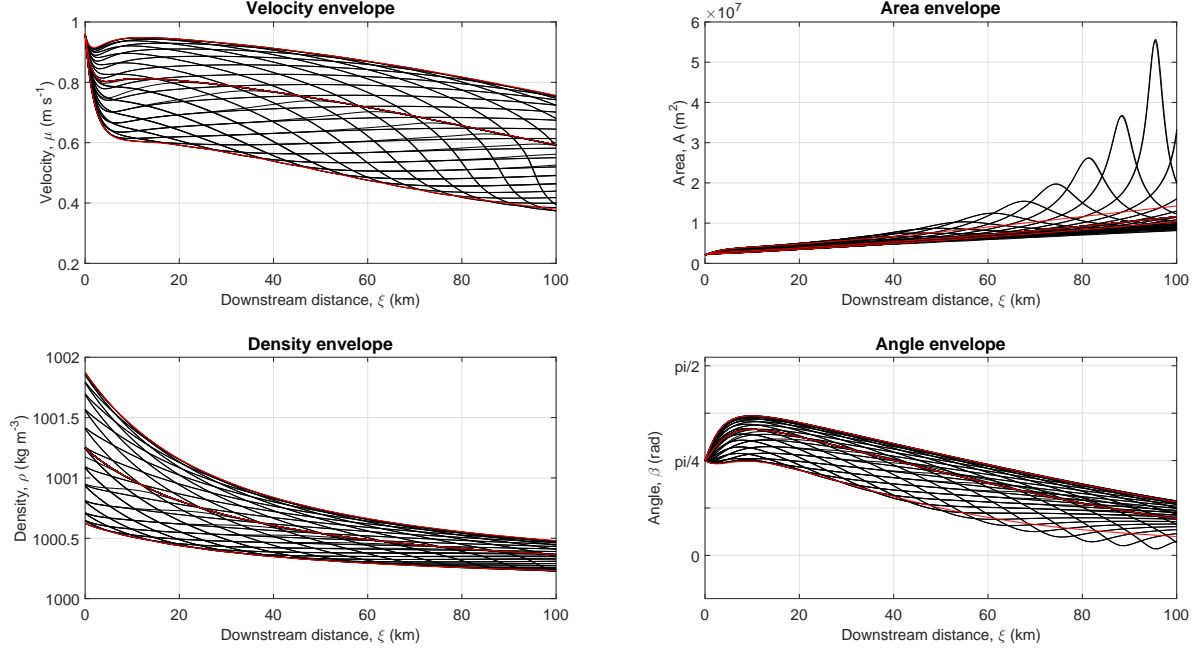


Figure 5.26: Down-stream envelopes of the four state variables for a time-dependent current in a rotating system. The source conditions are shown in Figure 5.19, where the initial current density at the source is oscillated over time. The red lines represent the steady state solutions obtained using the limits of the oscillations applied here. The state parameters are those of the Mediterranean outflow used in Smith [1975], with the ambient fluid being of a homogeneous structure, and the entrainment coefficient increased to 666 m.

## 5.7 Analysis of the overshooting

In order to analyse the overshooting of the cross sectional area of the dense current in the unsteady cases, the individual terms of the equations are investigated.

The system used to solve the unsteady cases introduces four perturbed quantities related to the state variables and to the equations that are both time and space dependent. This gives the following equations:

$$\frac{\partial A\tilde{A}}{\partial t} + \frac{\partial \mu\tilde{\mu}A\tilde{A}}{\partial \xi} = E_0\mu\tilde{\mu}, \quad (5.1)$$

$$\frac{\partial \rho \tilde{\rho} A \tilde{A}}{\partial t} + \frac{\partial \rho \tilde{\rho} \mu \tilde{\mu} A \tilde{A}}{\partial \xi} = E_0 \mu \tilde{\mu} \rho_e, \quad (5.2)$$

$$\frac{\partial \rho \tilde{\rho} \mu \tilde{\mu} A \tilde{A}}{\partial t} + \frac{\partial \rho \tilde{\rho} \mu^2 \tilde{\mu}^2 A \tilde{A}}{\partial \xi} = g A \tilde{A} \sin \alpha \Delta \rho \sin(\beta \tilde{\beta}) - \rho \tilde{\rho} K \mu^2 \tilde{\mu}^2, \quad (5.3)$$

and

$$\frac{\partial \beta \tilde{\beta}}{\partial t} + \frac{\partial \mu \tilde{\mu} \beta \tilde{\beta}}{\partial \xi} = \frac{g \sin \alpha \Delta \rho \tilde{\rho}}{\rho \tilde{\rho} \mu \tilde{\mu}} \cos(\beta \tilde{\beta}) - \hat{f}. \quad (5.4)$$

The product rule is then applied in order to calculate the terms denoted with  $(\hat{\cdot})$ . These terms are set to “one” at the source for the case of the steady state current, and are varied accordingly as required for the unsteady cases. Here the case plotted in Figure 5.18 is used to illustrate the approach taken, and then gives an indication of how the overshooting of the cross-sectional area occurs in the unsteady dense currents.

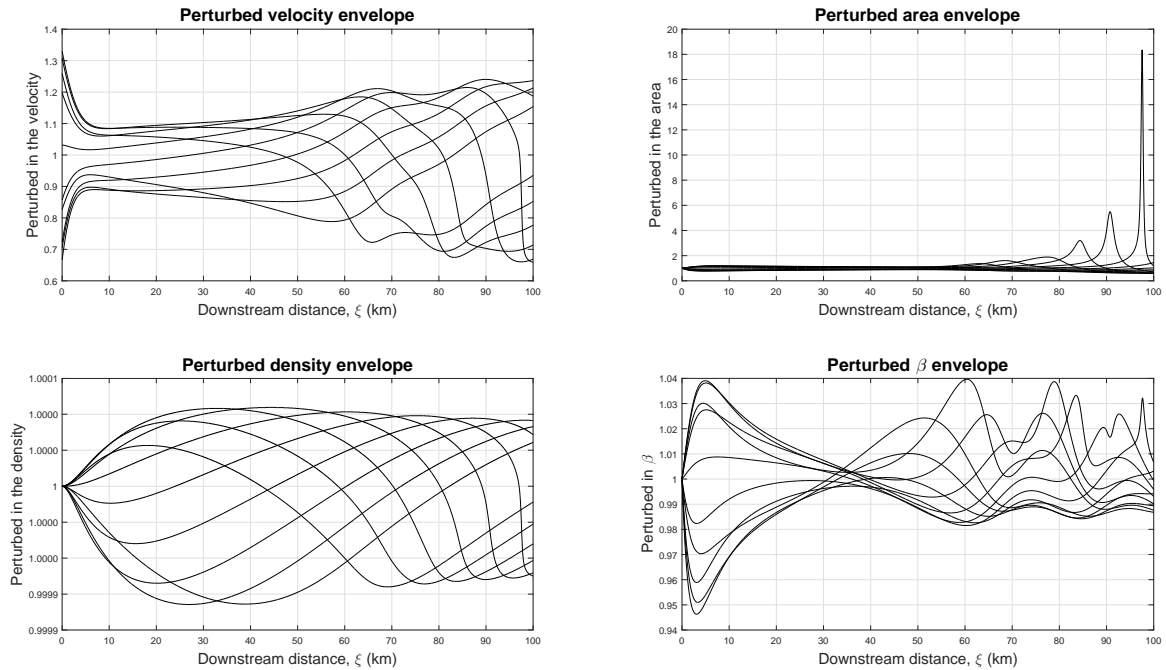


Figure 5.27: The down-stream envelopes of the perturbed quantities for the state variables arising from varying the initial current velocity at the source between 0.7 and 1.3 of the original base case. The variations in the other three state variables are in response to the varying initial source velocity.

Figure 5.27 gives the down-stream envelopes of the perturbed quantities for the case shown in Figure 5.18. It can be seen that the envelopes of each of the state variables match those of the perturbed variables. Figure 5.27 also illustrates the overshooting that occurs in the cross-sectional area of the current.

For further investigation of the overshooting, the spatial and temporal derivatives of each of the state variables is taken into account to see what happens through the current as the initial source conditions are perturbed.

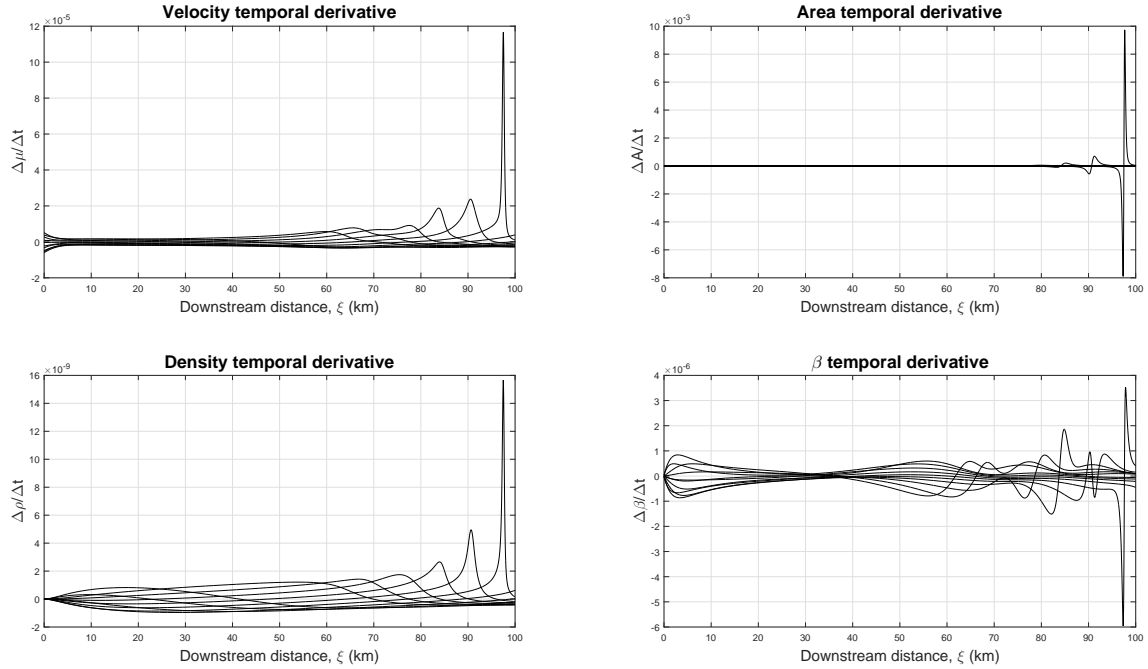


Figure 5.28: The down-stream temporal derivatives of the state variables for an unsteady dense current with an oscillation in the source velocity. The full state variables envelopes are shown in Figure 5.18.

Both the temporal derivatives of the state variables shown in Figure 5.28 and the spatial derivatives of the state variables shown in Figure 5.29 show that the derivatives increase with the down-stream distance. This is consistent with the envelopes of the state variables shown previously in Figure 5.18. In addition to that, the results here express how steep the transition of current properties can be throughout the current body, but without any wave breaking taking place.

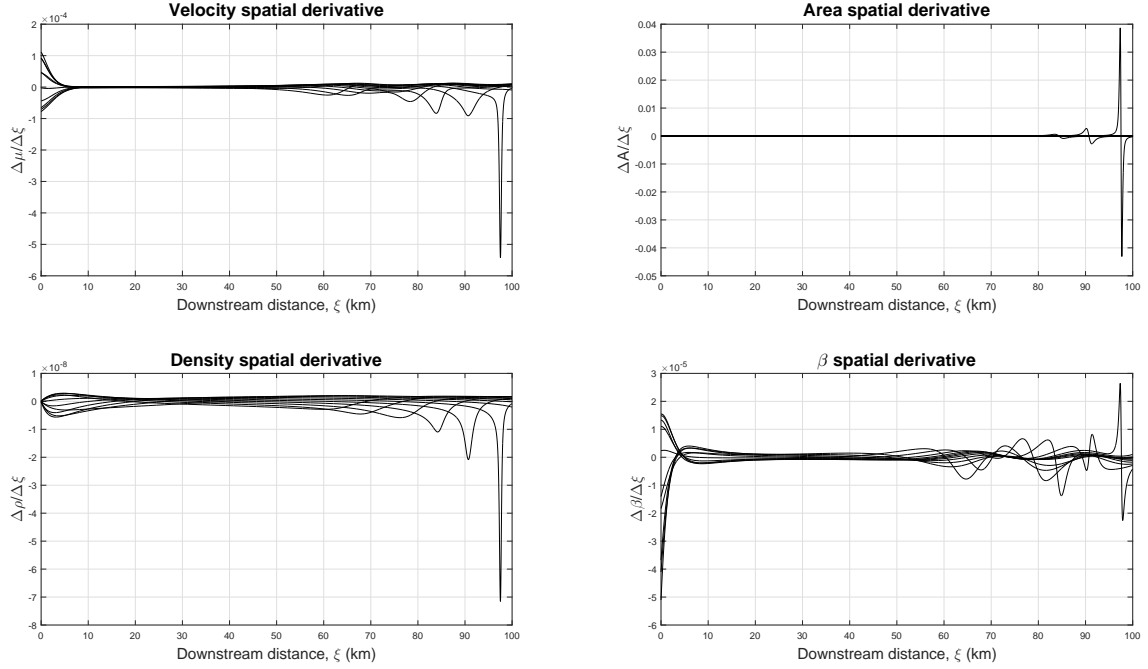


Figure 5.29: The down-stream spatial derivatives of the state variables for an unsteady dense current with an oscillation in the source velocity. The full state variables envelopes are shown in Figure 5.18.

In order to investigate which terms are leading in the equations, the equation used to calculate the temporal derivatives of the perturbed cross-sectional area is plotted as individual terms. The equation states that:

$$\frac{\partial \tilde{A}}{\partial t} = \mu \tilde{A} \frac{\partial \tilde{\mu}}{\partial \xi} + \mu \tilde{\mu} \frac{\partial \tilde{A}}{\partial \xi} + \frac{E_0 \mu \tilde{\mu} \tilde{A}}{A}. \quad (5.5)$$

Figure 5.30 gives the terms of Equation 5.5 plotted for an unsteady dense current with a varying source velocity. The conditions of the current and the oscillation of the source are shown in the case plotted in Figure 5.18. The left hand side term is plotted in black, the first term on the right hand side is plotted in light blue, and the second term on the right hand side is plotted in red. The final term was found to not be a leading term, and

in order to help with visualizing the other three terms, it was taken out of the plot.

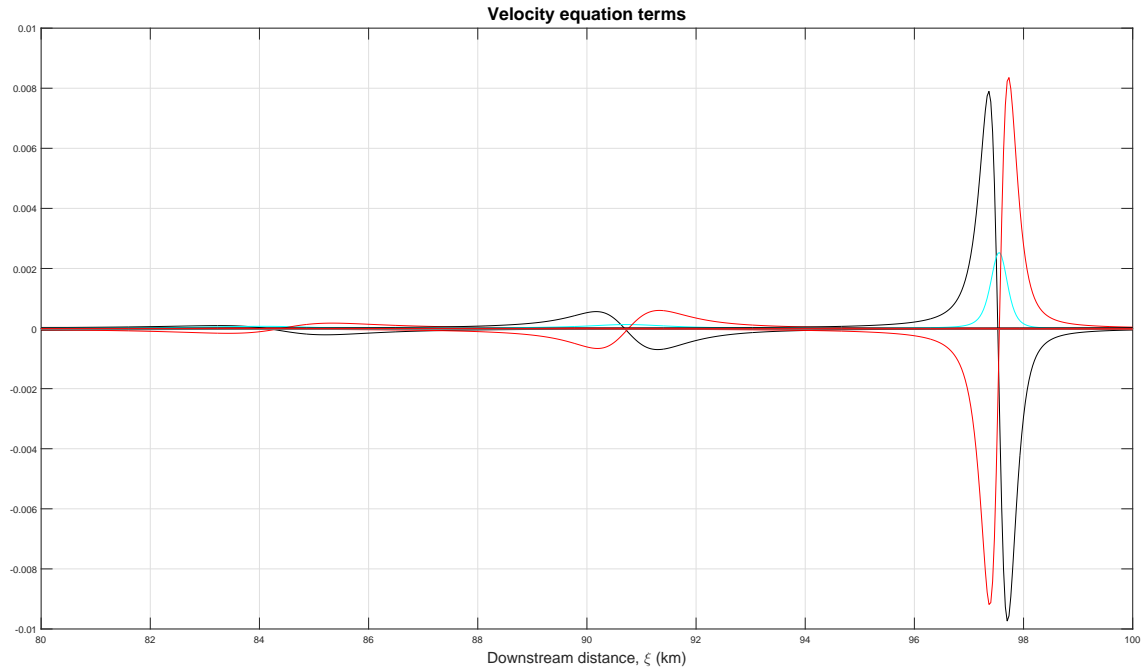


Figure 5.30: The terms of the equation used to calculate the temporal derivatives of the perturbed cross-sectional area of the dense current are plotted against the down stream distance. The equation is shown in Equation 5.5, however only the first two terms on the right hand side in addition to the left hand side term are plotted here as they are found to be the leading terms of the equation.

As was the case with other tests that were run, Figure 5.30 shows that the terms with the spatial derivative of the cross sectional area are the terms that act as the leading terms on the right hand side of the equations used to calculate the temporal derivatives of the state variables. The derivatives are found to increase with the down-stream distance, while increasing with both the oscillation amplitude and frequency. This increase was found to represent how much fluid was introduced to the system at the source, and how the current dealt with this. As new fluid was released from the source, it adapted to the system, and in the case of a continuous increase the fluid would catch up with the fluid released before it, causing the cross-sectional spatial derivative to increase. In the same

manner, when there was a decrease in the amount of fluid emitted from the source, the newly released fluid was found to move slower than that released earlier which caused a decrease in the cross-sectional area prediction. As the amplitude and frequency of the source oscillations increased, the current was experiencing higher cross-sectional area overshooting, and that was found to be solely due to the current adapting to the high amount of fluid that was released over time. This gave rise to waves travelling through the current which represent faster moving fluid “catching up” with slower moving fluid ahead of it which was released earlier from the source. The two parts of the fluid (ahead of the wave and behind it) had different densities as well as velocities, and the current’s cross sectional area was expanding due to the continuous motion of the fluid “catching up”. As the system does not handle any wave breaking, the cross-sectional area was found to keep increasing, which would not be the case in reality. It is suggested that this system is to be taken as the base case for modelling unsteady dense currents in rotating systems, with the assumption that it will over predict the values of the cross-sectional area after the down-stream distance of wave breaking. Holland et al. [2014] showed that an unsteady line plume would experience wave breaking, this wave breaking would occur closer to the source for higher amplitudes and frequencies. Further investigation is now required to determine the downstream distance where the wave breaking takes place for the newly developed unsteady model.

# Chapter 6

## Conclusion

### 6.1 Summary of thesis

The thesis covers the research carried out in order to address the effects of tidal activity on dense ocean currents. The tidal activity makes the sources of these currents behave in a time dependent manner, giving rise to unsteady currents. The effect of having a background stratification rate in the ambient fluid which the current travels through was also studied, as well as the strength of this stratification rate. Numerical simulations of the current behaviours were carried out, and the effect of changing different parameters and state variables on the current behaviour were analysed.

### 6.2 General conclusions

Through applying the same mathematical derivation approach used by Scase et al. [2006], the steady streamtube model established by Smith [1975] was developed to account for temporal changes at the sources of dense ocean currents, and study the effect these

changes would have on the down-stream behaviour of the currents.

Gordon et al. [2004] suggested that a steady state dense current experiences an adjustment in the velocity profile that is dependent on the density anomaly between the current and the ambient, and is also affected by the initial current velocity. This study showed that this adjustment is not only dependent on that, but for a set of state parameters, a dense steady state current would readjust to one profile for each of the state variables. This adjustment takes place near the source creating rapid changes in the current's state variable profiles. This adjustment was also found to affect the current's final position and properties. When looking at the four state variables of the current, the study found that the change in the density anomaly between the current and the surrounding ambient carried the most significant effect on the dense current's down-stream behaviour. This was due to the fact that the current was driven by two main forces, buoyancy and Coriolis, and the change of the density anomaly was affecting the buoyancy force directly. In addition, the changes of the current's initial cross sectional area and velocity were found to have less of an impact on the current final positioning and down-stream state variable profiles. Moreover, the change of the initial current's inclination had the least impact on the current. This was because the change did not affect any of the physics surrounding the current, and the study showed that the down-stream profiles of the state variables for a dense current in a homogeneous ambient with different initial pitch angles collapsed onto one solution.

In the presence of a background ambient stratification rate, steady state currents were found to experience an oscillatory behaviour. These oscillations were found to be affected by the strength of the density stratification, the entrainment and drag coefficients, as well as the rotational rate of the system. Previous research indicated that these oscillatory behaviours cause the dense currents to split up into sub-currents with different trajectories [Jiang and Garwood Jr, 1996], but since the streamtube model handles the current as

one coherent structure, this was not observed. The steady state oscillations were found to increase in amplitude with the increase of the state variables as well as the drag and entrainment coefficients of the dense current. A newly developed threshold showed that these oscillations exist even in the absence of a background ambient stratification. The study was able to identify two relationships, when adhered, a steady state current would not oscillate downstream.

The newly developed system revealed that when a dense current experiences continuous changes in the initial state variables' values at the source it experiences waves that travel down the current. These unsteady waves were found to be affected by the source oscillations as well as the state parameters of the system. The steepness of the unsteady waves was found to increase with the increase of the source oscillations' frequency and amplitude. As the model does not support wave breaking, the current down-stream solutions, namely the state variables' profiles, were found not to follow the limits set by the steady state solutions for the values of which the source conditions are oscillated between. The study also found that the unsteady waves increased in both frequency and magnitude with the introduction of a background stratification rate.

The physical process that was found to govern the unsteady dynamics was the rotational rate of the system, whereas the drag experienced by the current, due to the flow through the system, and the amount of ambient fluid entrained into the current, were found to have less of an impact on the behaviour of the unsteady currents as long as they satisfied the threshold of the steady state oscillations. The higher the Coriolis parameter, the stronger the waves introduced due to the unsteadiness of the source are, which causes the current to overshoot the predicted steady state solutions more. It is expected that systems with higher rotational rates will have higher turbulent behaviour and more wave breaking.

### 6.3 Future work

The threshold of the steady state current oscillatory behaviour was found here using a numerical analysis. As this study looked into developing a new unsteady model, the behaviour of the oscillations beyond the threshold were not quantified, however the general effect of each parameter was studied. This work could carry on using the same numerical analysis implemented to establish the threshold of where the oscillations occur.

For the newly developed unsteady model, and having established that the unsteady dynamics are governed by the oscillations of the current source. In addition to the dependency on which the state variables is being oscillated, as well as the rotational rate of the system, and the ambient stratification. The next step would be to examine in detail, the probability of wave breaking, which would be given as a function of the distance away from the source, and dependent on the physical settings mentioned above. This would establish the downstream threshold of where the current system could be implemented to.

The numerical system used throughout this thesis is of a low order. Having established the well-posedness of the new model, a higher order numerical method would be desired. This would help with the computational power required to model the currents.

In addition to establishing wave breaking dependency, the situation of varying more than one source condition should be considered. This study tried to distinguish between the effects of each individual parameter. However, when compared to the real physical world, oscillatory behaviour can occur across a number of parameters at the same time.

# Bibliography

- M. H. Alford. Redistribution of energy available for ocean mixing by long-range propagation of internal waves. *Nature*, 423(6936):159–162, 2003.
- L. Armi. Some evidence for boundary mixing in the deep ocean. *Journal of Geophysical Research: Oceans*, 83(C4):1971–1979, 1978.
- P. G. Baines and S. Condie. Observations and modelling of antarctic downslope flows: A review. *Antarctic Research Series*, 75:29–49, 1998.
- M. Baringer and J. Price. Momentum and energy balance of the mediterranean outflow. *Journal of physical oceanography*, 27(8):1678–1692, 1997.
- J. Bear. *Dynamics of fluids in porous media*. Courier Corporation, 2013.
- P. E. Biscaye. Mineralogy and sedimentation of recent deep-sea clay in the atlantic ocean and adjacent seas and oceans. *Geological Society of America Bulletin*, 76(7):803–832, 1965.
- V. Bjerknes, T. Bergeron, J. Bjerknes, and H. S. Solberg. *Hydrodynamique physique avec applications a la météorologie dynamique*. Les Presses universitaires de France, 1934.
- F. Bo Pedersen. Dense bottom currents in rotating ocean. *Journal of the Hydraulics Division*, 106(8):1291–1308, 1980.
- K. Borenäs, A. Wåhlin, I. Ambar, and N. Serra. The mediterranean outflow splitting

- comparison between theoretical models and canigo data. *Deep Sea Research Part II: Topical Studies in Oceanography*, 49(19):4195–4205, 2002.
- J. Boussinesq. *Théorie analytique de la chaleur: mise en harmonie avec la thermodynamique et avec la théorie mécanique de la lumière*, volume 2. Gauthier-Villars, 1903.
- W. S. Broecker et al. The great ocean conveyor. *Oceanography*, 4(2):79–89, 1991.
- C. Cenedese and C. Adduce. Mixing in a density-driven current flowing down a slope in a rotating fluid. *Journal of Fluid Mechanics*, 604:369–388, 2008.
- C. Cenedese, J. Whitehead, T. Ascarelli, and M. Ohiwa. A dense current flowing down a sloping bottom in a rotating fluid. *Journal of Physical Oceanography*, 34(1):188–203, 2004.
- S. Chang and X. Wang. Courant number insensitive ce/se euler scheme. In *38th AIAA/ASME/SAE/ASEE Joint Propulsion Conference & Exhibit*, page 3890, 2002.
- COAS. Osu tidal inversion. <http://volkov.oce.orst.edu/tides/>. Accessed: 2016-12-22.
- L. Cooper. Deep water movements in the north atlantic as a link between climatic changes around iceland and biological productivity of the english channel and celtic sea. *Journal of Marine Research*, 14(4):347–362, 1955.
- L. Cooper. Vertical and horizontal movements in the ocean. *M. Sears [cd.]*, *Oceanography*. AAAS, *Publ*, 67:599–621, 1961.
- D. L. Cutchin and R. L. Smith. Continental shelf waves: Low-frequency variations in sea level and currents over the oregon continental shelf. *Journal of Physical Oceanography*, 3(1):73–82, 1973.

- G. Davidson. Gaussian versus top-hat profile assumptions in integral plume models. *Atmospheric Environment (1967)*, 20(3):471–478, 1986.
- T. Ellison and J. Turner. Turbulent entrainment in stratified flows. *Journal of Fluid Mechanics*, 6(3):423–448, 1959.
- S. Erofeeva, L. Padman, and G. Egbert. Assimilation of ship-mounted adcp data for barotropic tides: Application to the ross sea. *Journal of Atmospheric and Oceanic Technology*, 22(6):721–734, 2005.
- T. Ezer. Entrainment, diapycnal mixing and transport in three-dimensional bottom gravity current simulations using the mellor–yamada turbulence scheme. *Ocean Modelling*, 9(2):151–168, 2005.
- T. Ezer. Topographic influence on overflow dynamics: Idealized numerical simulations and the faroe bank channel overflow. *Journal of Geophysical Research: Oceans*, 111(C2), 2006.
- T. D. Foster and E. C. Carmack. Frontal zone mixing and antarctic bottom water formation in the southern weddell sea. In *Deep Sea Research and Oceanographic Abstracts*, volume 23, pages 301–317. Elsevier, 1976.
- M. Germano. Turbulence: the filtering approach. *Journal of Fluid Mechanics*, 238: 325–336, 5 1992. ISSN 1469-7645. doi: 10.1017/S0022112092001733. URL [http://journals.cambridge.org/article\\_S0022112092001733](http://journals.cambridge.org/article_S0022112092001733).
- J. B. Girton, L. J. Pratt, D. A. Sutherland, and J. F. Price. Is the faroe bank channel overflow hydraulically controlled? *Journal of physical oceanography*, 36(12):2340–2349, 2006.
- F. S. Godeferd and F. Moisy. Structure and dynamics of rotating turbulence: a review of

- recent experimental and numerical results. *Applied Mechanics Reviews*, 67(3):030802, 2015.
- A. L. Gordon, E. Zambianchi, A. Orsi, M. Visbeck, C. F. Giulivi, T. Whitworth, and G. Spezie. Energetic plumes over the western ross sea continental slope. *Geophysical Research Letters*, 31(21), 2004.
- A. L. Gordon, A. H. Orsi, R. Muench, B. A. Huber, E. Zambianchi, and M. Visbeck. Western ross sea continental slope gravity currents. *Deep Sea Research Part II: Topical Studies in Oceanography*, 56(13):796–817, 2009.
- R. Griffiths. Gravity currents in rotating systems. *Annual Review of Fluid Mechanics*, 18(1):59–89, 1986.
- J. M. Hamrick. A three-dimensional environmental fluid dynamics computer code: Theoretical and computational aspects. 1992.
- Y. Heggelund, F. Vikebø, J. Berntsen, and G. Furnes. Hydrostatic and non-hydrostatic studies of gravitational adjustment over a slope. *Continental Shelf Research*, 24(18): 2133–2148, 2004.
- P. Holland. Turbulent plumes in the southern ocean. University Talk, 2010.
- P. Holland. Oscillating dense plumes. *Journal of Physical Oceanography*, 41(8):1465–1483, 2011.
- P. R. Holland, R. E. Hewitt, and M. M. Scase. Wave breaking in dense plumes. *Journal of Physical Oceanography*, 44(2):790–800, 2014.
- P. Holmes, J. L. Lumley, and G. Berkooz. *Turbulence, coherent structures, dynamical systems and symmetry*. Cambridge university press, 1998.

- V. Ivanov, G. Shapiro, J. Huthnance, D. Aleynik, and P. Golovin. Cascades of dense water around the world ocean. *Progress in oceanography*, 60(1):47–98, 2004.
- S. S. Jacobs. On the nature and significance of the antarctic slope front. *Marine Chemistry*, 35(1-4):9–24, 1991.
- A. Jameson. Solution of the euler equations for two dimensional transonic flow by a multigrid method. *Appl. Math. Comput*, 13(3-4):327–355, 1983.
- A. Jameson. Time dependent calculations using multigrid, with applications to unsteady flows past airfoils and wings. In *10th Computational Fluid Dynamics Conference*, page 1596, 1991.
- L. Jiang and R. W. Garwood Jr. Three-dimensional simulations of overflows on continental slopes. *Journal of Physical Oceanography*, 26(7):1214–1233, 1996.
- J. H. Jungclauss, J. Hauser, and R. H. Käse. Cyclogenesis in the denmark strait overflow plume. *Journal of Physical Oceanography*, 31(11):3214–3229, 2001.
- R. H. Käse, J. Girton, and T. Sanford. Structure and variability of the denmark strait overflow: Model and observations. *Journal of Geophysical Research: Oceans*, 108(C6), 2003.
- P. Killworth. Mixing of the weddell sea continental slope. *Deep Sea Research*, 24(5):427–448, 1977.
- H. Kuo. A new perspective of geostrophic adjustment. *Dynamics of atmospheres and oceans*, 27(1):413–437, 1998.
- A. Lee and D. Ellett. On the contribution of overflow water from the norwegian sea to the hydrographic structure of the north atlantic ocean. In *Deep Sea Research and Oceanographic Abstracts*, volume 12, pages 129–142. Elsevier, 1965.

- S. Legg, R. W. Hallberg, and J. B. Girton. Comparison of entrainment in overflows simulated by z-coordinate, isopycnal and non-hydrostatic models. *Ocean Modelling*, 11(1):69–97, 2006.
- S. Legg, T. Ezer, L. Jackson, B. P. Briegleb, G. Danabasoglu, W. G. Large, W. Wu, Y. Chang, T. M. Ozgokmen, H. Peters, et al. Improving oceanic overflow representation in climate models: the gravity current entrainment climate process team. 2009.
- J. Lighthill. *Waves in fluids*. Cambridge university press, 2001.
- M. S. Lozier. Deconstructing the conveyor belt. *Science*, 328(5985):1507–1511, 2010.
- J. H. Middleton, T. D. Foster, and A. Foldvik. Low-frequency currents and continental shelf waves in the southern weddell sea. *Journal of physical oceanography*, 12(7):618–634, 1982.
- J. H. Middleton, T. D. Foster, and A. Foldvik. Diurnal shelf waves in the southern weddell sea. *Journal of Physical Oceanography*, 17(6):784–791, 1987.
- B. Morton, G. Taylor, and J. Turner. Turbulent gravitational convection from maintained and instantaneous sources. *Proceedings of the Royal Society of London. Series A. Mathematical and Physical Sciences*, 234(1196):1–23, 1956.
- R. Muench, L. Padman, A. Gordon, and A. Orsi. A dense water outflow from the ross sea, antarctica: Mixing and the contribution of tides. *Journal of Marine Systems*, 77(4):369–387, 2009.
- G. I. Ogilvie and D. Lin. Tidal dissipation in rotating giant planets. *The Astrophysical Journal*, 610(1):477, 2004.
- M. Ollitrault, M. Lankhorst, D. Fratantoni, P. Richardson, and W. Zenk. Zonal inter-

- mediate currents in the equatorial atlantic ocean. *Geophysical research letters*, 33(5), 2006.
- T. M. Özgökmen, P. F. Fischer, and W. E. Johns. Product water mass formation by turbulent density currents from a high-order nonhydrostatic spectral element model. *Ocean Modelling*, 12(3):237–267, 2006.
- L. Padman, S. L. Howard, A. H. Orsi, and R. D. Muench. Tides of the northwestern ross sea and their impact on dense outflows of antarctic bottom water. *Deep Sea Research Part II: Topical Studies in Oceanography*, 56(13):818–834, 2009.
- J. Pedlosky. *Geophysical fluid dynamics*. Springer Science & Business Media, 2013.
- O. Phillips. Energy transfer in rotating fluids by reflection of inertial waves. *Physics of Fluids (1958-1988)*, 6(4):513–520, 1963.
- O. Praud, J. Sommeria, and A. M. Fincham. Decaying grid turbulence in a rotating stratified fluid. *Journal of Fluid Mechanics*, 547:389–412, 2006.
- A. Rabitti and L. R. Maas. Meridional trapping and zonal propagation of inertial waves in a rotating fluid shell. *Journal of Fluid Mechanics*, 729:445–470, 2013.
- S. Rahmstorf. Ocean circulation and climate during the past 120,000 years. *Nature*, 419(6903):207–214, 2002.
- D. Randall. *An Introduction to the Global Circulation of the Atmosphere*. Princeton University Press, 2015.
- O. Reynolds. On the dynamical theory of incompressible viscous fluids and the determination of the criterion. *Philosophical Transactions of the Royal Society of London A: Mathematical, Physical and Engineering Sciences*, 186:123–164, 1895. ISSN 0264-

3820. doi: 10.1098/rsta.1895.0004. URL <http://rsta.royalsocietypublishing.org/content/186/123>.
- M. Scase and R. Hewitt. Unsteady turbulent plume models. *Journal of Fluid Mechanics*, 697:455–480, 2012.
- M. Scase, C. Caulfield, S. Dalziel, and J. Hunt. Time-dependent plumes and jets with decreasing source strengths. *Journal of Fluid Mechanics*, 563:443–462, 2006.
- W. J. Schmitz. On the world ocean circulation. volume ii, the pacific and indian oceans/a global update. Technical report, Woods Hole Oceanographic Institution, 1996.
- G. Shapiro and A. Hill. Dynamics of dense water cascades at the shelf edge. *Journal of Physical Oceanography*, 27(11):2381–2394, 1997.
- G. Shapiro and A. Hill. The alternative density structures of cold/saltwater pools on a sloping bottom: The role of friction. *Journal of physical oceanography*, 33(2):390–406, 2003.
- F. P. Shepard, R. Revelle, and R. S. Dietz. Ocean-bottom currents off the california coast. *Science*, 89(2317):488–489, 1939.
- J. E. Simpson. Gravity currents in the laboratory, atmosphere, and ocean. *Annual Review of Fluid Mechanics*, 14(1):213–234, 1982.
- P. Smith. A streamtube model for bottom boundary currents in the ocean. *Journal of Deep Sea Research and Oceanographic Abstracts*, 22(12):853–873, 1975.
- B. R. Sutherland, J. Nault, K. Yewchuk, and G. E. Swaters. Rotating dense currents on a slope. part 1. stability. *Journal of Fluid Mechanics*, 508:241–264, 2004.
- I. Vilibić and N. Šupić. Dense water generation on a shelf: the case of the adriatic sea. *Ocean Dynamics*, 55(5-6):403–415, 2005.

- M. Visser. Neap-spring cycles reflected in holocene subtidal large-scale bedform deposits: a preliminary note. *Geology*, 8(11):543–546, 1980.
- A. Wåhlin. Topographic steering of dense currents with application to submarine canyons. *Deep Sea Research Part I: Oceanographic Research Papers*, 49(2):305–320, 2002.
- A. Wåhlin. Downward channeling of dense water in topographic corrugations. *Deep Sea Research Part I: Oceanographic Research Papers*, 51(4):577–590, 2004.
- A. Wåhlin and C. Cenedese. How entraining density currents influence the stratification in a one-dimensional ocean basin. *Deep Sea Research Part II: Topical Studies in Oceanography*, 53(1):172–193, 2006.
- Q. Wang, S. Danilov, H. Hellmer, and J. Schröter. Overflow dynamics and bottom water formation in the western ross sea: Influence of tides. *Journal of Geophysical Research: Oceans*, 115(C10), 2010.
- M. Wells. Influence of coriolis forces on turbidity currents and sediment deposition. In *Particle-Laden Flow*, pages 331–343. Springer, 2007.
- T. Whitworth and A. Orsi. Antarctic bottom water production and export by tides in the ross sea. *Geophysical research letters*, 33(12), 2006.
- L. Worthington. An attempt to measure the volume transport of norwegian sea overflow water through the denmark strait. *Deep-Sea Res*, 16(Suppl):421–432, 1969.
- C. Wunsch and R. Ferrari. Vertical mixing, energy, and the general circulation of the oceans. *Annu. Rev. Fluid Mech.*, 36:281–314, 2004.
- X. Xu, Y. S. Chang, H. Peters, T. M. Özgökmen, and E. P. Chassignet. Parameterization of gravity current entrainment for ocean circulation models using a high-order 3d nonhydrostatic spectral element model. *Ocean Modelling*, 14(1):19–44, 2006.